Observing the seasonal cycle of pCO_2 from autonomous pH measurements in the South Atlantic sector of the Southern Ocean

Mishka Rawatlal

2020

Dissertation presented for the degree of
Master of Science
in the
Department of Oceanography
University of Cape Town

Supervisors:
Dr K E Altieri (UCT)
Dr P M S Monteiro (SOCCO-CSIR)

Abstract

Global climate predictions hinge on our understanding of the global carbon cycle, and in particular, the role of the Southern Ocean (SO). Sea surface measurements across the SO are sparse and subject to temporal, spatial and seasonal biases. These biases arise from the inaccessibility of the SO due to the high-risk weather conditions and ice coverage experienced during the winter. This study looks at the feasibility of autonomous measuring platforms in the SO for the purpose of reducing the uncertainty bias observed in the SO, constraining the global carbon budget and observing the seasonal cycle of carbonate chemistry in seawater.

The high resolution Wave Glider (WG) dataset located in the sub-Antarctic zone (SAZ) of the SO, during the spring-summer bloom period of 2013/2014, resolves the seasonal cycle of TA from pCO_2 and pH (WGTA) and the empirical expression for TA (Lee et al., 2006) using salinity and temperature and measurements of pH. The discrepancy between WGTA and the calculated TA gives rise to a summer bias in the seasonal cycle of TA attributed to the uptake of nitrate during the bloom period, and the entrainment of nitrate in the pre-bloom period. The effect of this bias on estimating pCO_2 indicates that the amplitude of the pCO_2 seasonal cycle may be overestimated by as much as 3.6% during the pre-bloom period.

An assessment of the Lee et al., (2006) TA expression (LeeTA) in the SO regime against ship-board observations showed a significant regional different in TA between the Atlantic Ocean and Indian Ocean sectors of the SO at the onset of winter, where LeeTA overestimates TA observations in the Atlantic Ocean sector. This further emphasises the seasonal bias of the TA algorithm which provides an averaged TA across the SO as a whole. Hence, it is proposed that a regional formulation be developed for the prediction of TA in each ocean sector of the SO.

To further assess the performance of empirical expressions for TA, the Carter et al., (2014) LIAR expression, utilized by the Southern Ocean Carbon and Climate Observations and Modeling (SOCCOM) project were compared to shipboard underway measurements of TA in the autumn-winter season, and WGTA. The LIAR expression showed a strong dependence on salinity that coincided with the summer bias of the Lee et al., 2006 formulation. This re-enforces that estimates of TA in the SO cannot resolve biologically driven changes in the seasonal cycle of TA, and measurements of pH alone are not enough to elucidate the accurate pCO_2 estimates if TA is not constrained by the seasonal cycle of nitrate.

Declaration

1. I know that plagiarism is a serious form of academic dishonesty.
2. I have read the document about avoiding plagiarism, am familiar with its contents and have avoided all forms of plagiarism mentioned there.
3. Where I have used the words of others, I have indicated this by the use of quotation marks.
4. I have referenced all quotations and properly acknowledged other ideas borrowed from others.
5. I have not and shall not allow others to plagiarise my work.
6. I declare that this is my own work.
7. I am attaching the summary of the Turnitin match overview (when required to do so).

Signature:

Date: 10 February 2020

Supervisors

1. Dr Katye E Altieri
   Department of Oceanography
   University of Cape Town, South Africa

2. Dr Pedro M S Monteiro
   Southern Ocean Carbon-Climate Observatory
   Council for Scientific and Industrial Research, South Africa

Acknowledgements

I would like to extend my gratitude to the following persons, all of whom are in some part responsible for helping me achieve this degree:

To my loving father and mother, to have had your support, guidance and blessings, means more than I could ever convey. It is through your strength, perseverance and will to give me the best that you could manage, that I am able to stand here today. Thank you for carrying me through life, for protecting me and for believing that I could overcome all obstacles in my path. I am because you are, thank you for being my greatest teachers.

To my brother, thank you for showing me what it means to be fearless, to live life outside of the box. You have trekked through life on your own terms and your bravery, passion, intellect and endless coolness never cease to astound me.

Dr Pedro Monteiro, for your supervision, words of wisdom, travel opportunities, understanding and invaluable insights. It has been a privilege to work with you and learn from you. The opportunities you have afforded me have set me on a path far different from any career I could have imagined, and I am eternally grateful for this stepping stone into the wider oceanographic community.

Dr Katye Altieri for your supervision, words of encouragement, the sharing of your life experiences, your understanding, travel opportunities and assistance in all things academic. I look forward to many more discussions over "nerdy" analytical techniques and instrumentation, the atmosphere and everything beyond. Most importantly, I would like to thank you for the inspiring role model you have been over the past few years, and the strides you have made to change the tides of science in South Africa.

Dr Luke Gregor for being a mentor and a friend, your passion for coding has been an inspiration. Natasha van Horsten for being an excellent mentor, your work ethic is unparalleled and it has been an honour to follow your example. Leletu Nohayi and Warren Joubert at the CSIR CO_2 laboratory for your guidance with sample preparation and teaching me the intricacies of the VINDTA system. Mtushushu at the DEA for your dedicated analysis of samples in my hour of need. Raymond Roman and Raquel Flynn for assisting me with nutrient analysis.

The DEA for allowing me the opportunity to board the R/V *SA Agulhas II*, and the captain and crew thereof. The NRF, DST and SANAP for their support in my endeavour to complete this

dissertation. The CSIR for awarding me their Earth Observations Bursary which allowed me to pursue my MSc at UCT. SOLAS, SCOR, and GEOMAR for their financial support with travel and the invitation to participate at the International SOLAS Summer School.

A big thank you to my friends, Riesna Audh, Timothy Gwynn, Ruan Parrott, Shantelle Smith, Kurt Spence, Robyn Granger, Asmita Singh and Suvarna Sokay, without your support, encouragement and laughter, Cape Town would be a truly dull place to live and work. To Theoshan Moodley, Ushik Mewlal, Shoval Maharaj and the GS Family, you have travelled a long road with me, forever keeping me grounded and supporting me, thank you for never leaving a man behind.

A special thank you to Cashifa Karriem, the most steadfast captain in all that we do.

I dedicate this work to the loving memory of my father, who could not wait to read it.

Today seems bad, but the sun will rise again tomorrow.

I wish you were here to watch it shine with me.

Mr Ishwarlal Rawatlal

(1948 – 2019)

"…to preserve and cherish the pale blue dot, the only home we've ever known."

– Carl Sagan

Pale Blue Dot: A Vision of the Human Future in Space

Table of contents

List of abbreviations and acronyms

ACC	Antarctic circumpolar current
APF	Antarctic polar front
ASZ	Antarctic-Southern Zone (Gray et al., 2018)
CSIR	Council for Scientific and Industrial Research
DEA	Department of Environmental Affairs
DPT	Drake passage time-series
DIC	Total dissolved inorganic carbon
ESRL	Earth System Research Laboratory
GEOSECS	Geochemical Ocean Section Study
HNLC	High-nutrient, low-chlorophyll
IPCC	Intergovernmental Panel on Climate Change
ISFET	Ion-selective field effect transistor
ISE	Ion-selective electrode
JGOFS	Joint Global Ocean Flux Study
LEEpCO_2	pCO_2 derived from pH and calculated total alkalinity (Lee et al., 2006)
LeeTA	Total alkalinity derived from Lee et al., (2006) relationship for total alkalinity
LIAR	Locally interpolated alkalinity regression
MAPCO_2	Moored autonomous pCO_2
MBARI	Monterey Bay Aquarium Research Institute
MOSFET	Metal oxide semiconductor field effect transistor
MIZ	Marginal ice zone
MLR	Multiple linear regression
NBS	National Bureau of Standards

pCO_2	Partial pressure of carbon dioxide in seawater
PFZ	Polar frontal zone
pH_T	pH measured on the total scale
PUZ	Polar upwelling zone
SACCF	Southern Antarctic circumpolar current front
SAF	Sub-Antarctic front
SAMW	Sub-Antarctic Mode Water
SAWS	South African Weather Service
SAZ	Sub-Antarctic zone
SBdy	Southern boundary
SSIZ	Seasonal sea-ice zone
SOCAT	Surface Ocean CO_2 Atlas
SOCCO	Southern Ocean Carbon and Climate Observatory
SOCCOM	Southern Ocean Carbon and Climate Observations and Modeling
SSS	Sea surface salinity
SST	Sea surface temperature
STF	Sub-tropical front
STZ	Sub-tropical zone
TA	Total alkalinity
UCDW	Upper circumpolar deep water
UCT	University of Cape Town
VINDTA	Versatile instrument for the determination of total inorganic carbon and titration alkalinity
WC	Winter Cruise
WG	Wave Glider

WOCE World Ocean Circulation Experiment

List of figures

List of tables

1 Introduction and Literature Review

Since the rise of the industrial revolution in the 18th century, the combustion of fossil fuels, increased land-change practices and industrial processing have rapidly released carbon dioxide (CO_2) into the atmosphere leading to an increase of CO_2 from ~275 ppm in 1750 to ~408 ppm in 2018 (Le Quéré et al., 2018, Tans and Keeling, 2018, Etheridge et al., 1996). The recent record of the accelerating rate of this release is reflected in the atmospheric CO_2 observations taken at the Mauna Loa Observatory (Figure 1.1). This anthropogenic perturbation of CO_2 into the atmosphere results in global warming through the greenhouse effect, and consequently impacts on climate change.

The CO_2 molecule, like other greenhouse gases, readily absorbs longwave terrestrial radiation emitted by the Earth. These greenhouse gas molecules then re-emit the radiation back to Earth, effectively trapping heat in the atmosphere, and thus raising global temperature (Wallace and Hobbs, 2006). It follows that as concentrations of CO_2 increase, so does global temperature. Thus, the long term trend of anthropogenic CO_2 in the atmosphere is of particular interest for the future of quality life on Earth.

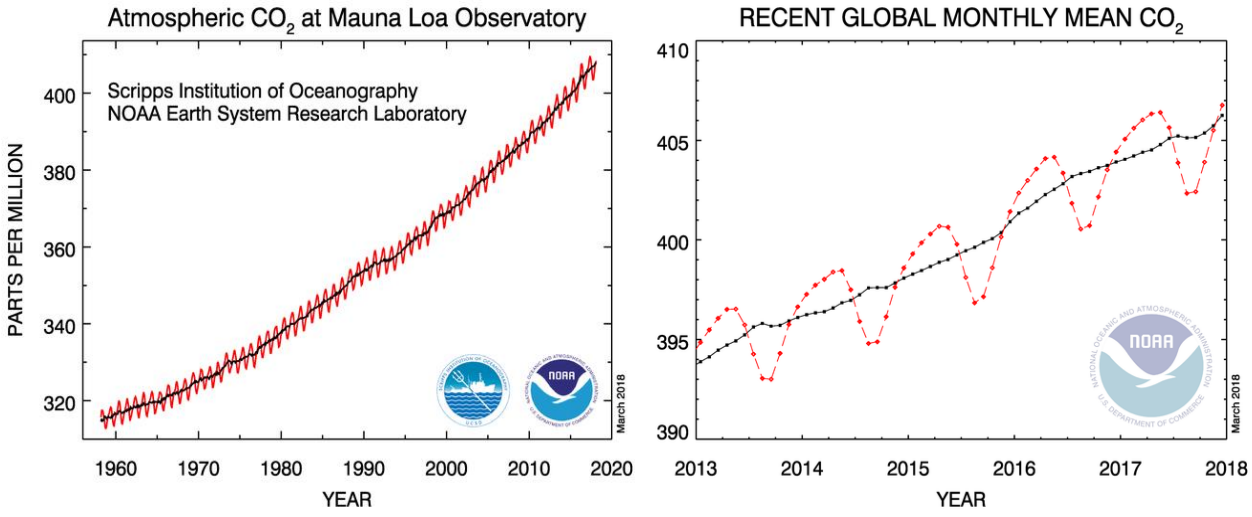

Figure 1.1: The Keeling curve depicts the rising CO_2 concentration in the atmosphere, largely attributed to the burning of fossil fuels for energy production. The red curve signifies direct measurements of CO_2 as the mole fraction in dry air. The black curve indicates the monthly mean values of CO_2, corrected for the average seasonal cycle. Atmospheric CO_2 has risen from ~270 ppm in 1750 to ~408 ppm at present day (Tans and Keeling, 2018)

The transfer of carbon between the atmosphere, land and ocean carbon reservoirs is described by the global carbon cycle (Emerson and Hedges, 2008). Increasing urbanization and land use has reduced the uptake of anthropogenic CO_2 from the atmosphere by the land biosphere, however, current estimates show that the land sink (3.0 ± 0.8 Gt C/yr) and oceanic sink (2.4 ± 0.5 Gt C/yr) for CO_2 from the atmosphere are comparable (Figure 1.2, Le Quéré et al., 2018). The flux of CO_2 between the land and atmosphere is highly variable and difficult to observe with certainty. Thus, the accurate measurement of ocean-atmosphere CO_2 fluxes are important to constrain the global carbon budget.

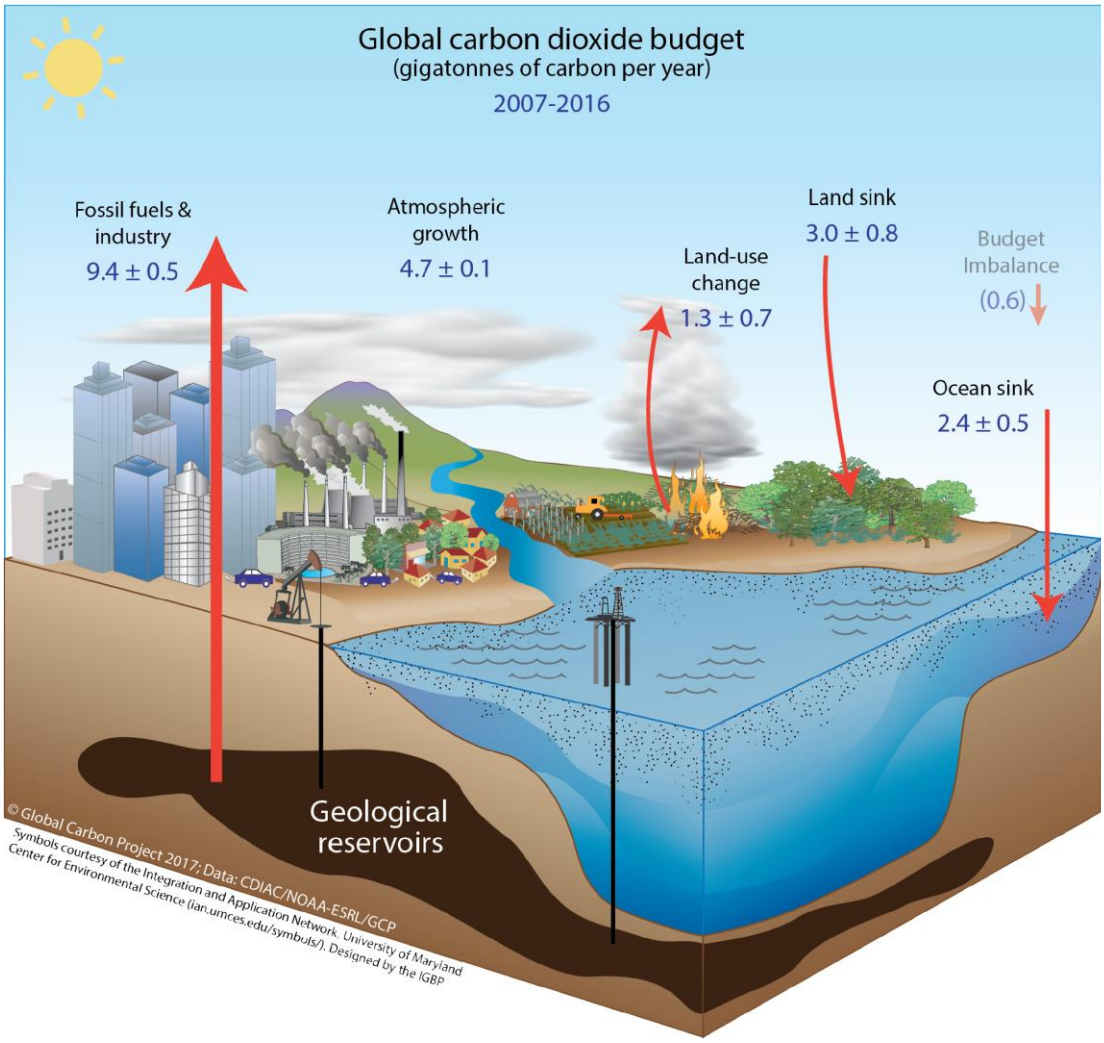

Figure 1.2: The current estimate of the flux of anthropogenic carbon across the terrestrial biosphere, the hydrosphere and the atmosphere as outlined by the Global Carbon Budget 2017 (Le Quéré et al., 2018)

Our understanding of carbon storage in the ocean through marine carbonate chemistry is dependent on the physical and chemical processes taking place at the air-sea interface (Section 1.4). Approximately 40 % of anthropogenic CO_2 emissions to the atmosphere are taken up by the ocean (Sabine et al., 2004), and of this it is estimated that the Southern Ocean alone takes up ~ 43 % (Landschützer et al., 2015, Khatiwala et al., 2013).

The ocean naturally absorbs CO_2 by means of the thermodynamic equilibrium that exists at the ocean-atmosphere interface. However, the absorption of CO_2 throughout the ocean basins is not uniform. The physical drawdown of CO_2 from the atmosphere is stronger at higher latitudes in regions of deep water formation, and weaker at mid latitudes in regions where deep water is upwelled to the surface. Coupled with this is the effect of temperature on CO_2 absorption, known as the solubility pump, whereby colder sea surface waters at the poles are able to absorb greater amounts of CO_2 from the atmosphere than warmer waters at the equator. As CO_2 enters the ocean, it is available for uptake by biology. The biological pump transports CO_2 from the surface ocean into the ocean interior by transforming it into dissolved organic carbon and particulate organic carbon (Sabine and Feely, 2007).

The pH of seawater is largely controlled by the speciation of carbonate in seawater, and changes in the equilibrium of this system act as a chemical buffer between the oceanic and atmospheric reservoirs of carbon (Sarmiento and Gruber, 2013). The growing influx of anthropogenic CO_2 into the ocean impacts the carbonate chemistry in seawater (explained in Section 1.4) by lowering the pH, which has led to ocean acidification. However, the focus of this study will concentrate on the high precision measurement of pH to quantify the carbonate system in seawater.

1.1 The Southern Ocean

The Southern Ocean (SO), defined as the unbounded ocean region south of 40 °S, encircles the continent of Antarctica and covers approximately 30 % of the global ocean surface. The SO accounts for almost half of the total uptake of anthropogenic CO_2 (~43 %) and three-quarters of the heat (~75 %) from the atmosphere (Frölicher et al., 2015, Sabine et al., 2004, Khatiwala et al., 2013). It is estimated to absorb ~25 % of anthropogenic CO_2 emissions on an annual basis (Le Quéré et al., 2016) and as such, plays a critical role in climate change.

The SO connects three large ocean basins (Indian, Atlantic and Pacific) via the Antarctic Circumpolar Current (ACC) that is driven eastward by the strong westerly winds (Rintoul et al., 2001), and northward by Ekman transport, which forms part of the meridional overturning circulation. The ACC is characterised by the continuous flow of several fronts of varying strength: the Sub-Tropical Front (STF) at the north-most boundary, the Sub-Antarctic Front (SAF), the Antarctic Polar Front (APF), the Southern ACC Front (SACCF) and the Southern Boundary (Sbdy) (Figure 1.3). The zonally unbounded flow across the three ocean basins allow for the transport of heat, nutrients, water and associated properties from one region to another (Rintoul et al., 2001).

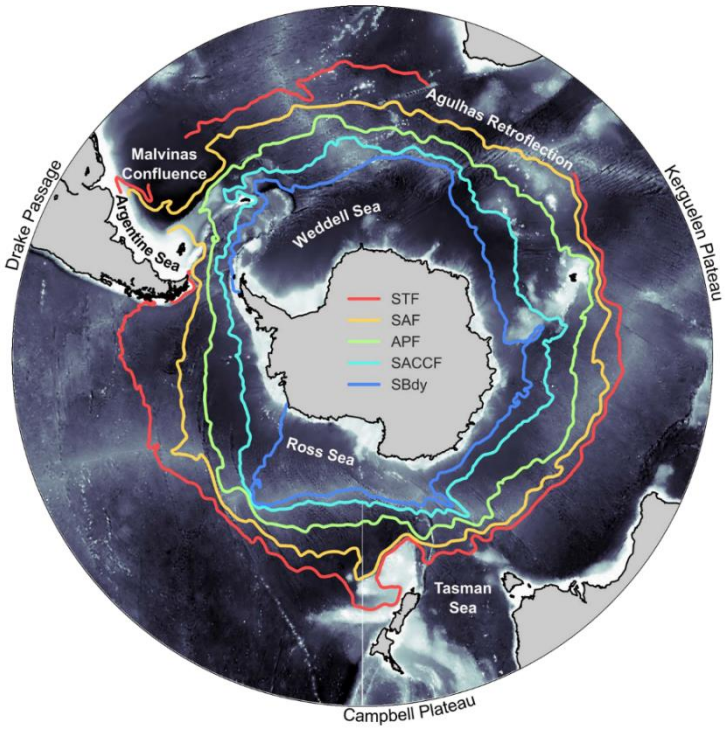

Figure 1.3: Major fronts of the Antarctic Circumpolar Current (ACC) in the Southern Ocean: Subtropical Front (STF), Sub-Antarctic Front (SAF), Antarctic Polar Front (APF), Southern ACC Front (SACCF) and the Southern boundary (Sbdy). Image sourced from PhD thesis of Gregor (2017)

Global climate predictions hinge on our understanding of the role of the SO in the global carbon cycle. The physical mechanism by which anthropogenic CO_2 enters the ocean is the formation and transport of shelf, surface, intermediate and deep waters (Figure 1.4). Antarctic Bottom Water (AABW) is formed against the continent shelf, as strong winds create polynyas (open ocean areas surrounded by ice) which pump the high salinity, dense, cold waters downward to the ocean bottom (< 0 °C, salinity maxima ~34.8 PSU), and transports the water mass northward. This is the site at which a large amount of atmospheric CO_2 is drawn down into the deep ocean, facilitated via rapid air-sea gas exchange by the strong winds driving the polynyas (Talley, 2011, Rintoul et al., 2001).

Circumpolar deep water (CDW) is formed from the deep-water masses of each of the surrounding ocean basins as they move south into the ACC, upwelling into the region south of the Polar Front (PF). This mixes with Antarctic water masses that are not dense enough to be AABW. CDW is a combination of Upper CDW (UCDW) characterised by an oxygen minimum layer and high nutrient concentration (1.5 – 2.5 °C, 33 – 34.5 PSU) , and Lower CDW (LCDW) characterised by a salinity maximum layer (1.3 – 1.8 °C, 34.8 – 34.9 PSU). UCDW lies just beneath the surface waters of SACCF as it upwells, supplying nutrients to the surface layer, and is transported northward via Ekman transport. It is this connection of deep water to the surface layer that allows the outgassing of CO_2-saturated waters to the atmosphere. LCDW also upwells in this region moving southward toward the continent, laying beneath the UCDW and eventually being sub-ducted and transported north, forming the dense, high salinity, bottom waters of the world's oceans north of the ACC (Talley, 2011).

Antarctic Intermediate Water (AAIW) lies north of the SAF, and is pervasive through the sub tropics and sub-tropical gyres of the Southern Hemisphere, characterised by a low salinity layer (~ 34.2 PSU) at ~ 500 – 1500 m at a temperature range of 4 – 5 °C. AAIW is thought to form from the sinking of the Antarctic surface waters as they are transported north via Ekman transport across the SAF (Talley, 2011).

Sub-Antarctic surface water (SASW) in the upper 500 m of the surface ocean is found north of the SAF and is characterised by high salinity waters (> 34 PSU, -1 – 4 °C) due to the proximity of the sub-tropical gyres. The deep winter mixed layers adjacent to the SAF are known as Sub-Antarctic Mode Water (SAMW). SAMW (8 – 9 °C, ~34.6 PSU) is transported eastward with the flow of the ACC, or northward by Ekman transport and sub-ducted to from part of the subtropical gyres. At the surface, SAMW take up large amounts of anthropogenic CO_2 from

the atmosphere due to increased wind speeds which act to enhance the gas-transfer velocity and waters that are under-saturated in pCO_2 (Talley, 2011).

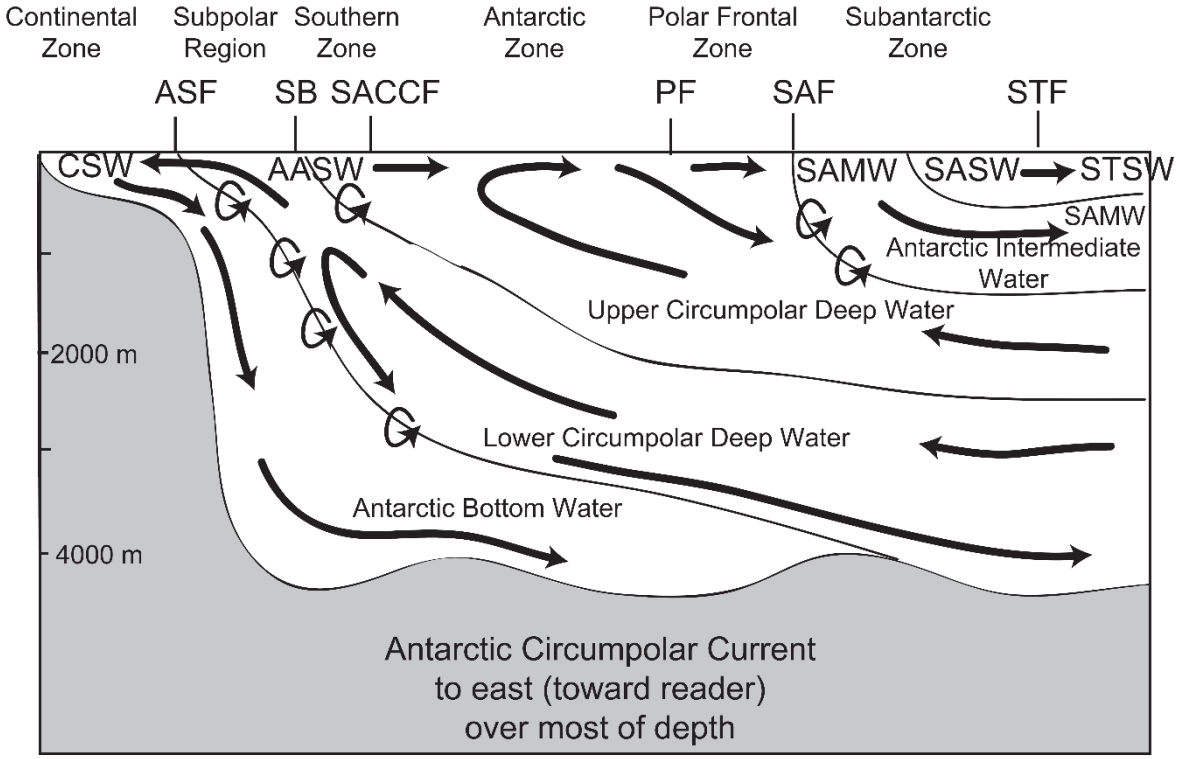

Figure 1.4: Schematic of the meridional overturning circulation in the Southern Ocean showing the movement of water masses across the major fronts and zones. Water masses: Continental Shelf Water (CSW), Antarctic Surface Water (AASW), Antarctic Bottom Water (AABW), Lower Circumpolar Deep Water (LCDW), Upper Circumpolar Deep Water (UCDW), Antarctic Intermediate Water (AAIW), Sub-Antarctic Mode Water (SAMW) and Sub-Antarctic Surface Water (SASW). Fronts: Antarctic Slope Front (ASF), Southern Boundary (SB), Southern ACC Front (SACCF), Polar Front (PF), Sub-Antarctic Front (SAF), Subtropical Front (STF). Image sourced from Talley (2011) based on Speer et al. (2000).

Owing to the paucity of data in this region, the SO is responsible for much of the uncertainty in current earth system model predictions. The flux of CO_2 and trace gases across the air-sea interface are dependent on sea surface temperature, salinity, mixed layer physical processes, wind speed and biological productivity. The largest compilation of high resolution seawater pCO_2 measurements are found in the Surface Ocean CO_2 Atlas (SOCATv4) database (Bakker et al., 2016) containing over 18 million observations spanning from 1957 – 2015. Currently,

the Drake Passage Time-series (DPT) situated across the ACC, between the southern tip of South America and Antarctica, is the most temporally and spatially sampled region of the SO with 20 crossings per year since 2002 (Munro et al., 2015).

However, sea surface measurements across the SO at large are sparse and subject to temporal, spatial and seasonal bias as the routes travelled are largely repetitive in order to resupply Antarctic bases during the summer (Gregor et al., 2018). This emphasises the need for the deployment of autonomous measuring systems throughout the Southern Ocean in the form of ocean robotics, moorings and profiling floats - such as those utilised by the Southern Ocean Seasonal Cycle Experiment II (SOSCEx II) (Monteiro et al., 2015) and the Southern Ocean Carbon and Climate Observations and Modelling (SOCCOM) project (Russel et al., 2014). SOSCEx makes use of remote operational systems, namely the Wave Glider and the Sea Glider which are fitted with various autonomous sensors for physical, biological and chemical seawater parameters. The SOCCOM project uses biological Argo profiling floats that have been modified to operate beneath the sea ice.

1.2 Non-steady state of the natural and anthropogenic CO_2 signal

The transport cycle of CO_2 between the land, ocean and atmosphere was thought to be in steady state prior to the industrial revolution, since the atmospheric concentrations of CO_2 remained at a constant of ~280 ppm (Etheridge et al., 1996). However, through the perturbation of CO_2 into the atmospheric reservoir through the burning of fossil fuels, industrial cement production and deforestation, the steady state equilibrium of carbon transport between the respective reservoirs has been disturbed. The extent of the anthropogenic perturbation is still unclear.

It was postulated that the anthropogenic perturbation of CO_2 in the atmospheric carbon reservoir would act passively over the natural steady-state signal driven by biology and circulation (Matear et al., 2000). However, recent model evaluations and observations suggest the emergence of a non-steady state CO_2 signal owing to a large outgassing of CO_2 from the ocean due to climate change and rising surface ocean temperatures (Le Quéré et al., 2007). This led to the identification of an emerging non-steady state oceanic CO_2 signal. McNeil (2013) proposed a novel multi-method approach to distinguish between the natural CO_2 signal, the anthropogenic CO_2 signal and now, the non-steady state oceanic CO_2 signal (McNeil, 2013).

The multi-method approach employs several techniques that capture the steady-state signal and the net oceanic signal. The non-steady state oceanic signal can then be inferred by the combination of these signals, however, the uncertainty associated with this approach renders the currently observable signal statistically insignificant (McNeil, 2013). In order to accurately deconstruct the CO_2 signal into its respective steady state and non-steady components and reduce uncertainty, accurate measurements of pCO_2 in the surface ocean are required.

The determination of the non-steady state oceanic signal can give us valuable insight into the evolution of the oceanic CO_2 sink and more importantly, constrain the global carbon budget. According to Le Quéré et al. (2007), a large percentage of the non-steady state signal can be attributed to the outgassing of CO_2 from the carbon rich waters of the Southern Ocean, in correlation with the intensification of winds across decadal timescales. Seasonal studies in different sectors of the Southern Ocean have reportedly shown a shift from ocean sink to source of CO_2, from summer to winter respectively (Metzl et al., 2006, Fransson et al., 2004).

Due to limited sampling it is difficult to determine whether or not the Southern Ocean CO_2 sink will strengthen in response to the anthropogenic perturbation of CO_2 to the atmosphere and the

decadal outgassing witnessed from model and observational data. Recent studies (Munro et al., 2015, Williams et al., 2017, Landschützer et al., 2015, Majkut et al., 2014, Gray et al., 2018) have reported a strengthening of the Southern Ocean pCO_2 sink. However, owing to the lack of observational data for the winter season, model predictions are still inconsistent with these findings.

1.3 The SOCCOM Project

The Southern Ocean Carbon and Climate Observations and Modelling (SOCCOM) project is a regional division of the biogeochemical-Argo Program (Group, 2016) that aims to deploy ~200 autonomous floats throughout the Southern Ocean. To date, there are ~100 floats in operation around the Antarctic continent, with more than 3.5 million biogeochemical measurements throughout the water column in remote regions.

The aim of the SOCCOM project is to understand the mechanisms at play in the Southern Ocean that impact on the climate and global ocean biogeochemistry by increasing the number of monthly biogeochemical measurements made in this region. The increased measurements of biogeochemical parameters will improve our understanding of carbon uptake, biological activity and the nutrient distribution of the Southern Ocean to the global ocean. This will further improve constraints on high resolution Earth system models, reduce spatiotemporal bias, and improve projections for Earth's climate and biogeochemistry. The floats can also help to resolve inter-annual and annual variability in biogeochemical parameters in the Southern Ocean that cannot be accomplished through ship-board measurements or satellite observations.

The biological-Argo profiling floats are fitted with biogeochemical sensors to measure pH, nitrate, oxygen, chlorophyll-a fluorescence, suspended particle abundance and down-welling irradiance (Group, 2016). The floats obtain a horizontal and vertical profile of the ocean interior as they sample the ocean down to a depth of 2000 m once every five to ten days. The floats have a lifespan of 250 – 300 vertical profiles (depending on their sampling cycle) which equates to roughly 7 years. This long lifespan allows us to resolve seasonal to inter-annual variations in carbon and nutrient cycling through the water column.

Recent studies utilised the measured pH captured by these floats together with an estimated TA to calculate pCO_2 all year round, thereby deducing seasonal variations in the Southern Ocean (Williams et al., 2017, Gray et al., 2018). The source and sink of pCO_2 varies regionally and zonally in the SO, depending on the dominant mechanism of uptake or saturation in each zone.

All data collected by the SOCCOM floats are made freely available in near real-time via the SOCCOM website. Float data can be obtained interactively through a mapped tool for each float, or through a database in varying resolution through the website under the float identifier.

1.4 The carbonate system in seawater

The carbonate chemistry of seawater plays a large role in the ocean's capacity to uptake carbon dioxide from the atmosphere. Thermodynamic equilibrium equations describe the reaction of CO_2 with seawater, which provide a buffering effect to the flux of anthropogenic CO_2 into the ocean. The drawdown of atmospheric CO_2 into the ocean is facilitated through several physical, chemical and biological processes (Figure 1.5) (Sabine et al., 2004). These processes can be described as a system of pumps that compete with each other and include vertical transport and mixing, air-sea gas exchange, formation of calcium carbonate, photosynthesis and remineralization (Sarmiento and Gruber, 2013). However, CO_2 is not the dominant species present in the ocean, it exists as dissolved inorganic carbon (DIC), dissolved organic carbon (DOC), particulate organic carbon (POC), calcium carbonate ($CaCO_3$) and in trace amounts as aqueous CO_2 and carbonic acid.

The solubility pump is comprised of the temperature-driven solubility of CO_2 in seawater, and the transport of CO_2 into the deep ocean via thermohaline circulation (Sabine et al., 2004). The surface ocean loses heat to the atmosphere in the high latitudes, where deep water formation takes place, taking up more CO_2 from the atmosphere as CO_2 dissolves readily in cold waters to produce inorganic carbon species (DIC). Conversely in the low latitude region, cold waters are upwelled to the surface and warmed at the equator, leading to an outgassing of CO_2 from the surface ocean (Sarmiento and Gruber, 2013). The biological pump counters the effects of this outgassing of CO_2 to the atmosphere, and is comprised of the soft-tissue and carbonate pumps.

The soft-tissue pump depletes the surface ocean of inorganic CO_2 and nutrients through the photosynthetic production of organic matter (DOC and POC). Biological productivity is dependent on light availability and nutrients in the surface ocean. Productivity in warmer lower latitude regions are efficient at utilising the high concentration of inorganic CO_2 and nutrients upwelled from the deep ocean. Thus, limiting the amount of CO_2 available to outgas into the atmosphere. However, in high latitude regions such as the Southern Ocean, biological production is less efficient due to limited iron and light availability, thus there is an excess of CO_2 and nutrients in these surface waters (Sarmiento and Gruber, 2013, Emerson and Hedges, 2008).

The organic matter produced by photosynthesis sinks through the water column as it increases in mass or is drawn down by vertical mixing. As organic matter sinks, it decomposes back into

inorganic carbon through the process of remineralisation, thus storing atmospheric CO_2 in the ocean interior (Emerson and Hedges, 2008, Sarmiento and Gruber, 2013).

The carbonate pump describes the action of calcifying organisms that form calcium carbonate shells in the surface ocean and rapidly sink through the water column. While the precipitation of $CaCO_3$ utilises DIC species present in seawater, it also produces CO_2 as a by-product, thus acting in contrast to the soft-tissue pump, which decreases CO_2 in the surface ocean. $CaCO_3$ shells sink through the water column, leading to dissolution in the deep ocean or becoming incorporated in sediment at the bottom of the ocean (Sarmiento and Gruber, 2013).

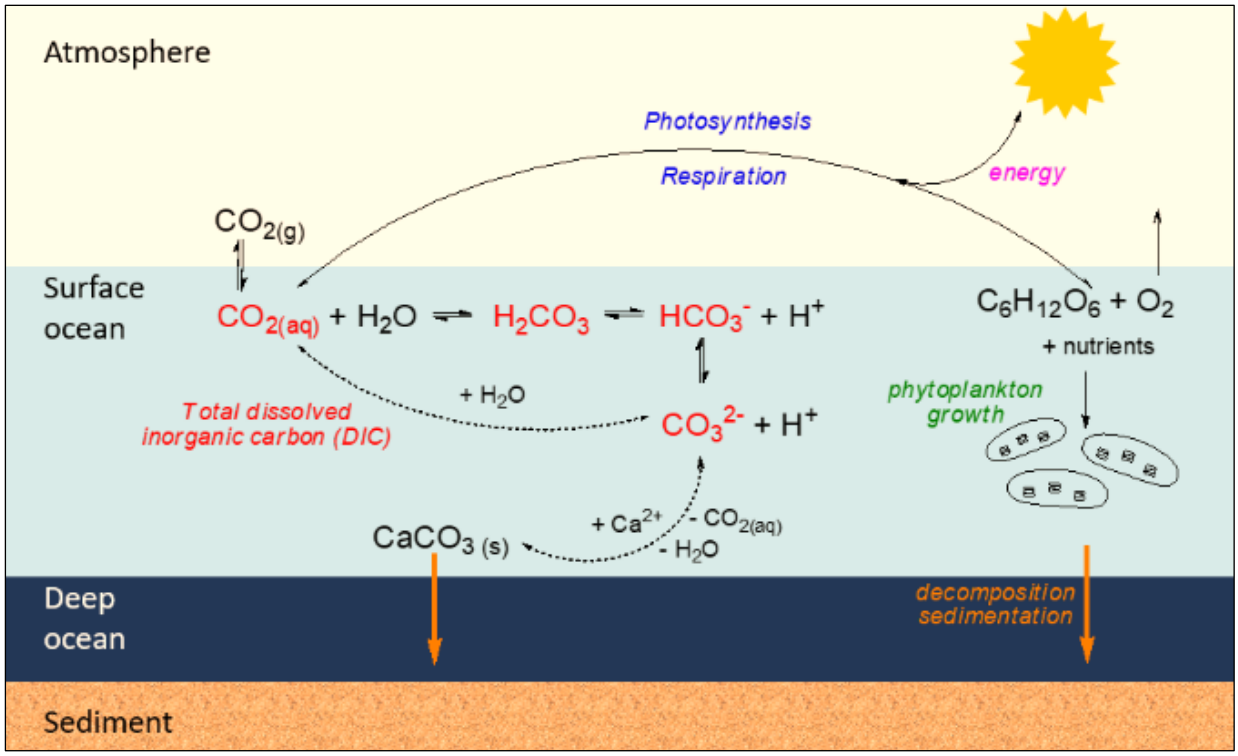

Figure 1.5: Scheme depicting the solubility, biological, soft-tissue and carbonate pumps at play in the surface ocean, which influence CO_2 drawdown from the atmosphere into the ocean.

To quantitatively determine the carbonate system of seawater, it is necessary to define the thermodynamic equilibrium equations which describe the reaction of CO_2 with seawater, and the four master variables which impact this system: the DIC concentration, the total alkalinity (TA), the pH of the seawater and finally the partial pressure of carbon dioxide (pCO_2) in seawater (Emerson and Hedges, 2008). By accurately measuring at least two of these variables, we can use the thermodynamic equilibrium equations to calculate the remaining two master

variables, and the relative concentrations of the carbonate species present in seawater (Dickson and Goyet, 1994).

The dissolution of gaseous CO_2 into water is described by the following thermodynamic equilibrium equation, where K_0 is the solubility constant for carbon dioxide in seawater. K_0 is highly dependent on the temperature of the surface ocean, which drives the air-sea gas exchange. Colder waters will absorb more CO_2 compared to warmer waters (Sarmiento and Gruber, 2013, Zeebe and Wolf-Gladrow, 2001).

$$CO_{2_{(g)}} \overset{K_0}{\Leftrightarrow} CO_{2_{(aq)}} \tag{1}$$

$$K_0 = \frac{[CO_{2_{(aq)}}]}{[CO_{2_{(g)}}]} \tag{2}$$

K_0 is defined as the solubility coefficient of CO_2 in water based on Henry's Law (Zeebe and Wolf-Gladrow, 2001):

$$pK_0 = -\log K_0 \tag{3}$$

Aqueous CO_2 reacts with water to form carbonic acid

$$CO_{2_{(aq)}} + H_2O \rightleftharpoons H_2CO_3 \tag{4}$$

The concentrations of aqueous CO_2 and H_2CO_3 are present in such small quantities, that they are often denoted together as CO_2^* (Zeebe and Wolf-Gladrow, 2001):

$$CO_2^* = \left[CO_{2_{(aq)}}\right] + [H_2CO_3] \tag{5}$$

H_2CO_3 rapidly dissociates into the carbonate ion by the loss of a proton. The bicarbonate ion further dissociates to the carbonate ion by losing the remaining proton:

$$CO_2 + H_2O \overset{K_1}{\Leftrightarrow} HCO_3^- + H^+ \quad (6)$$

$$HCO_3^- \overset{K_2}{\Leftrightarrow} CO_3^{2-} + H^+ \quad (7)$$

where

$$K_1 = \frac{[HCO_3^-][H^+]}{[CO_2]} \quad (8)$$

$$K_2 = \frac{[CO_3^{2-}][H^+]}{[HCO_3^-]} \quad (9)$$

K_1 and K_2 are the stoichiometric equilibrium constants for the respective dissociation reactions, and control the forward and reverse reactions. The equilibrium constants are dependent on temperature, salinity and pressure, and are determined experimentally. Several expressions for K_1 and K_2 have been reported e.g. (Lueker et al., 2000, Millero et al., 2006, Mehrbach et al., 1973), as well as numerous comparisons between these expressions e.g. (Lee et al., 1996, Millero et al., 2002, Clayton et al., 1995), however, these studies cannot agree on which is the most accurate set of expressions.

Total dissolved inorganic carbon

The total dissolved inorganic carbon (DIC) is the sum of the individual inorganic carbonate species in seawater: CO_2, HCO_3^- and CO_3^{2-}.

$$DIC = [CO_2] + [HCO_3^-] + [CO_3^{2-}] \quad (10)$$

Figure 1.6 shows the Bjerrum plot depicting the relative speciation of DIC present in seawater at a given pH. At an estimated surface ocean pH of ~ 8.1 indicated on the figure, the concentration of HCO_3^- is dominant, followed by CO_3^{2-}, and the smallest concentration present is CO_2*. It is the proportions of these carbonate ions in seawater which control the seawater pH.

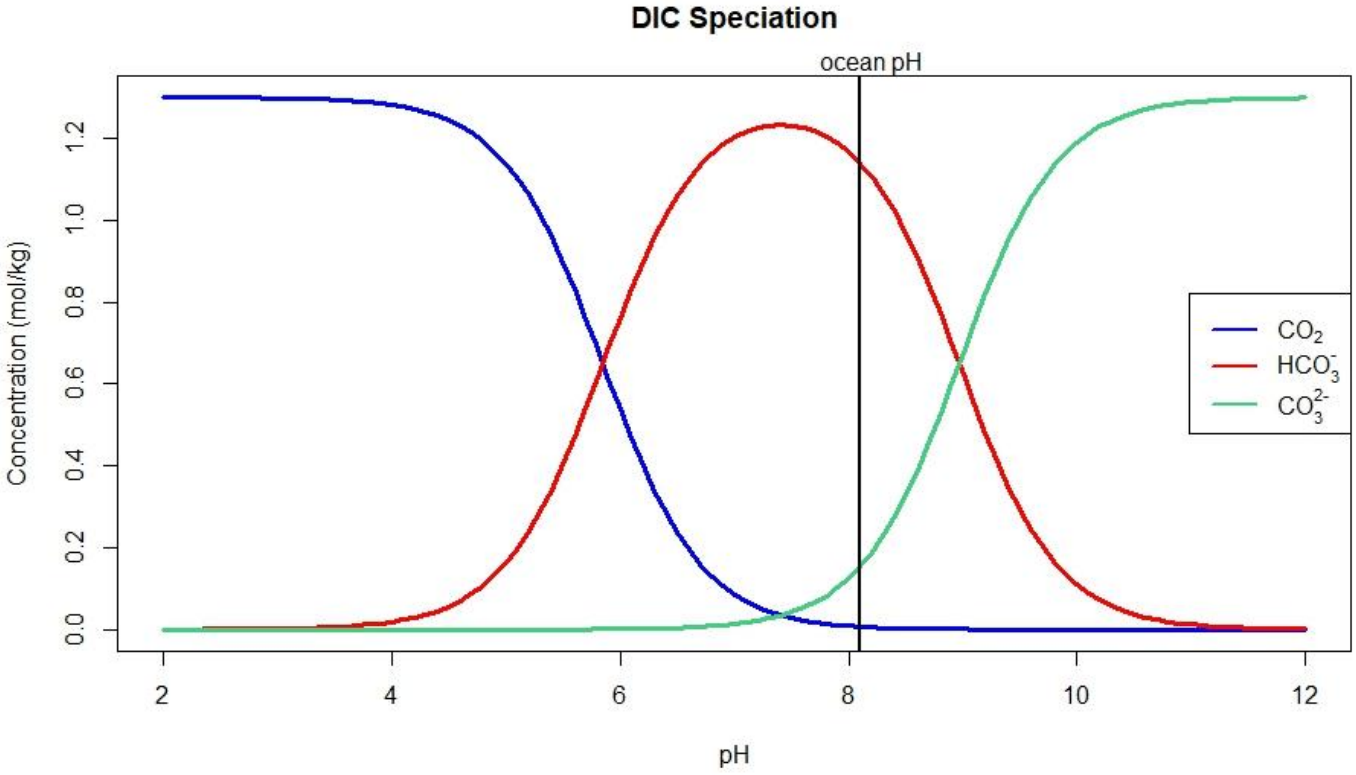

Figure 1.6: Bjerrum plot indicating the dominant carbonate ion species present in seawater and the corresponding pH

Changes in the concentration of DIC in seawater (Zeebe and Wolf-Gladrow, 2001):

The main drivers affecting changes in DIC concentrations in seawater are summarised as follows:

1. Photosynthesis and respiration

   DIC decreases with photosynthesis as CO_2 is utilised to produce glucose and oxygen, the reaction scheme is seen in Figure 1.5. Conversely, CO_2 is released through respiration and increases the concentration of DIC in seawater.

2. Formation and dissolution of calcium carbonate

   DIC concentration is decreased as carbonate ions are utilised in the biogenic precipitation of $CaCO_3$ shells. However, this reaction also produces CO_2 as a by-product, increasing the DIC pool. The dissolution of $CaCO_3$ releases carbonate ions, increasing the concentration of DIC.

3. Remineralization

   Dissolved organic carbon species are converted back to DIC and release nutrients as they progress down through the water column, thereby increasing the concentration of DIC.

4. Air-sea gas exchange

   Dependent on the temperature, salinity and wind speed over the surface ocean, CO_2 is absorbed in cold high latitude waters, in regions of deep water formation, increasing the DIC concentration. In the low-latitude warm waters, in regions of upwelling, DIC is decreased as CO_2 is outgassed to the atmosphere, and absorption of CO_2 into the ocean is weak.

5. Upwelling

   Upwelled waters enriched with DIC (via remineralization) are brought up to the surface, thereby increasing the concentration of DIC in surface waters.

The pH of seawater

pH is a measure of the hydrogen ion concentration in a solution, it is defined by the equation:

$$pH = -\log [H^+] \quad (11)$$

The most accurate representation of pH is in terms of activity, however, activities cannot be determined experimentally in a solution of high ionic strength containing multiple species. When the concentration of a solute is greater than 0.1 M, interactions between the solute molecules or ions are significant, and the effective and real concentrations are no longer equal (Housecroft and Sharpe, 2005). The deviations from ideality associated with seawater do not allow for the use of the stoichiometric thermodynamic relationships, thus pH must be operationally defined on an appropriate scale that is consistent with the experimentally defined equilibrium constants (Zeebe and Wolf-Gladrow, 2001).

It is required that these concentrations are expressed in terms of activity, which takes into account the interactions between the ionic species in solution. The activity of a species (a) is related to the stoichiometric concentration of the species by the activity coefficient (γ) (Zeebe and Wolf-Gladrow, 2001):

$$a_H = \gamma_H [H^+] \quad (12)$$

Under ideal behaviour, the activity coefficient of a chemical species is unity (1.0) under the infinite dilution convention that applies to simple systems of high activity, which implies a dependence on the concentration of the chemical species. The calculation of the activity coefficient for low ionic strength systems can be approximated by the Davies equation or the Debye-Huckel limiting law for ionic solutions, and will not be considered here (Loewenthal and van Rooyen Marais, 1976).

For seawater, the increased number of ions indicates a low ionic activity due to the interaction of the ions with each other i.e. long range electrostatic interactions, ion pairing and the formation of ionic complexes. The ionic strength of a solution is a measure of the concentration of ionic species present in an aqueous solution, defined as (Loewenthal and van Rooyen Marais, 1976):

$$I = \frac{1}{2} \sum c_i \, z_i{}^2 \qquad (13)$$

where c is the concentration of chemical species *i*, z is the charge of the ion *i*. The complex system of seawater contains a mixture of different charged ions. The ionic strength of seawater is ~ 0.7 (Loewenthal and van Rooyen Marais, 1976, Zeebe and Wolf-Gladrow, 2001), which is considered a high ionic strength, high salinity solution. In such cases, the activity coefficient will be expressed as a total activity quantity that accounts for all deviation, and is estimated by the use of ion-pairing models (Zeebe and Wolf-Gladrow, 2001).

It stands to reason then that the correct representation for the thermodynamic equilibrium constants defined for the carbonate equilibria described at the start of this chapter, are more appropriately expressed in terms of activities:

e.g. $$K_2 = \frac{\{H^+\}\{CO_3{}^{2-}\}}{\{HCO_3{}^-\}}$$

However, the measurement of these quantities in seawater is extremely difficult, and are thus expressed in terms of stoichiometric concentrations. This is made possible by the assumptions based on the constant ionic medium convention – whereby the ratio of the composing ions are fairly constant, which is the case for the seawater matrix. The deviations from ideality caused through ion pairing and complex formation are quantified by the changes in the equilibrium constants due to ionic strength and chemical composition (Loewenthal and van Rooyen Marais, 1976).

The activity coefficients of each ion decrease as the ionic strength increases (i.e. activity decreases), this in turn changes the ratio of the activity coefficients used to express the equilibrium constant:

e.g. $$K_2{}^* = K_2 \frac{\gamma_{HCO_3{}^-}}{\gamma_{H^+}\gamma_{CO_3{}^{2-}}}$$

The chemical composition of seawater remains fairly constant, which suggests that the variations in the equilibrium constants are only a function of temperature, salinity and pressure (Loewenthal and van Rooyen Marais, 1976, Zeebe and Wolf-Gladrow, 2001).

The total hydrogen ion pH scale

For calculations of the carbonate equilibria in seawater, pH is defined on the total hydrogen ion scale under the constant ionic medium approach. Introduced by Hansson (1973), the total pH scale (pH_T) was developed based on artificial seawater where the "activity coefficient approaches unity when total H^+ concentration tends to zero in pure synthetic seawater". The standard pH buffers introduced by Hansson reduced the liquid junction potential between the sample and the buffer due to the similarity of the buffers to the seawater medium (Zeebe and Wolf-Gladrow, 2001):

$$pH_T = -\log[H^+]_T = -\log\left([H^+]_F + [HSO_4^-]\right) \quad (14)$$

This was an improvement on the previous National Bureau of Standards (NBS) pH scale which had large deviations between low ionic strength standard buffers and the high ionic strength seawater being measured, which lead to irreproducible changes in the liquid junction potential.

The measurement of seawater pH

As a master variable to quantify the carbonate system in the ocean, pH is an important factor to measure. Early on, potentiometric methods of determining pH with glass electrodes proved problematic as the sensors were subject to drift and produced poor quality measurements as the electrodes were difficult to calibrate in the seawater medium. Thus, the vast majority of pH measurements were determined by the spectrophotometric method refined by (Clayton and Byrne, 1993), however, this method was confined to ship-based measurements. Autonomous samplers integrated with spectrophotometric analysers were employed later on to reduce the spatial variability of the pH measurements, this involved the use of indicator dyes being pumped into seawater samples and mixed. These measurements, although improved for *in situ* analysis (Liu et al., 2006, Seidel et al., 2008), were not continuous and limited by slow response times due to the need for blank measurements to be taken between samples, and required the maintenance of complex systems (Martz et al., 2010).

The need for a rapid response, high precision and simple operation system was met in the early 2000s with the development of the metal oxide semiconductor field effect transistor (MOSFET). This semiconductor device proved highly sensitive to changes in conductivity of the n-channel which varied by the amount of electrical potential applied between the gate and the source electrodes. The semiconductor was modified by replacing the metal gate over the

conductivity channel with a layer of amphoteric substrate, usually, silicon nitride (Si_3N_4). This modified MOSFET is known as an ion-selective field effect transistor (ISFET) and is sensitive to changes in pH of the analyte solution (Martz et al., 2010, Skoog, 2004).

Commonly used for the determination of pH, the ISFET sensor has been applied to ocean-based measurements due to its sensitivity, low electrical impedance, ruggedness in harsh environments, quick response time and the ease of integration with electronic measurement devices.

The ISFET sensor exploits the sensitivity of the n-channel to changes in electrical potential of the gate i.e. the conductivity of the device. Variations in the gate voltage of the ISFET are based on the concentration (or more accurately, the activity) of the analyte ions in the solution, thus enhancing the conductivity of the n-channel which can be measured electronically (Skoog, 2004).

Consider a solution of hydronium ions in contact with the gate insulator and reference electrode shown in Figure 1.7. The hydronium ions become adsorbed onto the Si_3N_4 gate insulator, thus altering the concentration (and activity) of the solution. The change in the electrochemical potential at the source and the gate gives rise to the change in the conductivity of the channel. The measured electronic signal arising from the change in conductivity is proportional to the logarithm of the activity of the hydronium ion in the analyte solution (Skoog, 2004). Instrumentation and calculations associated with the measurement of pH in seawater are detailed in Section 3.2.4.

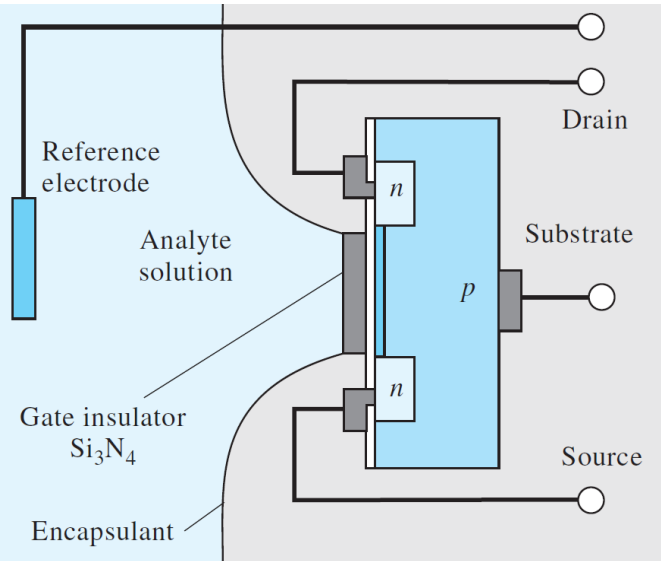

Figure 1.7: Cross-section of an ISFET pH sensor

Partial pressure of carbon dioxide in seawater

The partial pressure of carbon dioxide (pCO_2) is the concentration of dissolved gaseous carbon dioxide that is in equilibrium with seawater at a given temperature and salinity. The pCO_2 of seawater is related to atmospheric CO_2 by Henry's Law, which can be used to calculate the concentration of aqueous CO_2 present in seawater (Emerson and Hedges, 2008, Zeebe and Wolf-Gladrow, 2001):

$$pCO_2 = \frac{[CO_2{}^*]}{K_0} \tag{15}$$

However, the relationship between pCO_2 and the DIC concentration is not as straightforward as this equation suggests. It is better expressed in terms of the concentration of HCO_3^- and CO_3^{2-} ions present in seawater and the equilibrium constants, K_0, K_1 and K_2:

$$pCO_2 = \frac{K_2}{K_0\,K_1}\frac{[HCO_3{}^-]^2}{[CO_3{}^{2-}]} \approx \frac{K_2}{K_0\,K_1}\frac{(2\,DIC - Alk)^2}{Alk - DIC} \tag{16}$$

This equation shows that the factors affecting the distribution of pCO_2 in the surface ocean are complex, in addition to the initial DIC concentration of the seawater, each of the terms in the equation are subject to temperature, salinity and biological uptake, which in turn, have an impact on the pCO_2. We have already established that K_0 has a strong dependence on temperature, and this is largely responsible for the variations in pCO_2, whereas the ratio of K_2/K_1 show a stronger influence from salinity (Sarmiento and Gruber, 2013).

The temperature dependence of pCO_2 is important for the correction process for calculating pCO_2 from the analytical determination of the dry mole fraction of CO_2 (Section 3.2.4). The contribution of temperature to the changes in pCO_2 were quantified by Takahashi et al. 2003, which showed that for a 1 °C change in temperature at a pCO_2 of 400 µatm, there would be a change in pCO_2 of ~ 17 µatm. This relationship is expressed by the logarithmic function (Sarmiento and Gruber, 2002):

$$\frac{1}{pCO_2}\frac{\delta pCO_2}{\delta T} = \frac{\delta lnpCO_2}{\delta T} \approx 0.0423\ °C^{-1} \tag{17}$$

Whether or not the ocean is a sink or a source of CO_2 to the atmosphere is determined by calculating the air-sea flux of pCO_2. A negative value indicates that the ocean is a sink for CO_2 from the atmosphere, and a positive value indicates that the ocean is a source of CO_2 to the

atmosphere, when the ΔpCO_2 is $pCO_{2SW} - pCO_{2ATM}$. The air-sea flux of pCO_2 (FCO_2) is estimated by the equation:

$$FCO_2 = k\, K_0 (pCO_{2\,SW} - pCO_{2\,atm}) \quad (18)$$

where k is the gas transfer velocity as a function of wind speed (Wanninkhof, 1992) and K_0 is the solubility of CO_2 in seawater as a function of temperature and salinity. These values vary regionally depending on the dominant mechanisms at play, as well as the seasonal distribution of pCO_2.

In summer, the increase in the sea surface temperature creates a stratified water column which increases biological uptake of DIC due to increased photosynthesis in the thin surface layer. This depletes DIC in the surface ocean, which is not replenished through upwelling due to the stratified water column. The rise in temperature impacts the K_0 equilibrium constant by reducing the solubility of CO_2 in the surface ocean. The shallow mixing in regions such as this indicate that pCO_2 in the surface ocean is under-saturated relative to the atmosphere, suggesting that the region becomes a sink for CO_2. Thus, the summer season is driven by temperature and productivity (Sarmiento and Gruber, 2013, Le Quéré et al., 2007).

Conversely, the winter season is driven by temperature and upwelling and entrainment. Sea surface temperatures decrease, increasing the gradient of CO_2 solubility and deepening the mixed layer. Upwelling of deep water to the surface ocean increases the DIC concentration, indicating that the surface ocean is saturated with pCO_2 relative to the atmosphere. This suggests that these regions are a source of CO_2 to the atmosphere due to outgassing (Sarmiento and Gruber, 2013, Gray et al., 2018).

Ice formation in winter at high latitudes increases the density of surface waters due to brine rejection, facilitating the drawdown of CO_2 into the deep ocean (Talley, 2011). The ice also acts as a barrier between the ocean and the atmosphere, preventing the air-sea flux of CO_2. Conversely, ice melt during the summer increases air-sea gas exchange as the surface ocean directly interacts with the atmosphere, which leads to the outgassing of CO_2. This is also coupled with biological uptake of CO_2 in the summer as the sun is able to penetrate the thinning ice (Bakker et al., 2008, Gray et al., 2018).

The SOCCOM project has recently released a number of studies which report on the year-round measurements of salinity, temperature, pH and nitrate throughout the Southern Ocean.

This gives us the first comprehensive insights into the seasonal and zonal distribution of carbonate variables (calculated from pH_T and estimated TA) in the ACC, especially during the winter season. Gray et al., (2018) resolve the predominant seasonal mechanisms in the STZ, SAZ, PFZ, ASZ (Antarctic-Southern Zone) and SIZ. The STZ shows significant uptake of CO_2 during winter, with a smaller flux during the summer which indicates a temperature-driven change in solubility. The SAZ shows strong uptake to CO_2 during the spring-summer and outgassing of CO_2 in winter which indicates the influence of transport and biological activity. The PFZ shows a similar trend to the SAZ, with a larger outgassing of CO_2 in the winter season, corresponding to a greater component of the upwelling of deep waters in this region. The ASZ shows a consistent outgassing trend of CO_2 from the surface ocean, which peaks in the winter and lessens in the summer that indicates the influence of transport and biological activity. Ice cover in the SIZ suppresses the winter air-sea flux of CO_2, with significant uptake during spring and outgassing of CO_2 in the autumn prior to the onset of ice formation.

The float-based measurements when compared to ship-based measurements show a discrepancy between the calculated pCO_2 and *in-situ* measurements of pCO_2. Gray et al. 2018 indicate that the floats show a consistently higher value of pCO_2 compared to ship measurements. However, owing to the summer-bias of ship measurements, these values may be skewed due by the interpolation method used calculate TA, and subsequently estimate pCO_2. This thesis makes a direct comparison of winter ship-based measurements taken aboard the R/V *SA Agulhas II* during June-July 2016/7, against the float-calculated pCO_2 values that coincide with the ship transects in space and time.

Total Alkalinity

Total alkalinity (TA) is a carbonate parameter than can be measured with great accuracy by Gran-type titration in seawater (Dickson et al., 2007). In simple terms, TA is the measure of the excess proton acceptors (bases) over proton donors (acids) in a sample of seawater (Dickson et al., 2007) with the advantage that it is insensitive to temperature, pressure and CO_2 changes (Wolf-Gladrow et al., 2007).

The titration of a sample solution with a strong acid, such as HCl, can be seen as the addition of protons to the solution. The added protons neutralise the bases present in solution e.g. CO_3^{2-} and HCO_3^-. In a complex system such as seawater, there are a number of weak acid-base systems to consider that contribute to TA, namely: carbonate, borate, phosphate, sulphate, nitrate and water (Wolf-Gladrow et al., 2007).

Dickson et al. (2007) defines conservative TA as the sum of the following ions in seawater according to standard operating procedure (SOP) 3a of Dickson and Goyet (1994):

> "The total alkalinity of a sample of sea water is defined as the number of moles of hydrogen ion equivalent to the excess of proton acceptors (bases formed from weak acids with a dissociation constant $K < 10^{-4.5}$ at 25 °C and zero ionic strength) over proton donors (acids with $K > 10^{-4.5}$) in one kilogram of sample." (Dickson, 1981)

$$\begin{aligned} TA &= proton\ acceptors - proton\ donors \\ &= [HCO_3^-] + 2[CO_3^{2-}] + [B(OH)_4^-] + [OH^-] + [HPO_4^{2-}] + 2[PO_4^{3-}] \\ &\quad + [H_3SiO_4^-] + [NH_3] + [HS^-] - [H^+]_F - [HSO_4^-] - [HF] \\ &\quad - [H_3PO_4] \end{aligned} \tag{19}$$

where the bracketed constituents represent total concentrations in solution and $[H^+]_F$ is the free concentration of hydrogen ion. The chosen dissociation constant at pK = 4.5 defines a zero level of protons that classifies chemicals species into proton donors, acceptors and neutral species for each of the acid-base systems which contribute to TA. The definition of TA is dependent on the chosen zero level of protons (Wolf-Gladrow et al., 2007).

The zero level of protons is unique to each acid-base system under consideration. Usually taken as the neutral chemical species, the ionised forms of the species are then classified as a proton donor or proton acceptor relative to this. A relation between the relative acid-base systems and the choice of species taken as the zero level of protons can be specified via a

chosen pK value, denoted as pK_{zlp}. The pK_{zlp} acts as a defining point to separate proton donors (with $pK < pK_{zlp}$) from proton acceptors (with $pK > pK_{zlp}$) (Wolf-Gladrow et al., 2007).

At a seawater pH of 8.2, the dominant acid-base system (the largest concentration) is that of the carbonate species. As such, the pK_1 value for CO_2 at ~ 4.5 is taken to be the zero level of protons – when the carbonate weak acid system is completely converted to $H_2CO_3^*$ (Wolf-Gladrow et al., 2007).

pK_{zlp} = 4.5 was chosen by Dickson 1981 based on thermodynamic pK values at standard temperature and pressure (25 °C, 1 atm) and zero ionic strength. This value was ideally selected as it applies to both the stoichiometric conventions used in natural waters, as well as the thermodynamic constraints used in seawater. The chosen pK_{zlp} leads to the same division between the acidic basic species in the respective systems (Wolf-Gladrow et al., 2007).

Explicit conservative expression for total alkalinity

The expression for the TA proposed by Dickson contains the concentrations of non-conservative chemical species i.e. the individual chemical species that define TA are dependent on temperature and pressure. An alternate expression for TA can be attained by combining the conventional expression for TA (Eq. 19) with the broader relation of electroneutrality (Eq. 20) to yield an expression for TA which contains only conservative ions, denoted as TA_{ec} (Eq. 21). The relation of electroneutrality states that the sum of charges of the respective chemical species are zero for aqueous solutions according to equation 20:

$$\sum_i q_i[C_i] = 0 \tag{20}$$

where q is the electric charge of the respective chemical species, and C is the concentration of the respective species.

TA_{ec} is known as the explicit conservative expression for TA. TA_{ec} is equivalent to TA, however, it is more useful for quantitatively assessing the changes in TA due to biological processes (Wolf-Gladrow et al., 2007, Zeebe and Wolf-Gladrow, 2001).

$$\begin{aligned} TA_{ec} = {} & [Na^+] + 2[Mg^{2+}] + [K^+] + 2[Sr^{2+}] + \cdots + [NH_4{}^+] + \cdots - [Cl^-] \\ & - [Br^-] - [NO_3{}^-] - \cdots TPO_4 + TNH_3 - 2TSO_4 - THF \\ & - THNO_2 \end{aligned} \tag{21}$$

where

$$TPO_4 = [H_3PO_4] + [H_2PO_4{}^-] + \left[HPO_4{}^{2-}\right] + \left[PO_4{}^{3-}\right]$$

$$TNH_3 = [NH_4{}^+] + [NH_3]$$
$$TSO_4 = [SO_4{}^{2-}] + [HSO_4{}^-]$$
$$THF = [F^-] + [HF]$$
$$THNO_2 = [NO_2{}^-] + [HNO_2]$$

are total phosphate, ammonia, sulphate, fluoride and nitrite, respectively. The derivation of TA_{ec} (Eq. 21) from Eq. 19 and Eq. 20 is outlined in Appendix A.

Changes of total alkalinity in seawater

Variations in TA are governed by processes which are able to drive changes in the charge difference between the conservative ions which make up TA. The main drivers for changes in TA are summarised as follows:

1. Salinity

   Fluctuations in salinity affect the charge difference between conservative cations and anions, thus TA is closely linked to changes in salinity, which can be caused via precipitation, evaporation, fresh water input, formation and melting of sea ice. (Zeebe and Wolf-Gladrow, 2001)

2. Production/dissolution of calcium carbonate

   The precipitation of calcium carbonate ($CaCO_3$) by marine organisms drives a decrease in the concentration of Ca^{2+} ions, this leads to a decline in the charge difference between conservative ions and therefore decreases TA. Conversely, the dissolution of $CaCO_3$, calcareous shells and skeletons at depth would drive an increase in TA as the Ca^{2+} concentration increases, TA is seen to increase in the surface ocean in regions of upwelling. (Zeebe and Wolf-Gladrow, 2001, Wolf-Gladrow et al., 2007, Millero et al., 1998).

3. Uptake of nutrients

   Changes in TA can be caused by the uptake of nutrients, depending on the reactive forms of nitrogen produced by biological reactions taking place. This is governed by the "nutrient-H+-compensation principle" proposed by Wolf-Gladrow et al., 2007. Increases in TA are calculated for nitrate, phosphorus and sulfate reduction. Decreases in TA are calculated by the remineralization of these processes, as well as N_2 fixation and nitrification (Brewer et al., 1986, Brewer et al., 1975, Chen, 1978, Brewer and Goldman, 1976, Goldman and Brewer, 1980, Wolf-Gladrow et al., 2007).

Observed and derived methods for the estimation of total alkalinity

The concentration of TA in a sample of seawater is typically determined by differential potentiometric (Gran-type) titration against 0.1 M HCl. TA can be measured at a precision of ~ 2 μmol/kg in the surface ocean (Watanabe et al., 2004). This method of measuring TA is limited by the number of samples that can be collected, analysed, as well as the amount and cost of chemicals and certified reference materials available.

Millero et al., (1998) first proposed an algorithm for estimating TA in the surface ocean based on the relationships which exist between TA, salinity, and temperature. Algorithms for TA are particularly useful for estimating the distribution of other carbonate variables in the surface ocean when only one other carbonate variable is measured e.g. underway fCO_2 measurements. However, the algorithm pertaining to the Southern Ocean region is based on observations of TA collected in the Indian Ocean sector during the onset of austral winter, and the Atlantic and Pacific Ocean sectors during the austral summer. Based on this, Millero et al., (1998) assume that the algorithm is seasonally robust, despite the differences in region owing to the salinity-normalisation of the dataset.

A later version of the TA global relationship algorithm (adjusted for each oceanic regime) proposed by Lee et al., (2006) is based on surface ocean measurements of salinity and temperature, taken from the global carbon survey between 1990-1998 (JGOFS, WOCE). However, the seasonal bias of this dataset toward the Southern Ocean is of particular concern for resolving the winter seasonal changes in TA.

The locally interpolated alkalinity regression (LIAR) method for global alkalinity estimation developed by Carter et al. (2016) is an algorithm based on the GLODAPv1.1 (Key et al., 2004), CARINA (Anton et al., 2010) and PACIFICA (Suzuki et al., 2013) datasets from 1990 onwards. The LIAR method interpolates the regression coefficients of the TA algorithm to the location of interest, as opposed to having a generalised algorithm pertaining to the large spatial areas of each ocean basin. This is the case for the SOCCOM float project which only measures pH in the water column over a 10-day period. The pH measurement is combined with a TA algorithm, such as the SOCCOM-specific algorithm used by Williams et al., (2017), or LIAR (Carter et al., 2016) to calculate pCO_2.

The accuracy of TA estimated by these algorithms for the Southern Ocean, particularly in context of strong regional heterogeneities, is still unknown. It is necessary to look closer at how the seasonal biases in the surface ocean sampling are affecting the validity of these

algorithms, particularly in the winter season of the under-sampled Southern Ocean regime. Salinity and temperature data are easily attainable measurements for autonomous systems, such was the Wave Glider and SOCCOM floats, in comparison to direct measurements of TA which are discrete in nature. For this reason, as well as the available datasets for the scope of this study, we have selected the Lee et al., (2006) formula to calculate TA for comparison with the LIAR formula utilized by the SOCCOM floats to assess the seasonal bias and accuracy of these algorithms for TA to predict changes in sea surface pCO_2 of the Southern Ocean.

2 Problem statement

Although there has been an increase in global observational data collection for surface ocean pCO_2 over the past two decades through initiatives such as the Joint Global Ocean Flux Study (JGOFS), the Surface Ocean CO_2 Atlas (SOCAT) (Bakker et al., 2016) and the World Ocean Circulation Experiment (WOCE), the Southern Ocean is still largely under-sampled and subject to seasonal, spatial and temporal biases (Gray et al., 2018, Gregor et al., 2018). Transects to and from the Antarctic continent are repeat voyages travelled mainly in the summer season when the Southern Ocean is less hostile and the continent is once again accessible when ice coverage has receded, which creates a seasonal bias in ship-board observations.

As such, the SO is still largely under-sampled in the winter season – the harsh weather conditions experienced in the SO emphasize the need for the use of autonomous measuring systems to gather more observational data at higher resolutions in under-sampled locations. A large scale initiative to gather more data in the SO all year round was undertaken by the SOCCOM Project biological profiling float array (Group, 2016). However, these floats can only measure one carbonate parameter of seawater, pH. There exist empirical algorithms for TA (Lee et al., 2006, Carter et al., 2018) which can be calculated from other measured seawater parameters (T, S, P, NO_3^- and O_2). Estimates of pCO_2 are then calculated from the measured pH and calculated TA.

Given the summer bias in seasonal data for the SO regime, this study will investigate whether or not empirical algorithms of TA are correct throughout the seasonal cycle, as well as assess the effects of the seasonal cycle of TA on the resultant estimates of pCO_2 during the austral winter in the SO.

2.1 Aims

The first aim of this study is to examine whether pH is a viable measurement to estimate pCO_2 concentrations in the surface ocean (Gray et al., 2018). What is the seasonal cycle of the TA? Can pH be used with estimated TA to accurately reconstruct the seasonal variations in pCO_2?

The second aim of this study is to determine whether TA algorithms based on measurements of temperature and salinity (Carter et al., 2016, Williams et al., 2016, Lee et al., 2006) are accurate enough to resolve the concentration of TA in the surface layer of the Southern Ocean during the winter season. Does the Lee formulation need to be re-evaluated based on observations emerging from the Southern Ocean in the winter season? What biogeochemical or physical factors are influencing the increased drawdown of pCO_2 during winter? What is the impact of using a regionally averaged algorithm for TA on the seasonal variations of TA in the surface ocean?

The last aim of this study is to determine compare estimates of pCO_2 calculated from the seawater parameters measured by SOCCOM floats, with *in situ* shipboard and WG measurements of pCO_2. How do *in situ* ship-board measurements of pCO_2 compare to float-based calculations of pCO_2 during the winter season? What impact does derived TA in winter have on estimating pCO_2 from pH and TA?

2.2 Approach

Data collected by the Southern Ocean Carbon-Climate Observatory (SOCCO) at the Council for Scientific and Industrial Research (CSIR) through Wave Glider (WG) deployments (pCO_2, pH, T, S), shipboard underway sampling (DIC, TA) and continuous *in situ* analysis (pCO_2) provide a high resolution estimate for carbonate chemistry in the SAZ, the PFZ, the PUZ and the MIZ in the Southern Ocean. The duration of this study spans the time period from summer 2013/14 and winter 2015-2017 in the Southern Ocean. In addition to this, we will use SOCCOM float data which is made freely available by the SOCCOM Project funded by the National Science Foundation, Division of Polar Programs (NSF PLR -1425989), supplemented by NASA, and by the International Argo Program and the NOAA programs that contribute to it.

This study will use three distinct datasets to investigate three main research questions, namely:

1. Can pH be used to estimate seasonal variations in pCO_2?
2. What is the performance of the Lee formula in austral winter across the Southern Ocean?
3. How do SOCCOM results compare to ship- and glider-based measurements?

This study will investigate the accuracy of predicting surface ocean pCO_2 from pH measurements obtained from the WG and empirically derived TA, at the SOCCO reference station, located at 43 °S; 8.5 °E. Ship-board measurements from winter cruise data will be compared to the Lee et al., (2006) expression for TA in the Atlantic and Indian Ocean sectors of the SO to determine its performance in the winter season. Finally, we will investigate the SOCCOM float measurements and calculated pCO_2 against ship- and glider-based measurements to determine the impact of the seasonal cycle of TA on the estimation of pCO_2 in winter.

A literature review is presented in Chapter 1, addressing the context of the Southern Ocean in the global carbon cycle, the marine carbonate system in seawater, and the physical and chemical characteristics at play in the Southern Ocean. Chapter 2 outlines the key aims and research questions addressed in this study. Chapter 3 outlines the *in situ* and discrete observations carried out during sample collection of the data, the experiments undergone to analyse the samples in the context of this study, and the methods used to process the collected data. Chapter 4 presents an analysis of the results obtained from direct measurements and calculations. Chapter 5 poses a discussion of the results framed toward answering the proposed research questions. Finally, Chapter 6 concludes the findings of this study and puts forward recommendations for future related research.

3 Methods

3.1 Data collection

3.1.1 Wave Glider measurements

This study utilizes data collected from a Liquid Robotics SV2 Wave Glider (WG), deployed from the R/V *SA Agulhas II*, during the second Southern Ocean Seasonal Cycle Experiment (SOSCEx II) in the sub-Antarctic zone of south of Southern Africa (Monteiro et al., 2015). The WG was deployed on 13 October 2013 at 41 °S, 9.5 °E and piloted in a quasi-circular sampling pattern centred at the SOCCO station (43 °S, 8.5 °E) with a diameter of 16 km (Figure 3.1). The glider arrived at this position on 17 November 2013 and the experiment terminated on 08 February 2014. The WG was deployed with a modified MAPCO$_2$ surface CO_2 sensor (Sutton et al., 2014) to measure the pCO_2 in seawater, and a Honeywell Durafet® pH sensor (Martz et al., 2010) to measure the pH_T of seawater. These measurements were taken at hourly intervals over the course of the four month experiment. TA and DIC were calculated from the *in situ* pCO_2 and pH_T measurements collected by the WG. TA was also calculated from the *in situ* measurements of salinity and temperature according to the (Lee et al., 2006) T-S relationship for TA in the Southern Ocean.

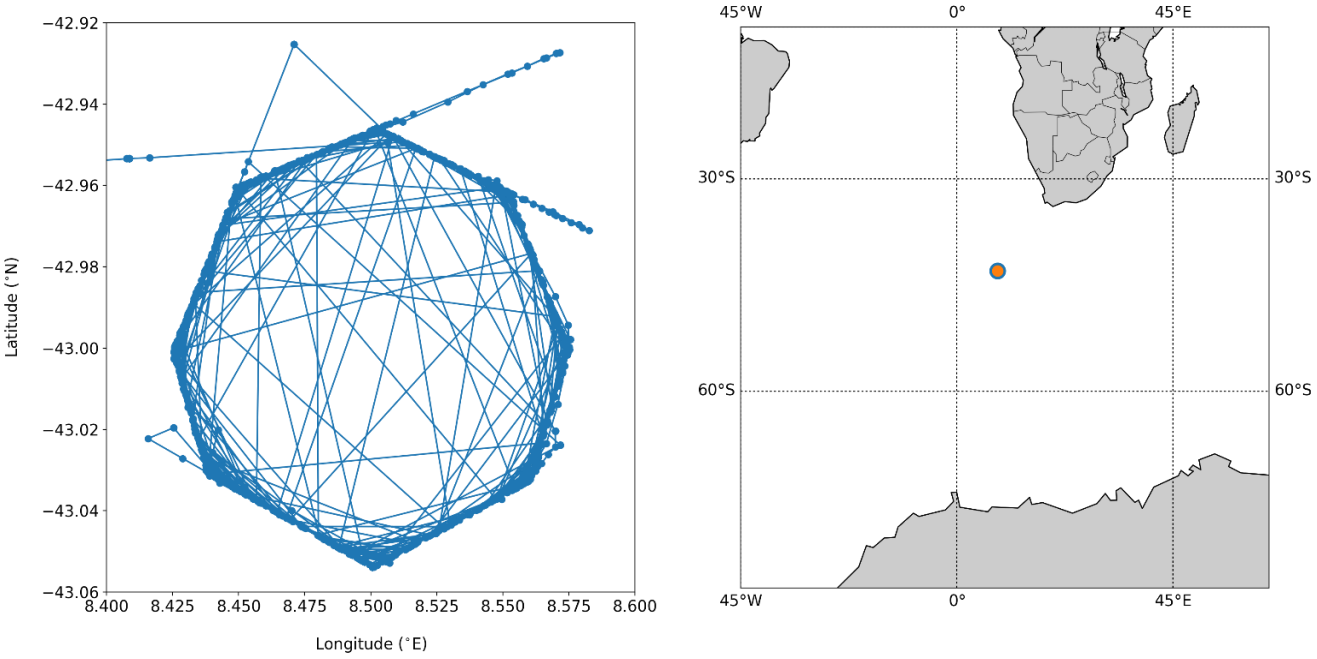

Figure 3.1: The position and sampling pattern followed by the Wave Glider centred at the SOCCO station (43 °S, 8.5 °E) in the sub-Antarctic zone of Southern Africa from Oct 2013 - Feb 2014

3.1.2 Ship-board measurements

The R/V *SA Agulhas II* traversed the Good Hope Line, from Cape Town to Neumayer Station on Antarctica, in the early winter seasons from 2015 – 2017 (as shown in Figure 3.2). Discrete samples of seawater were collected for DIC, TA and salinity via the ship's underway (UW) system at 4 hour intervals, and from the deployment of the CTD rosette at pre-determined stations as indicated on Figure 3.2. Continuous measurements of pCO_2 (1 minute intervals) were recorded along the Good Hope transect by means of an autonomous underway measuring system. The pCO_2 system was only switched on after the ship had left the harbour, and switched off once the ship had reached pack-ice.

In addition to sampling along the Good Hope Line on the journey down to the marginal ice zone (MIZ) in 2017, the R/V *SA Agulhas II* also sampled (UW and CTD) along the WOCE IO6 transect on its journey back to Cape Town (the green line on Figure 3.2).

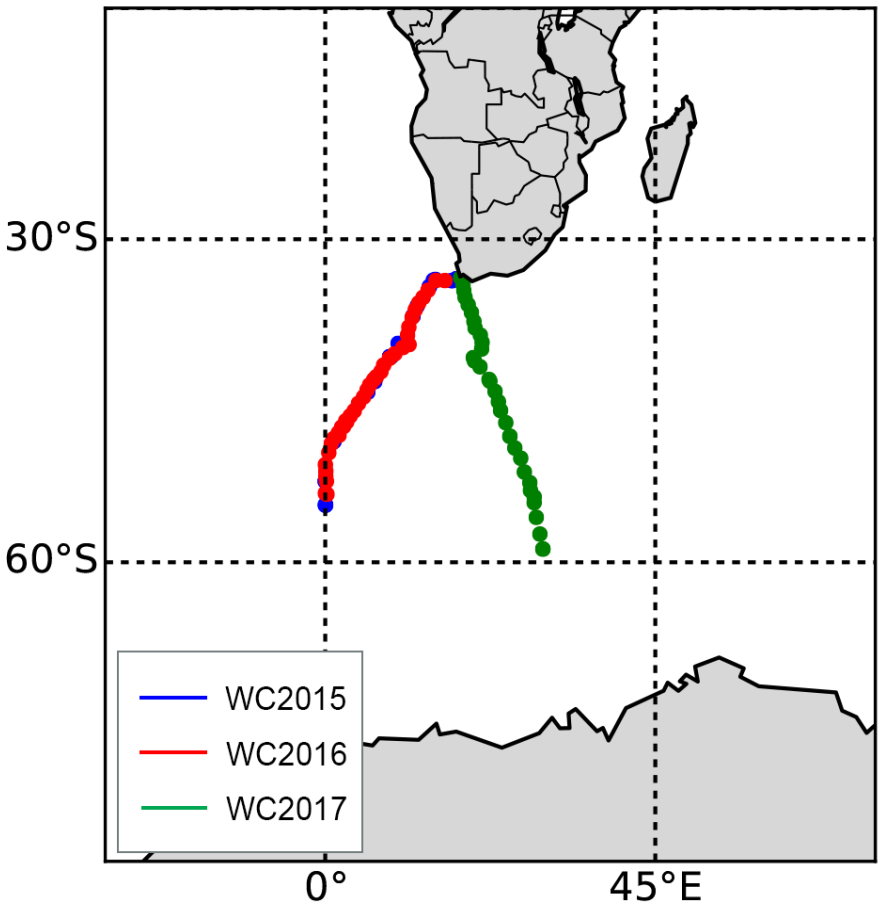

Figure 3.2: Transects for the R/V *SA Agulhas II* from Winter Cruise 2015 - Winter Cruise 2017

Table 3.1: Summary of cruise duration for the winter season from 2015 – 2017

Cruise	Start Date	End Date
Winter Cruise 2015 (WC2015)	24/07/2015	13/08/2015
Winter Cruise 2016 (WC2016)	15/07/2016	27/07/2016
Winter Cruise 2017 (WC2017)	28/06/2017	13/07/2017

3.1.3 The SOCCOM Project

The Southern Ocean Carbon and Climate Observation Modelling (SOCCOM) project biogeochemical profiling floats were chosen on the basis that the floats were fitted with Deep-Sea DuraFET pH sensors (Johnson et al., 2016). Secondary criteria was based on the location of the floats which overlapped with the selected winter cruise transects and the position of the wave glider i.e. longitude 0 – 45 °E and latitude 30 – 60 °S. The data collected by these floats was further constrained to surface measurements of 5 m, and valid pH measurements on the total pH scale.

The stations for each float pertaining to these criteria are shown in Figure 3.3. The selected floats are summarised in Table 3.1, showing the date when the float began taking measurements, the date for the most recent data available for each float at the time of this study, and the number of winter time surface measurements (to a depth of 10 m) taken by each of the floats. Calibration and validation protocol for the deployment of the SOCCOM floats is outlined in (Wanninkhof et al., 2016, Riser et al., 2017).

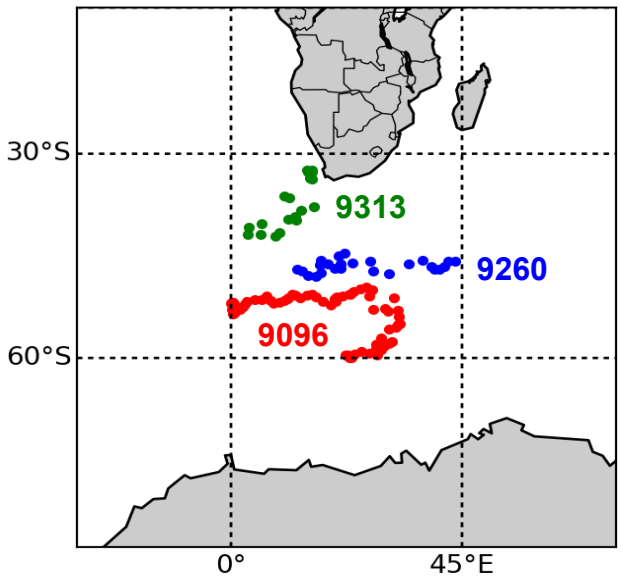

Figure 3.3: Position of the SOCCOM profiling floats operating within the region of study

Table 3.1: Selected SOCCOM profiling floats within the region of study during the winter season

Float ID	Start	End	No. of winter measurements
9096SOOCN	11/12/2014	22/04/2018	2
9260SOOCN	28/01/2015	23/07/2017	2
9313SOOCN	07/12/2014	30/04/2018	3

3.2 Sample Analysis

3.2.1 The carbonate system in seawater

The Versatile INstrument for the Determination of Total inorganic carbon and titration Alkalinity (VINDTA) 3C is designed to determine the TA and DIC concentrations of a seawater sample by means of differential potentiometric titration and coulometric titration respectively.

The VINDTA 3C instrumentation was designed by Ludger Mintrop and Marianda Marine Analytics and Data. The operation and setup of the VINDTA 3C system is in compliance with the accompanying manual authored by Ludger Mintrop (Mintrop, 2010).

Seawater samples collected for DIC and TA analysis are in compliance with SOP 1, SOP 2 and SOP 3b outlined in the Handbook of Methods for the Analysis of the Various Parameters of the CO_2 System in Seawater (Dickson and Goyet, 1994). Each seawater sample is poisoned with mercuric chloride to arrest biological activity.

3.2.2 Total alkalinity

The TA concentration is determined by differential potentiometric titration of a seawater sample with 0.1 M pure HCl. 100 mL of seawater is pipetted into a custom-built alkalinity open titration cell over a magnetic stirrer. The 0.1 M HCl is dispensed in 0.150 mL volumes by a Metrohm 702 SM Titrino to the titration cell.

The potentiometric changes in the solution are recorded in mV as acid is added to the solution. Changes in the potential of the solution are detected by a combination of three electrodes: the Metrohm double junction electrode (reference electrode), the Orion Ross-electrode (glass electrode) and an electrode of shielded titanium metal (auxiliary electrode).

The Metrohm double junction electrode is filled with a 0.7 M NaCl solution in the outer jacket and 3.0 M KCl solution in the inner jacket. The inner jacket solution is changed weekly to avoid crystallization of the salt, and the outer jacket is changed daily as it exchanges with the sample solution in the titration cell.

The glass electrode and the reference electrode are used in combination to achieve high resolution potential measurements needed to detect the relevant end points between the different carbonate species. The auxiliary electrode is essential for counteracting the electrical ground signal produced through the nature of the flow system by means of the peristaltic pump

apparatus which delivers the seawater to the pipettes and cells. The differential nature of the titration helps to alleviate this drift by measuring the glass electrode and the reference electrode against the auxiliary electrode. The sample undergoes a 25 point titration and uses a method of non-linear least squares and the Gran method (Appendix A, Section A1) function to calculate TA, as described in SOP 3b of the Handbook (Dickson and Goyet, 1994).

3.2.3 Total dissolved inorganic carbon

The DIC concentration is determined by coulometric titration of the carbon dioxide gas evolved from a mixture of the seawater sample with 8.5 % (v/v) phosphoric acid and absorbed into an aqueous solution of monoethanolamine (MEA).

The reaction of the seawater with a strong acid (influx of protons) drives the reverse equilibrium reaction to evolve carbon dioxide gas (CO_2):

$$HCO_3^- + H^+ \rightleftharpoons CO_{2\,(aq)} + H_2O \rightleftharpoons CO_{2\,(g)} \qquad (22)$$

A fixed volume of 8.5 % phosphoric acid (H_3PO_4) is dispensed into the stripper cell and 20 mL of the seawater sample is dispensed to the cell via peristaltic pump and pipette. The evolved CO_2 gas is carried through a peltier (set at 2-3 °C) by the nitrogen carrier gas flowing through the system (Lei and Xian-kun, 1997).

The dried CO_2 gas is directed to the coulometer cell housed in the UIC 5011 Coulometer by the constant flow of the carrier gas. The CO_2 gas is bubbled through a solution of (MEA) in the cathode compartment of the coulometer cell. The CO_2 is absorbed into the MEA to form an acid:

$$CO_2 + RNH_2 \rightleftharpoons RNHCO_2H$$
$$RNHCO_2H + RNH_2 \rightleftharpoons RNHCO_2^- + RNH_3^+ \qquad (23)$$

R = C_2H_5 (Xie et al., 2010)

The resulting acid is titrated against OH^- generated at the platinum spiral cathode of the coulometer cell when a current is running through it. Upon completion of the titration, the solution will once again turn from colourless to blue as all the "CO_2" is neutralized i.e. at the end point. The reaction of OH^- with RNH_3^+ will regenerate MEA, thus returning the solution to its blue colour. The amount of charge (raw electron counts) required to generate OH^- at the

cathode until the acid is neutralized is the quantitative measurement registered by the computer (Lei and Xian-kun, 1997, Xie et al., 2010).

The raw electron counts are converted by the VINDTA LabView software to a concentration in μmol/kg according to the equation outlined in Dickson and Goyet (1994):

$$C_T = \frac{N_s - bt - a}{c} \times \frac{1}{V_s \rho} \quad (24)$$

where C_T is the total dissolved inorganic carbon concentration of the sample in μmol/kg, N_s is the raw electron count for the seawater sample, b is the background reading for the system in counts/min, t is the time taken measure the sample in min, a is the acid blank raw electron count, c is the coulometer calibration factor in counts/min, V_s is the volume of the seawater sample at 25 °C in dm^3 and ρ is the density of the seawater sample in g/cm^3.

Certified reference materials

For quality control purposes, certified reference materials (CRMs) obtained from the Scripps Institute of Oceanography were used as a means of calibration to measure the accuracy and precision of the VINDTA 3C system. A duplicate analysis of each CRM was carried out before and after each batch of samples (approximately 12 samples per batch), and as required when the coulometer cell was changed to test the reproducibility of the measurements. The CRM batch numbers pertaining to the analysis for each cruise are outlined in Table 3.2.

Adjustments to the acid concentration factor were carried out on the data obtained for the CRM measurements. This was done post-analysis to account for evaporation or addition of acid to the titrant supply in the case of TA, in order to achieve the certified value. In the case of DIC, a linear correction factor was applied. The sample data were corrected using an average of the CRM corrections calculated between sample batches. The recalculation of the sample data was carried out using the VINDTA reCAlk package (Version 2.1) for Python 3.6+ developed by Dr Luke Gregor, available at: https://github.com/luke-gregor/vindta_reCAlk.

Table 3.2: Batch number for certified reference materials used during the analysis of seawater samples

Cruise	CRM Batch Number
SOSCEx II (2013/2014)	115
Winter 2015	143, 146
Winter 2016	143
Winter 2017	158

3.2.4 pCO_2 measurements in seawater

pCO_2 in seawater and the atmosphere was carried out from two platforms: the ship's underway (UW) system, and the Wave Glider (WG).

3.2.4.1 Autonomous underway pCO_2 measuring system

High resolution continuous measurements (1-2 min) of pCO_2 were taken by means of an autonomous UW measuring system, the General Oceanics GO-8050 fitted with a non-dispersive infrared (IR) LICOR® LI-7000 CO_2/H_2O Analyser, as described by (Pierrot et al., 2009).

A ~3 L/min flow of seawater was channelled into the equilibrator chamber where CO_2 in the seawater equilibrated with the headspace of the chamber. The resulting headspace gas was dried through a series of Nafion® tubes before being pumped through the IR analyser to determine the mole fraction of CO_2 (xCO_2) in seawater. The mole fraction of CO_2 in the atmosphere was determined by pumping a flow (~ 4 L/min) of atmospheric air through the analyser at regular intervals. The analyser was calibrated every 2.5-3 hours with four standard reference gases obtained from the Global Atmosphere Watch station at Cape Point.

3.2.4.2 Moored autonomous pCO_2 measuring system

The Wave Glider utilized in this study was deployed with a moored autonomous pCO_2 ($MAPCO_2$) sensor to measure surface ocean pCO_2 at a sampling frequency of 1 hour (Sutton et al., 2014). Like the ship-board autonomous underway pCO_2 measuring system, the $MAPCO_2$ sensor also uses the combination of an air-water equilibrator and a non-dispersive infrared (IR) analyser for the measurement of CO_2 in the gas phase. The functioning of the $MAPCO_2$ sensor is described in great detail by Sutton et al. (2014).

The IR analyser used in this system is the LICOR® LI-820 CO_2 gas analyser which requires the addition of a relative humidity (RH) and temperature sensor (Sensirion SHT71) to account for moisture in the gas stream. The analyser is calibrated by a zero standard gas and a standard reference gas obtained from NOAA's Earth System Research Laboratory (ESRL) before each measurement. The zero standard gas is generated by cycling air into a closed loop which is scrubbed of all CO_2 by means of a soda lime tube (Sutton et al., 2014).

To obtain the mole fraction of CO_2 in seawater (xCO_2), the MAPCO_2 system measures a closed loop of air that has been equilibrated with surface seawater within the h-shaped equilibrator. The air is passed through a silica drying agent to remove any condensation and the RH sensor to measure the moisture content of the air. This cycle is repeated for 10 min and the air then pumped to the IR analyser which records an average over 30 s. The mole fraction of CO_2 in air is measured by drawing air in through the air block and silica drying agent before being pumped through the IR analyser, and a 30 s average is recorded.

3.2.5 pH_T measurements in seawater

Measurements of pH_T were taken at hourly intervals with a Honeywell Durafet pH sensor fitted to the Wave Glider, and at ten day intervals for the surface ocean by the Deep-Sea DuraFET pH sensor deployed on the SOCCOM biological profiling floats.

3.2.5.1 Honeywell Durafet® ISFET sensor

The Honeywell Durafet® III sensor is made up of two cells in which the ion-selective field effect transistor (ISFET) is the working electrode compared to the internal reference electrode in the internal cell, and the external reference electrode in the external cell. The ISFET is sensitive to changes in the activity of the hydrogen/hydroxide ions present in solution. The measurement of this sensitivity is relayed by electronic signal which is detected by interaction of the ISFET with the internal and external reference electrodes (Martz et al., 2010, Scientific, 2018)).

The internal reference electrode consists of an Ag wire immersed in an AgCl and KCl saturated gel. This electrode is in contact with the sample solution by means of a liquid junction separated by an annular frit, and is sensitive to chloride ions present in solution.

The external reference is a chloride ion-selective electrode (Cl-ISE) developed in-house at the Monterey Bay Aquarium Research Institute (MBARI). The external reference electrode is expected to vary with the chloride concentration in the sample solution. Since the sample

solution in this case is seawater, the signal for the chloride concentration can be calculated based on the salinity of the sample. Thus, the remaining hydrogen/hydroxide ion signal can be obtained. The working principle behind the operation of the ISFET is outlined in Section 1.4. The calculation of pH_T from the recorded raw signal is outlined in Section 3.3.3.

3.2.5.2 Deep-Sea DuraFET pH sensor

The SOCCOM biological profiling floats utilize a pressure tolerant pH sensor, known as the Deep-Sea DuraFET, which can operate down to depths of 2000 m in seawater. The Deep-Sea DuraFET sensor is a Honeywell ISFET die (based on the commercial Honeywell Durafet ISFET sensor) housed within a pressure tolerant casing, coupled with a solid-state AgCl reference electrode that is able to withstand considerable temperature and pressure gradients (Johnson et al., 2016). The principle operation of this sensor is similar to that of the ISFET pH sensor described in Section 1.4.

The sensor was designed for use on Argo profiling floats which dive down to depths of 2000 m and are deployed for a number of years. The sensor has an accuracy of 0.01 pH_T units with a drift of -0.036 yr^{-1} for the early models of the sensor (Martz et al., 2010). With improved conditioning techniques, the drift has been reduced to less than 0.01 yr^{-1} (Wanninkhof et al., 2016, Johnson et al., 2016, Johnson et al., 2017). The calibration procedure and details of the pressure tolerant housing for the Deep-Sea DuraFET pH sensor are outlined in Johnson et al. (2016).

3.2.6 Carbonate variables in seawater

Using a combination of each of the measured carbonate variables (pH_T and TA, pCO_2 and TA, pCO_2 and pH_T), the remaining carbonate variables were calculated using the CO_2 Calc program (Robbins et al., 2010). pH_T was calculated on the total scale, and dissociation constants were based on Leuker et al., 2010. The cross-calculation of these measured variables were used to validate measurements and test our understanding of the carbonate chemistry in seawater. The calculations for the derivation of pCO_2 from TA and pH_T, and the derivation of pH_T from TA and DIC are outlined in Appendix A, Section A2.

3.2.7 Nutrient analysis

Nutrient analysis was carried out on discrete samples of seawater collected from the underway system and the CTD rosette to supplement the DIC and TA data to account for the effect of biology in the sample. Samples were analysed for nitrate, nitrite, phosphate and silicate.

3.2.7.1 Nitrate and nitrite

The determination of the concentration of nitrate in a sample of seawater was a two-step process. The concentration of nitrite was first measured spectrophotometrically at a wavelength of 543 nm by reacting the sample with sulphanilamide and N-1-naphthyl-ethylenediamine dihydrochloride (NEDI) to produce a pink hue (Strickland and Parsons, 1977). The concentration of nitrate in the sample was then determined by reducing all nitrate in the sample to nitrite by means of passing the sample through a copperized cadmium column using a Lachat Quick Chem Flow Analysis platform (Riley, 1976). The concentration of nitrite was then subtracted from this total value to isolate the concentration of nitrate.

$$[NO_3^-] = [NO_3^- + NO_2^-] - [NO_2^-] \quad (25)$$

3.2.7.2 Phosphate

The concentration of phosphate in seawater was determined by reacting a sample of seawater with a mixed reagent made up of ammonium molybdate, sulfuric acid, ascorbic acid and potassium antimonyl-tartrate (Strickland and Parsons, 1977). The reaction of seawater with the mixed reagent produces a blue hue which is directly proportional to the concentration of phosphate in the sample, which was measured by means of a spectrophotometer at a wavelength of 885 nm.

3.2.7.3 Silicate

The concentration of silicate in a sample of seawater was obtained by first reacting the sample with acid molybdate. The resulting product is then reacted with oxalic acid and ascorbic acid to form a blue hue (Riley, 1976). The colour intensity is directly proportional to the concentration of silicate in the sample, which was measured by means of a spectrophotometer at a wavelength of 820 nm.

3.3 Calculations

3.3.1 Global relationship for total alkalinity in the Southern Ocean regime

Lee et al., (2006) developed an empirical function for the estimation of TA in the surface ocean using measurements of salinity and temperature. The function was applied to global measurements of TA and correlated with salinity and temperature to generate an algorithm for each of the five ocean regimes. The Southern Ocean algorithm for sea surface TA is constrained to a latitude range from 30 – 70 °S, sea surface temperatures < 20 °C and sea surface salinity between 33 – 36 psu. The TA estimate has a weighted average uncertainty of ± 8.4 μmol/kg based on a sample set of 1708 surface TA measurements in the Southern Ocean regime. The algorithm for TA in the Southern Ocean is:

$$A_T = 2305 + 52.48\ (SSS - 35) + 2.85\ (SSS - 35)^2 - 0.49\ (SST - 20) + 0.086\ (SST - 20)^2 \qquad (26)$$

where **SSS** is the measured sea surface salinity in psu and **SST** is the measured sea surface temperature in °C.

3.3.2 Locally interpolated alkalinity regression (LIAR)

The locally interpolated alkalinity regression (LIAR) equation was developed by Carter et al., (2016) to supplement the SOCCOM float pH_T measurements. The only mandatory input for the LIAR equation is salinity, however, regressions containing more prediction variables reduces the uncertainty of the resulting TA estimate. The other predictor variables are outlined in Eq. 27:

$$A_T = \alpha_0 + \alpha_S S + \alpha_\theta \theta + \alpha_{AOU} AOU + \alpha_N N + \alpha_{Si} Si \qquad (27)$$

where α represents the estimated regression coefficients, S is salinity, θ is potential temperature in °C, N is the nitrate concentration in μmol/kg, AOU is the apparent oxygen utilization in μmol/kg and Si is the total dissolved silicate concentration in μmol/kg.

The use of the LIAR equation is available as a MATLAB R2014b script, compatible with earlier versions dating back to 2012. The script interpolates regression coefficients to the location by Delaunay Triangulation 3D linear interpolation routines and inputs the resulting regression coefficients directly into Eq. 27 to estimate TA. Further requirements and

assessment of uncertainties associated with each regression combination are discussed in Carter et al., (2016).

3.3.3 pH_T calculation from the raw output of the sensor

The Nernstian response of the internal cell for the pH_T sensor is calculated as:

$$pH_{int} = \frac{V_{FET|INT} - k_0 - k_2 T}{S_N} \quad (28)$$

$$S_N = \frac{R\,T \ln(10)}{F} \quad (29)$$

where $V_{FET|INT}$ is the measured potential for the internal reference electrode in mV, R is the universal gas constant in J/(K mol), T is the temperature in K, S_N is the Nernst potential, F is the Faraday constant in C/mol, k_0 is the cell standard potential offset and k_2 is the temperature slope provided as part of the instrument calibration.

The Nernstian response of the external cell of the pH_T sensor is affected by the activity of chloride in the seawater, which is calculated from the salinity of the sample solution:

$$pH_{ext} = \frac{V_{FET|EXT} - k_0 - k_2 T}{S_N} + \log(Cl_T) + 2\log(\gamma_{HCl}) - \log\left(1 + \frac{S_T}{K_S}\right) \quad (30)$$

where $V_{FET|EXT}$ is the measured potential for the external reference electrode in mV, k_0 is the cell standard potential offset, k_2 is the temperature slope provided as part of the instrument calibration, T is the temperature in K, Cl_T is the total chloride concentration, γ_{HCl} is the constant for HCl activity, S_T is the total sulphate concentration of seawater and K_S is the acid dissociation constant of HSO_4^-.

The chloride activity of the sample solution is calculated from several equations, the ionic strength of the solution, the total chloride concentration, the acid dissociation constant for HSO_4^- and the total sulfate activity in seawater are calculated according to Dickson et al., (2007).

The ionic strength, total chloride concentration and total sulphate concentration of seawater are based on the salinity of the seawater, and is calculated according to the equations:

$$I = \frac{19.924\,S}{1000 - 1.005\,S} \tag{31}$$

$$Cl_T = \frac{0.99889}{35.453} \times \frac{S}{1.80655} \tag{32}$$

$$S_T = \frac{0.1400}{96.062} \times \frac{S}{1.80655} \tag{33}$$

where I is the ionic strength of seawater, Cl_T is the total chloride concentration of seawater, S_T is the total sulphate concentration of seawater and S is the measured salinity of seawater in PSU.

The logarithm of HCl activity coefficient is calculated according to the equation by Khoo et al. (1977):

$$\log(\gamma_{HCl}) = \frac{-A_{DH}\sqrt{I}}{1 + 1.394\sqrt{I}} + (0.08885 - 0.000111\,t)\,I \tag{34}$$

where A_{DH} is the Debye-Huckel constant for HCl activity, I is the ionic strength and t is the temperature in °C. The Debye-Huckel constant for HCl activity is calculated from the relationship with temperature according to Khoo et al., (1977):

$$A_{DH} = 0.00000343\,t^2 + 0.00067524\,t + 0.49172143 \tag{35}$$

where t is temperature in °C.

Acid dissociation constant of HSO_4^-

$$K_S = (1 - 0.001005\,S)\,e^x$$

$$\begin{aligned} x = {} & \frac{-4276.1}{T} + 141.328 - 23.093\ln(T) \\ & + \left(\frac{-13856}{T} + 324.57 - 47.986\ln(T)\right)\sqrt{I} \\ & + \left(\frac{35474}{T} - 771.54 + 114.723\ln(\mathrm{T})\right)I - \left(\frac{2698}{T}\right)I^{1.5} \\ & + \left(\frac{1776}{T}\right)I^2 \end{aligned} \tag{36}$$

where T is the measured temperature in K and I is the ionic strength of seawater.

3.3.4 Carbonate variables in seawater – CO2calc parameters

Measured pH_T obtained from the SOCCOM float array is combined with estimated values of TA from the LIAR equation to compute the carbonate system via CO2Calc (Robbins et al., 2010). *In situ* pH was input on the total pH scale, with carbonate constants based on Lueker et al. (2000), borate dissociation coefficients on Dickson (1990), total boron from Lee et al. (2010) and the HF dissociation constant from Perez and Fraga (1987). The resulting outputs are included in the data product available in real time on the SOCCOM website: https://www.mbari.org/science/upper-ocean-systems/chemical-sensor-group/soccom-float-visualization.

3.4 Data processing

3.4.1 pH_T calibration by percentage error correction

The raw pH_T data (Figure 3.4) obtained from the first WG clearly showed an error in calibration of the pH_T sensor prior to the deployment of the WG. pH_T measurements from October – November 2013 were too high to reflect an accurate representation of the carbonate system within valid parameters. Therefore, raw pH_T measurements were back calibrated by a percentage error method (Equation 37) based on monthly climatology of pCO_2, the monthly mean of pCO_2 measured by the WG, and discrete bottle measurements of TA obtained from the deployment of the second WG, to determine the expected pH_T at the WG location (45 °S, 8.5 °E).

$$\% \text{ Error} = \frac{\text{Measured } pH_T - \text{Calculated } pH_T}{\text{Calculated } pH_T} \times 100 \qquad (37)$$

Proper calibration of the sensor prior to the deployment of the WG and at the recovery of the WG are essential to calibrate the pH_T sensor, determine its precision and to account for sensor drift over time. The absence of valid pH_T data between November and December is due to the retrieval of the first WG and the deployment of the second WG (Figure 3.4). The correction over the December period was minimal, indicating that the initial calibration on the second WG was carried out correctly. Further validation and considerations of using this approach are outlined in Appendix D, Section D.1.

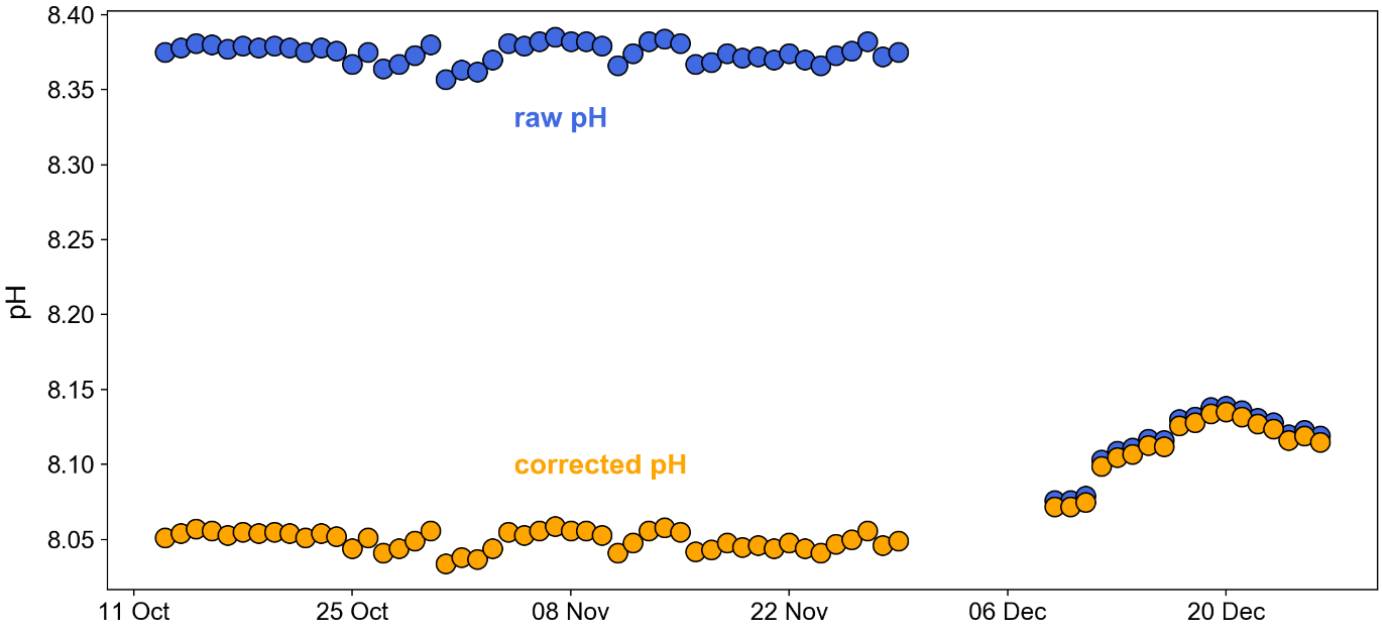

Figure 3.4: Raw pH data output from the Wave Glider compared to the percentage error corrected values between October and December 2013

3.4.2 SOCCOM float data processing

SOCCOM float data was obtained from (https://www.mbari.org/science/upper-ocean-systems/chemical-sensor-group/soccom-float-visualization/) for floats 9096, 9620 and 9313 in the region of interest (longitude 0 – 45 °E and latitude 30 – 60 °S). The data obtained was further constrained by valid *in situ* pH_T readings in the range of 7 – 8.2, at an ocean surface depth of 10 m, and contained measurements over the winter season from 2015 – 2017 collectively.

The float-measured salinity and temperature were used to compute TA from the Lee et al., (2006) formula for comparison with TA derived from the LIAR equation (Carter et al., 2016). The LIAR_TA and LIAR_pCO_2 values, provided in the data product, were also used for comparison against ship measurements of TA, DIC and computed pCO_2 thereof.

pH_T sensor calibration adjustment

The float-measured pH_T is calibrated according to an empirical algorithm outlined by Williams et al., (2016):

Measured pH_T is obtained from discrete bottle samples and converted to *in situ* pH using CTD, temperature and pressure. An estimate for pH_T for the same bottle samples is calculated from the MLR algorithm using temperature, salinity, pressure, oxygen and the *in situ* pH at a depth between 1000 – 2000 m. The MLR algorithm is applied to the float-measured pH_T to yield an *in situ* pH-MLR estimate. The reference potential for the Deep-Sea DuraFET pH sensor is adjusted to match the *in situ* pH sensor pH at ~1500 m, and the *in situ* pH-MLR estimate using a one-time offset correction or a time-dependent drift correction. The new calibration is applied to the entire float profile.

3.4.3 Salinity normalisation

To assess the variation in TA in the surface ocean, TA measurements were salinity-normalised to identify the biological processes affecting TA without the influence of salinity and differing water masses. This correction process was applied to all measured TA datasets.

Measured TA values were processed using the Friis et al., (2003) correction formula and normalised to a constant salinity reference value of 34.2 psu (Equation 38), which was the average salinity value for the observational dataset. Measured TA values are plotted against salinity to yield a straight line equation to find the value of TA at the x-intercept i.e. at zero salinity (Figure 3.5 a), which is then subtracted from the measured TA before the correction is applied, and added back after the correction process (Figure 3.5 b):

$$A_T{}^{eS} = \frac{A_T{}^{meas} - A_T{}^{S=0}}{S^{meas}} \times S^{ref} + A_T{}^{S=0} \qquad (38)$$

where $\mathbf{A_T^{eS}}$ is the salinity-normalised total alkalinity in µmol/kg, $\mathbf{A_T^{meas}}$ is the measured total alkalinity in µmol/kg, $\mathbf{A_T^{S=0}}$ is the calculated total alkalinity at zero salinity in µmol/kg, $\mathbf{S^{meas}}$ is the measured salinity in psu and $\mathbf{S^{ref}}$ is the selected reference salinity in psu (Friis et al., 2003).

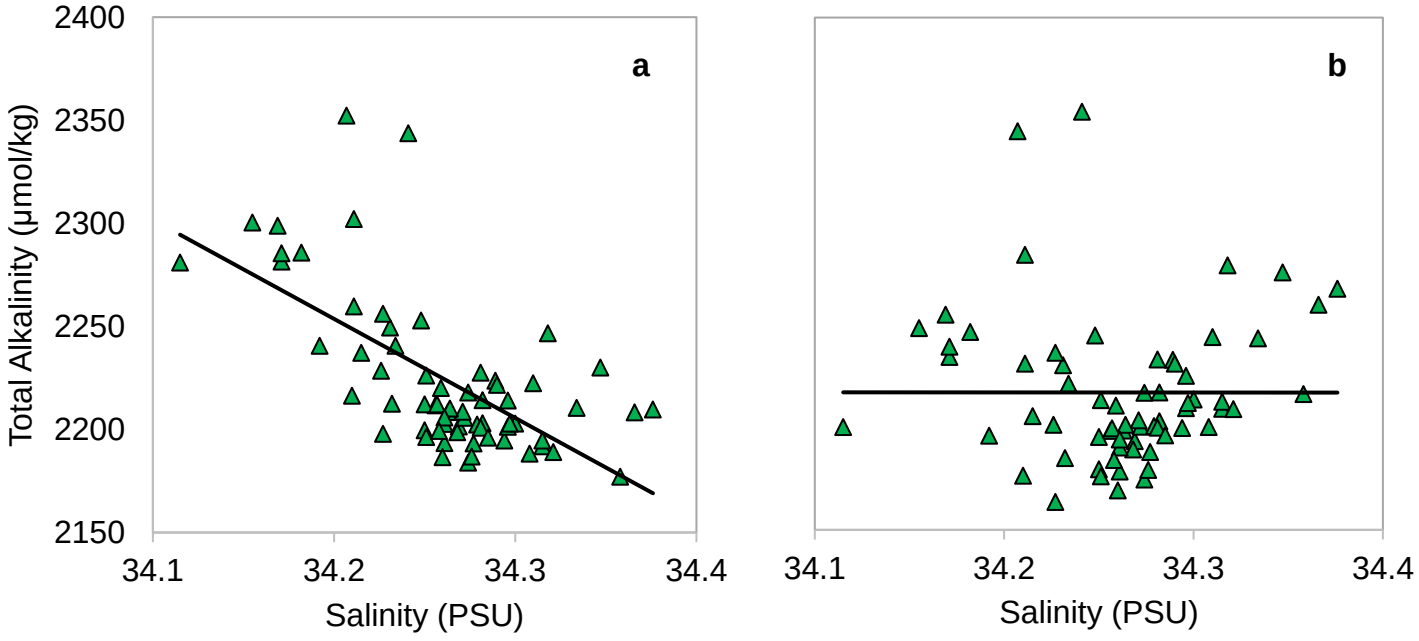

Figure 3.5: (a) Total alkalinity dataset for the Wave Glider and (b) salinity-normalised total alkalinity dataset

4 Results

4.1 Oceanographic context

The results are based on the analysis of three data sets which coincide in space, but differ in time and the platform of measurement. Figure 4.1 depicts the location of each observation platform in relation to each other: the WG is situated at 43 °S, 8.5 °E in the SAZ from spring to summer 2013; the WC transects run parallel to the meridian from 2015-2017 during austral winter; and the SOCCOM floats run parallel to the ACC, situated in the STZ, SAZ, PFZ and the MIZ, from summer 2014 – winter 2017.

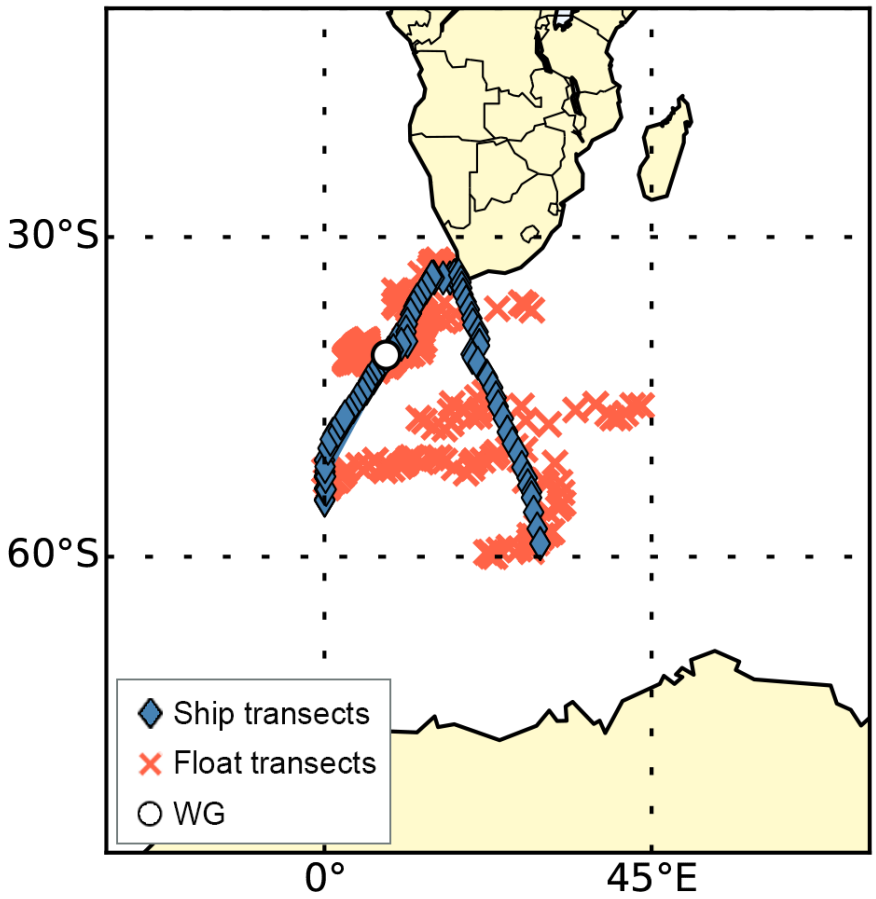

Figure 4.1: Sampling location for each observation platform relative to each other, the Wave Glider is shown in white, the Winter Cruise transects are shown in blue, and the SOCCOM float transects are shown in orange**.**

Figure 4.2 shows the temperature/salinity (TS) plots for each observation platform in the surface ocean. Figure 4.2 (a) and (b) show data from the WC transects and the WG, and Figure 4.2 (c) shows the data from float 9313, 9260 and 9096 located in the SAZ, PFZ and MIZ,

respectively. The WC TS plot shows a meridional progression with higher temperatures coupled to a higher salinity in the north, and the lower temperatures coupled to a slightly fresher surface ocean at the MIZ. The WG TS plot shows minor changes in salinity over time, with a slight freshening coupled to warmer temperatures in the SAZ. The float TS plot indicates that Float 9313 shows higher salinity, lower density waters consistent with warmer temperatures in the STZ/SAZ, with denser, slightly fresher waters coupled with cooler temperatures. Float 9260 located in the PFZ shows little variation in salinity over a narrow range in temperature, whereas float 9096 in the MIZ shows larger variations in salinity over a narrow temperature range, characteristic of the changing seasonal environment linked to brine rejection during the formation of sea-ice.

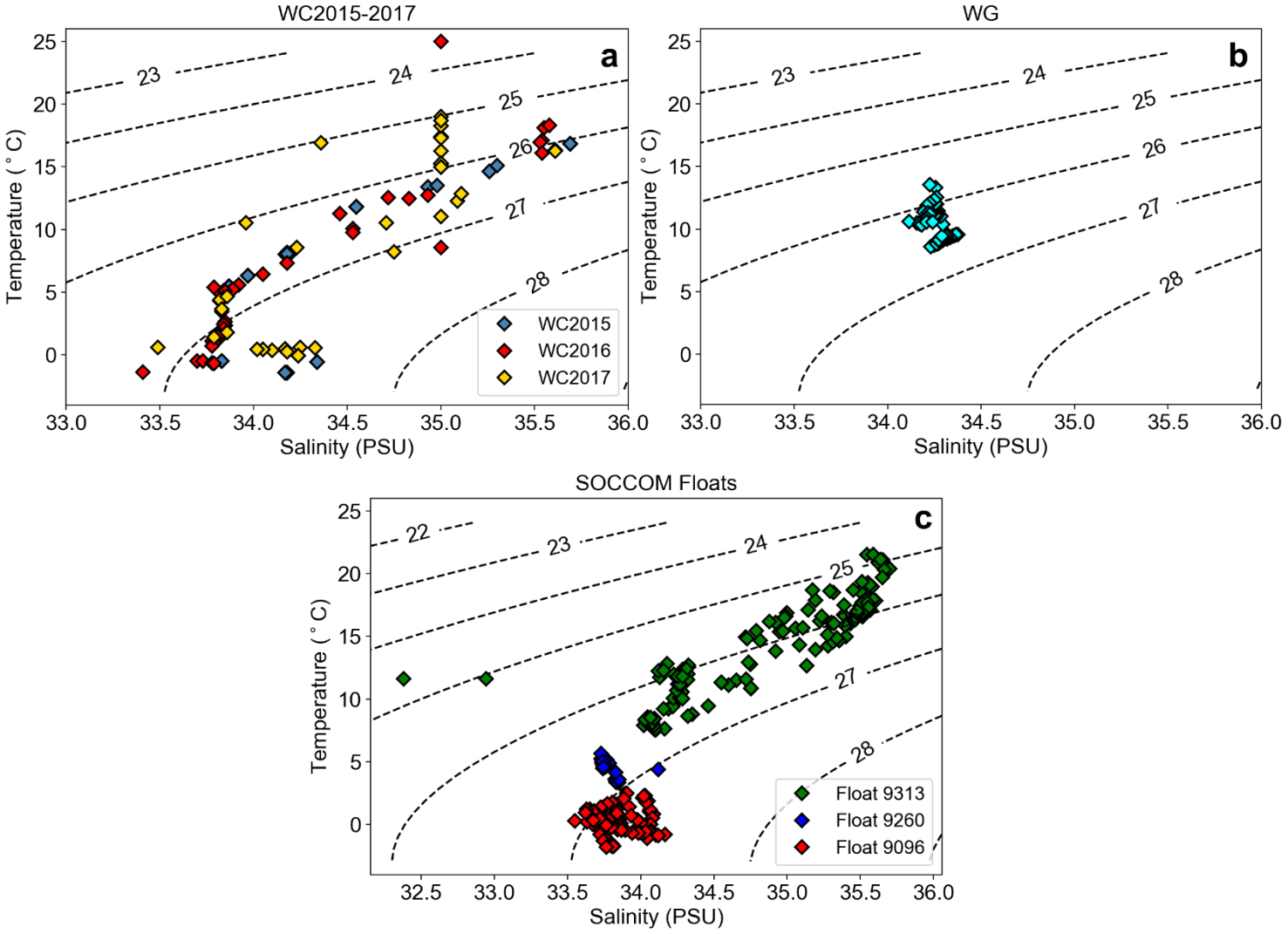

Figure 4.2: Temperature/salinity diagrams for the (a) WC transects from 2015 – 2017, (b) the WG, and (c) the SOCCOM floats from summer 2014 – winter 2017.

4.2 Wave Glider observations

Measurements of pCO_2, pH_T, temperature and salinity were made by the WG from October to December 2013 at 43 °S and 8.5 °E. Figure 4.3 shows the WG in location during spring-summer bloom period, when satellite imagery shows an elevated mean chlorophyll-*a* concentration (~2.0 mg/m^3) associated with a mesoscale frontal feature in December 2013.

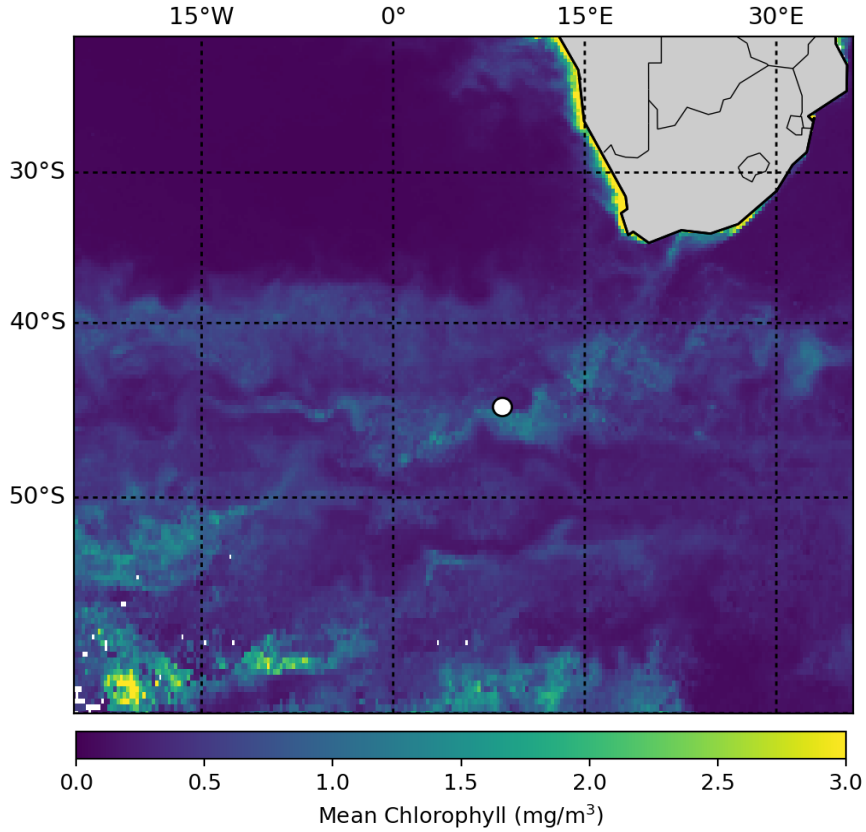

Figure 4.3: Monthly mean chlorophyll-*a* over the sub-Antarctic zone from December 2013 - January 2014. The position of the Wave Glider is denoted in white at 43 °S and 8.5 °E.

The physical (T, S) and biogeochemical (pH_T, pCO_2) observations from the WG and satellite data (Chl-*a*) are depicted in Figures 4.4 - 4.6. Together, the physical and biogeochemical data sets show that the seasonal observations are characterised by two distinct periods: the spring period (Oct – Nov) marked by variations of T, S and Chl-*a* within a narrow range, and the spring-summer period (Dec – Jan) characterised by rapid warming, weak freshening and the spring-summer bloom (Figures 4.4 – 4.5). Hereafter, these distinctions will be referred to as the pre-bloom period and the bloom period, respectively. The absence of measured data between November and December is due to the retrieval of the first WG and the deployment of the second WG.

The daily mean values for salinity and temperature are shown in Figure 4.4. The freshening of the surface ocean from the pre-bloom period into the bloom period indicates added precipitation to the surface ocean in the region. The added precipitation can be linked to storm activity, or a freshening of the SAMW at the surface in the SAZ due to the melting of sea ice in summer (Talley, 2011). The rise in temperature from the pre-bloom to the bloom period coincides with the increase in chlorophyll-*a* concentrations (Figure 4.5) as the summer season in the SAZ ensues. Coinciding with increasing temperatures and a weak freshening of the surface waters, we see a decrease in surface pCO_2 from 379.3 ± 7.453 µatm to 332.2 ± 15.34 µatm, and an increase in pH_T from 8.050 ± 0.006 to 8.112 ± 0.020 (Figure 4.6). The daily mean increase in pH_T and corresponding decrease in pCO_2 is characteristic of the increased biological uptake of CO_2 during the bloom period as CO_2 is utilised during photosynthesis, which is supported by the increasing chlorophyll-*a* concentrations (Figure 4.5). The monthly averaged measurements from the WG are summarised in Table 4.1.

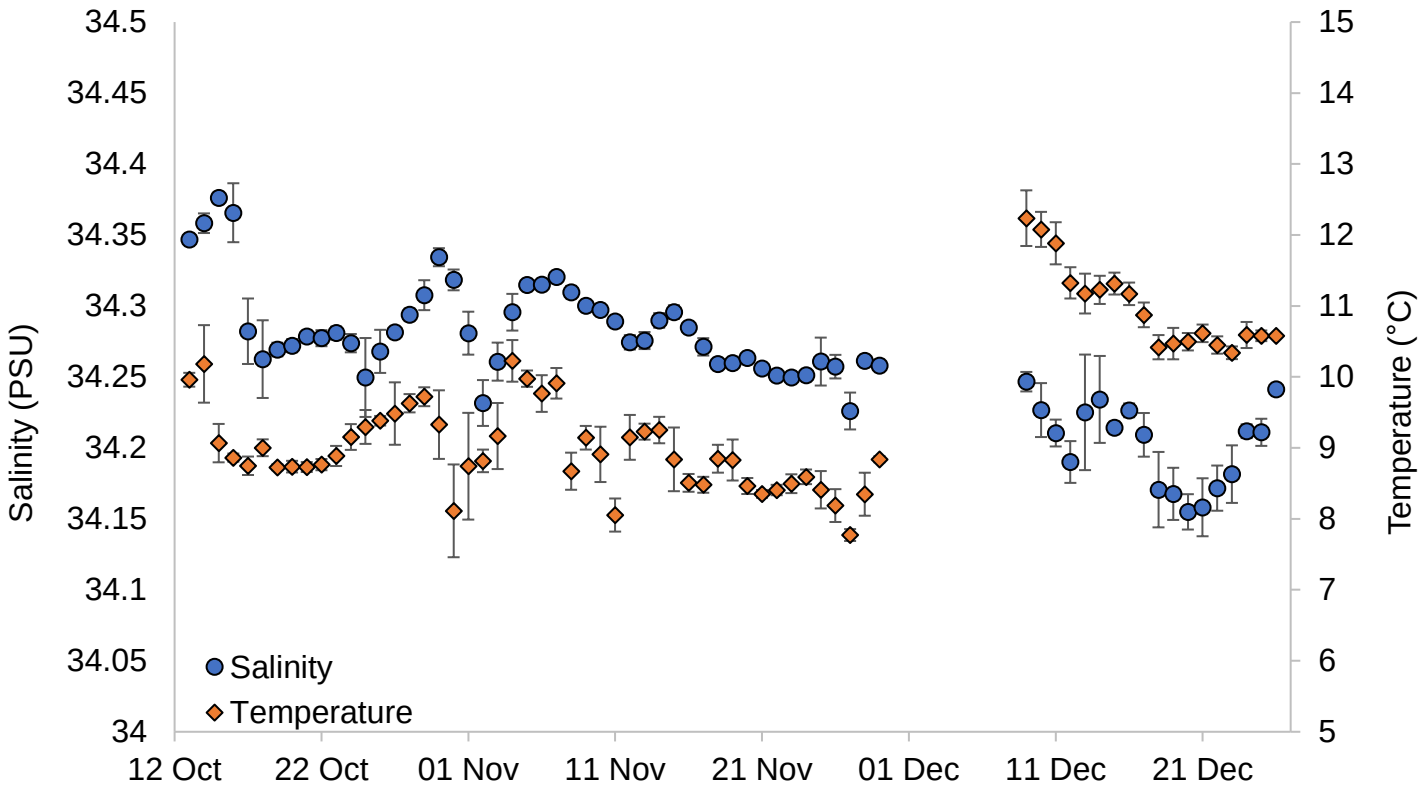

Figure 4.4: Daily mean salinity and temperature time series for the WG from Oct – Dec 2013. The missing data between Nov – Dec is a result of the retrieval of Glider 1 and the deployment of Glider 2.

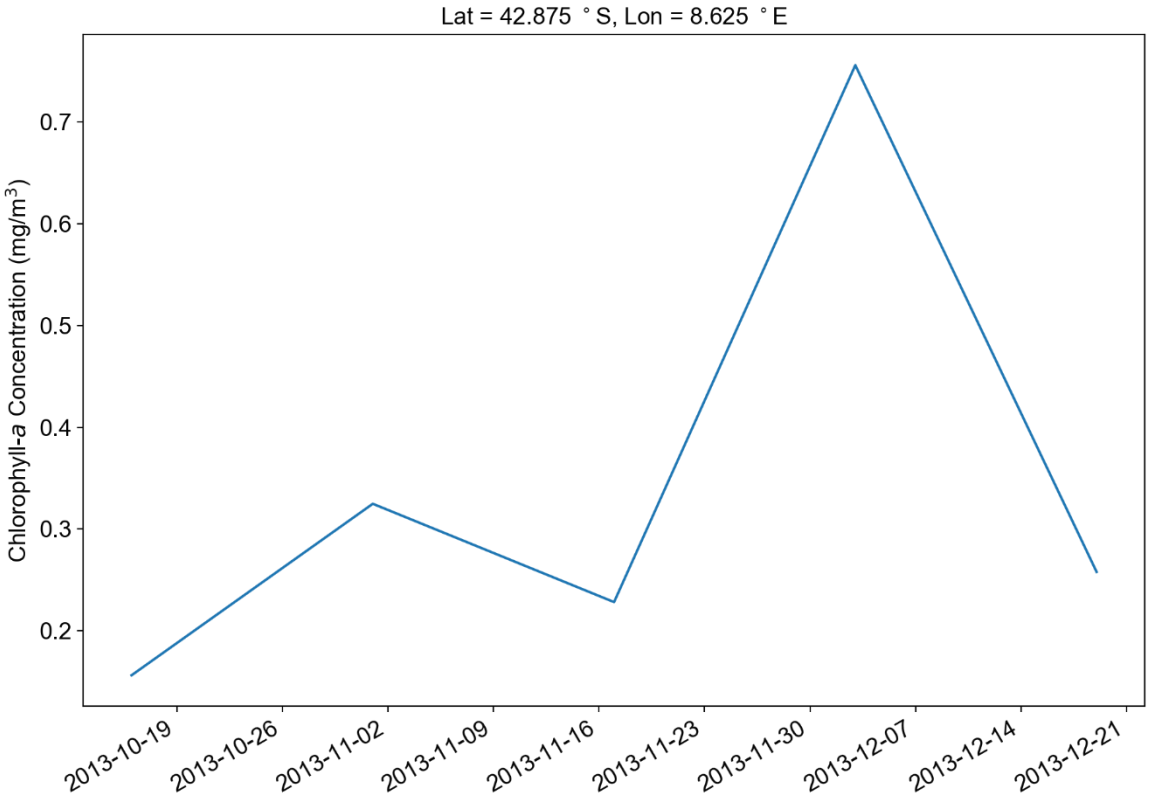

Figure 4.5: 16 day composite of chlorophyll-*a* concentrations in the region of the WG from Oct 2013 – Dec 2014 obtained from satellite observations (GLOB colour)

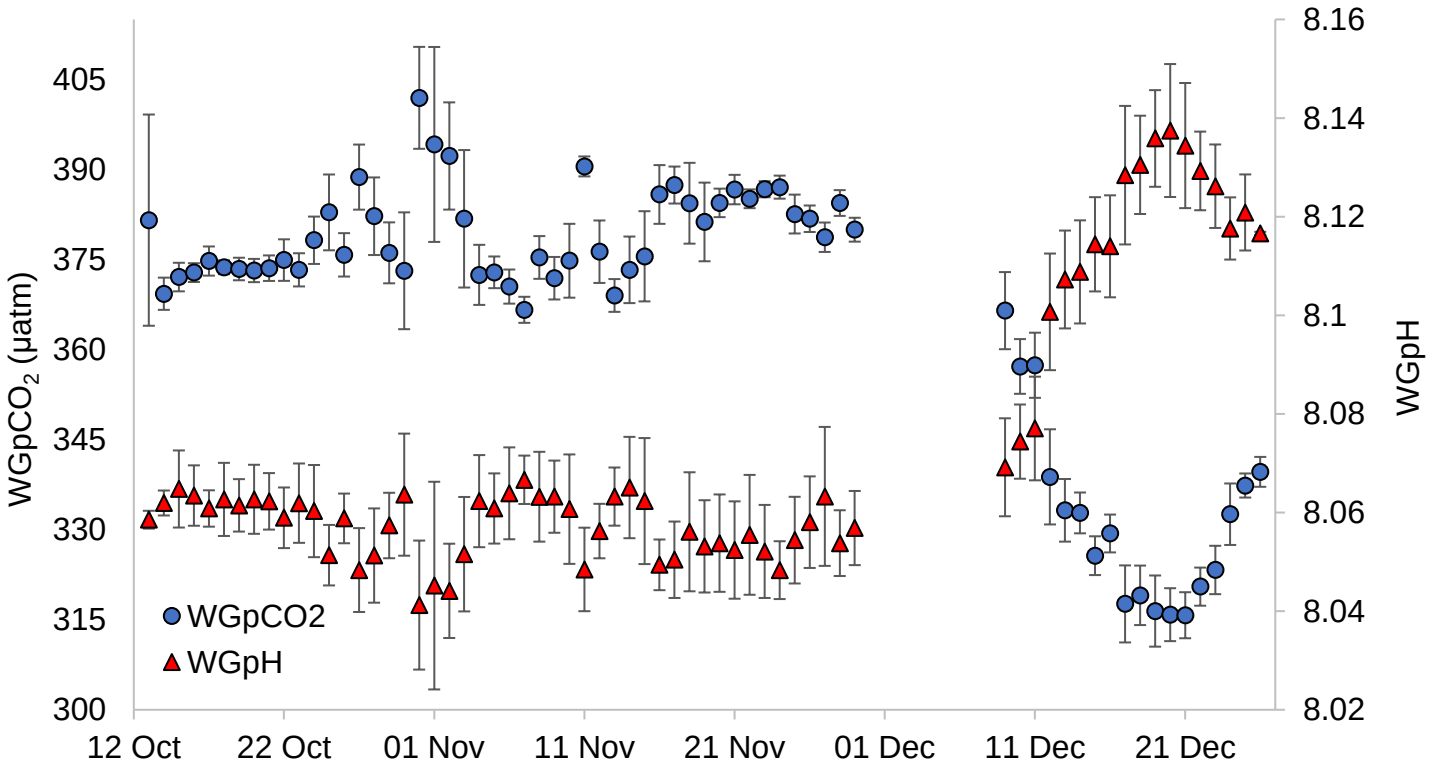

Figure 4.6: Daily average pH and daily average pCO_2 from Oct - Dec 2013 obtained from the WG. The missing data between Nov – Dec is a result of the retrieval of Glider 1 and the deployment of Glider 2.

Table 4.1: Monthly average pH_T, pCO_2 Temperature, and Salinity from the Wave Glider for Oct – Dec 2013.

	pH_T	**pCO_2 (µatm)**	**Salinity (PSU)**	**Temperature (°C)**
October	8.051 ± 0.006	377.4 ± 7.567	34.300 ± 0.03843	9.14 ± 0.25
November	8.049 ± 0.006	380.5 ± 7.258	34.275 ± 0.02485	10.4 ± 1.40
***Pre-bloom**	8.050 ± 0.006	379.3 ± 7.453	34.285 ± 0.03301	9.92 ± 1.26
December (Bloom)	8.112 ± 0.020	332.2 ± 15.34	34.201 ± 0.03468	11.0 ± 0.61
Pre-bloom compared to Bloom				
Difference between averages	0.062	-47.1	-0.084	1.08
****Significant difference**	✓	✓	✓	✓
Average difference between $WGpCO_2$ and $LEEpCO_2$				
***Pre-bloom**	13.56 µatm			
Bloom	4.978 µatm			

*The pre-bloom period is an average of measurements from October – November 2013.

**Significant difference is statistically defined as a measurable difference between the pre-bloom period and the bloom period for the respective measurements, with a p-value < 0.05.

Total alkalinity

Globally, TA is often derived from T-S parameterizations (Lee et al., 2006, Carter et al., 2014), and used along with measurements of pH_T to compute pCO_2. The WG dataset utilized for this study offered an opportunity to examine these parameterizations against *in situ* observations. The observed pH_T, T and S were used to calculate pCO_2 from the Lee et al., 2006 relationship ($LEEpCO_2$), as is typically done in many studies e.g. the SOCCOM floats. This was then compared to *in situ* pCO_2 observations ($WGpCO_2$; Figure 4.7).

There was a significant difference observed between $LEEpCO_2$ and $WGpCO_2$ from the pre-bloom period to the bloom period in both datasets (Figure 4.7). However, there was an average difference between the observed ($WGpCO_2$) and calculated pCO_2 ($LEEpCO_2$) of 13.56 µatm in the pre-bloom period, and 4.978 µatm in the bloom period (Table 4.1). The largest difference between $LEEpCO_2$ and $WGpCO_2$ occurred during the pre-bloom period (19.26 µatm), followed by little to no difference during the bloom period (Figure 4.7), although it is acknowledged that this large discrepancy may in part be an artefact of the pH percentage error correction method.

To investigate the drivers of the differences between the $LEEpCO_2$ and $WGpCO_2$, WG measurements of pH_T and pCO_2 were used to calculate TA (WGTA) and compared to LeeTA (Figure 4.8). LeeTA had a nearly constant value from Oct – Dec 2013, with a mean of 2281 ± 4.242 µmol/kg and a range of 2273 – 2288 µmol/kg. In contrast, WGTA had a mean of 2206 ± 13.86 µmol/kg during the pre-bloom period, which increased to a mean of 2271 ± 40.29 µmol/kg following the bloom period. The increase in WGTA observed during December coincided with Chlorophyll-*a* maxima (Figure 4.5), the decrease in pCO_2 (Figure 4.6) and the increase in pH_T (Figure 4.6).

The salinity normalised WGTA is also shown in Figure 4.8 to account for possible contributions from changes in water physical properties in the surface ocean. However, a significant increase in normalised WGTA was still seen throughout the bloom period.

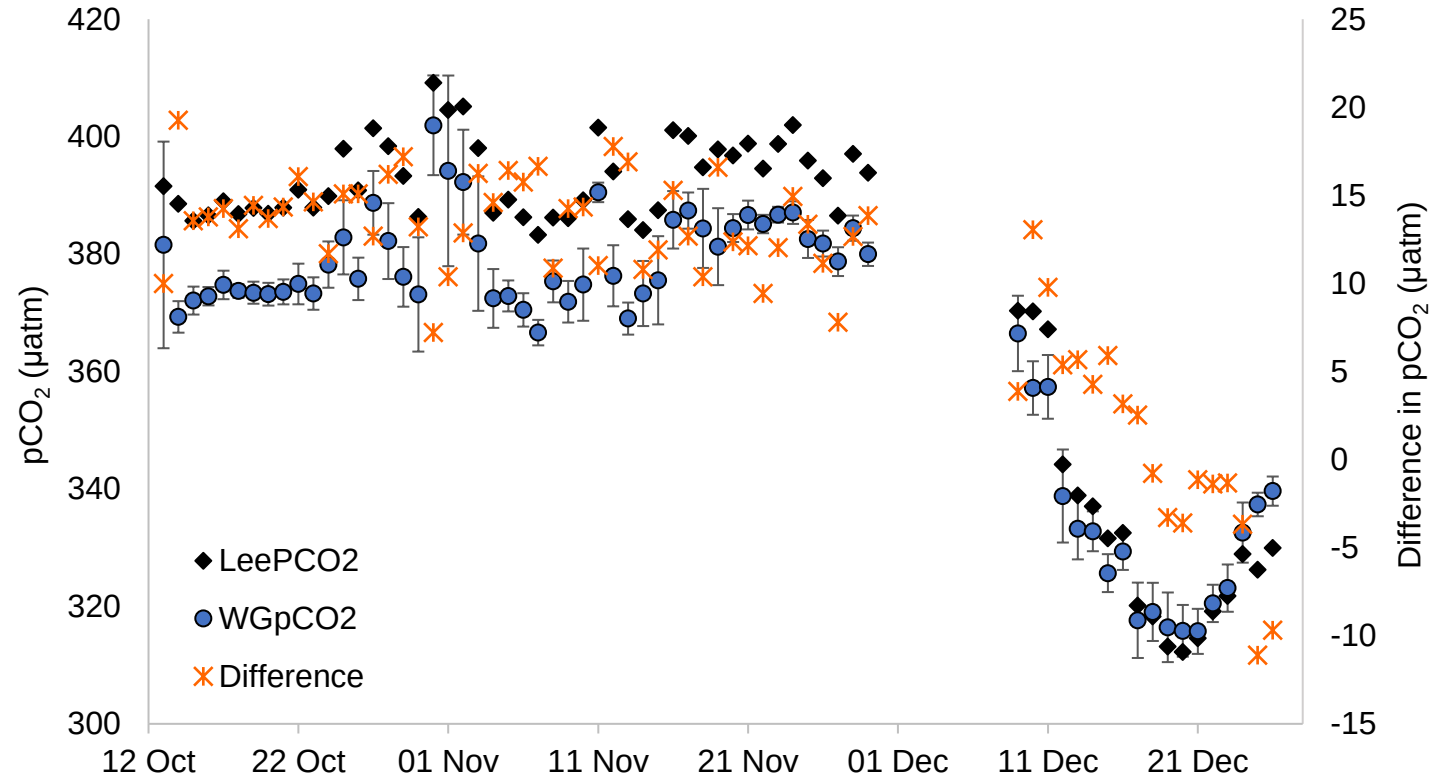

Figure 4.7: Time series for WG measured pCO_2 and pCO_2 calculated from LeeTA from Oct - Dec 2013

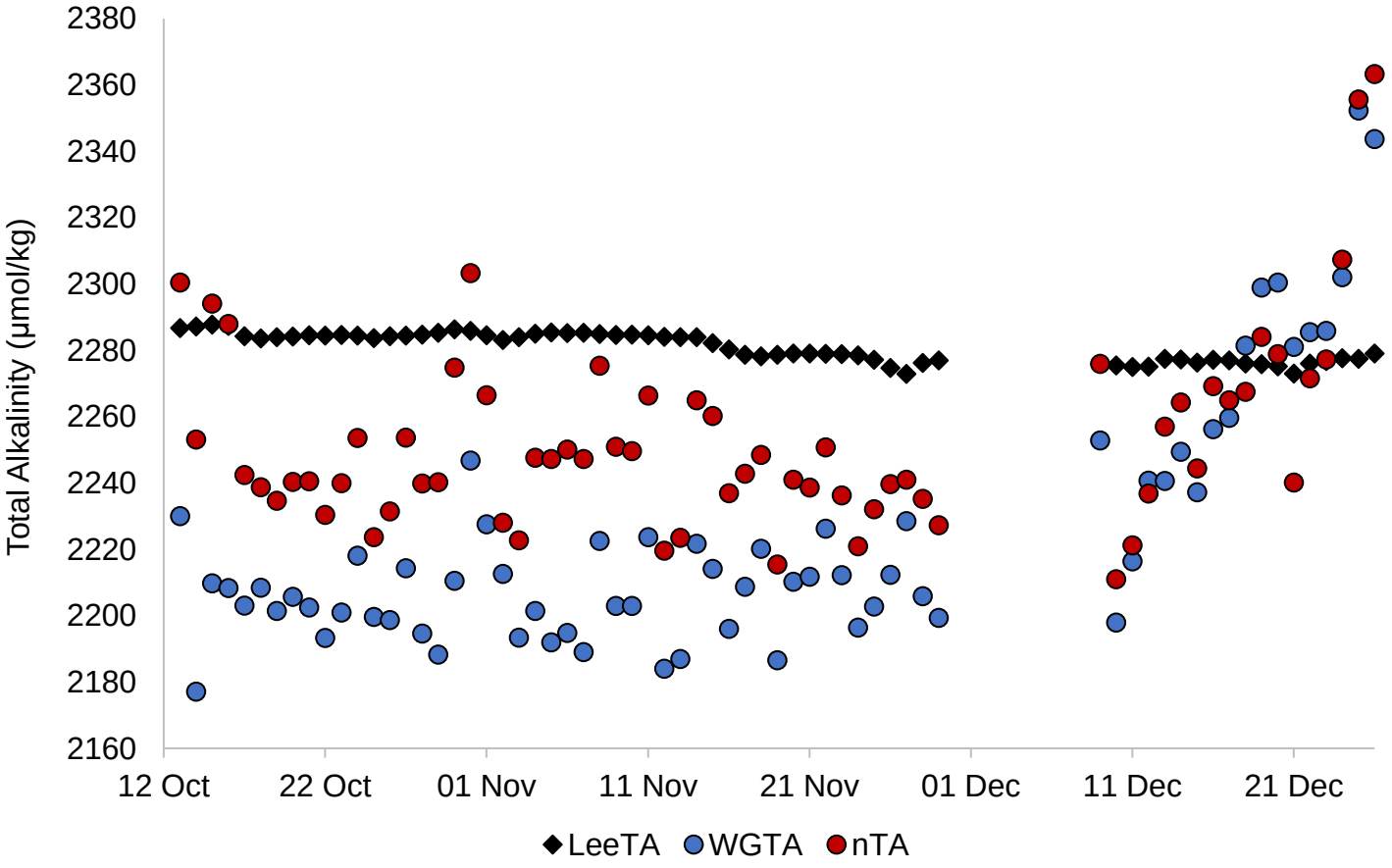

Figure 4.8: Total alkalinity derived from measurements on the WG, and salinity-normalised total alkalinity derived from the WG plotted against time, compared with total alkalinity derived from the Lee formula.

4.3 Ship-board observations during winter

Ship-board measurements for each winter cruise (WC) are categorized according to an estimate of the frontal zones from N to S: the subtropical zone (STZ: 30 – 40 °S), the sub-Antarctic zone (SAZ: 40 – 45 °S), the polar frontal zone (PFZ: 45 – 50 °S), the Antarctic zone, referred to here as the Polar Upwelling Zone (PUZ: 50 – 55°S) and the marginal ice zone (MIZ: 55 – 70 °S) along the Good Hope line.

As salinity and temperature are the key parameters used to calculate TA by the means of the Lee expression, we looked at how each of these parameters change across the respective transects. Salinity (Figure 4.9) and temperature (Figure 4.10) between WC2015, WC2016 and WC2017 are not significantly different across each transect. The STZ was characterised by saline and warm surface waters consistent with SASW with temperatures ~ 15 °C and a salinity range of 34.0 – 35.5 PSU (Emery, 2015). The SAZ had cooler and slightly fresher waters, as expected of SAMW with temperatures between 4 –10 °C, and a salinity of 33.9 – 34 PSU in the winter (Talley, 2011). Temperatures continued to decrease into the PFZ and further south to the MIZ, indicating the presence of AASW, with temperatures -1.9 – 1.0 °C, and a salinity range of 33.0 – 34.6 PSU (Talley, 2011, Emery, 2015). However, the surface ocean was observed to become more saline in the PUZ and salinity increased into the MIZ. Salinity and temperature data show a similar trend, with a freshening of the surface waters coinciding with a decrease in temperature across the transect from the STZ to the PFZ. The increase in salinity observed in PFZ and PUZ coincided with colder temperatures, thus we attributed the more saline waters to an excursion of brine from the formation of sea-ice in the winter, coupled with the upwelling of CDW. Considering the spatial difference between the Indian and Atlantic Ocean sectors, we observed that there was a significant difference (see Appendix C, Table C3 – C8 for p-values) in salinity between WC2015 and WC2016, and WC2015 and WC2017, respectively.

Owing to the sparse number of data points across the WC2015 transect that could be corroborated by CTD cast and nitrate data, the WC2015 dataset will not be included in the TA analysis. It is rather used to provide an insight into winter conditions along the Good Hope transect – for our purposes, salinity and temperature values were assigned accordingly by latitude from the nearest CTD station, and used in subsequent carbonate calculations. For example, in the STZ for WC2015 (Figure 4.9), salinity is set to 35.69 PSU, based on the closest CTD station at 35.15 °S. A value of 35 PSU was used in the carbonate calculations for

WC2017 across the STZ and SAZ due to a loss of 9 samples (Figure 4.10). This value was chosen as it falls within reported surface ocean measurements in these zones at a range of 34.5 – 35.5 PSU (Talley, 2011), as well as being similar to salinity values obtained during WC2015 and WC2016.

Nitrate concentrations (Figure 4.12) across each transect showed an increasing trend from the STZ to the PFZ, and are seen to plateau across the PUZ and MIZ. This is expected as the STZ is deplete of nutrients, characterised by low nitrate concentrations below 5 μM. The SAZ is a more biologically productive region as low nitrate concentrations are associated with nitrate consumption, nitrate concentrations increased throughout the SAZ (~ 20 μM). The plateau of nitrate at a maximum in the PUZ and MIZ are consistent with upwelling in the region, coupled with biological activity, as expected for a high-nutrient, low-chlorophyll (HNLC) region, limited by light and iron supply. Low light conditions coincided with the decrease in temperature across each transect. This trend is also observed between nitrate concentrations for WC2015 and WC2017. The highest nitrate concentrations were observed in the PUZ (> 25 μM), with slightly lower values observed in the MIZ (Figure 4.11).

For clarity, and because this study is not concerned with fine scale variability, underway pCO_2 averaged over a 4-hour period was observed for each transect. A minimum pCO_2 was observed in the STZ (~370 μatm), coinciding with more saline surface waters, warmer surface temperatures and low nitrate concentrations. pCO_2 increased along the transect moving south, SAZ (~ 400 μatm), PFZ (~ 420 μatm), with a pCO_2 maximum occurring in the the PUZ and MIZ (~440 μatm). This maximum coincides with the upwelling region, where cooler, CO_2 and nutrient-rich waters are brought to the surface from the deep ocean. The colder surface waters nearest the ice edge were expected to have a higher pCO_2 content as CO_2 is more readily absorbed by colder surface waters as per the solubility pump. There was little variation seen between the PUZ and MIZ in terms of pCO_2 content, likely due to the ice coverage which inhibits air-sea gas exchange of CO_2 in the MIZ. These results are summarised in Table 4.3.

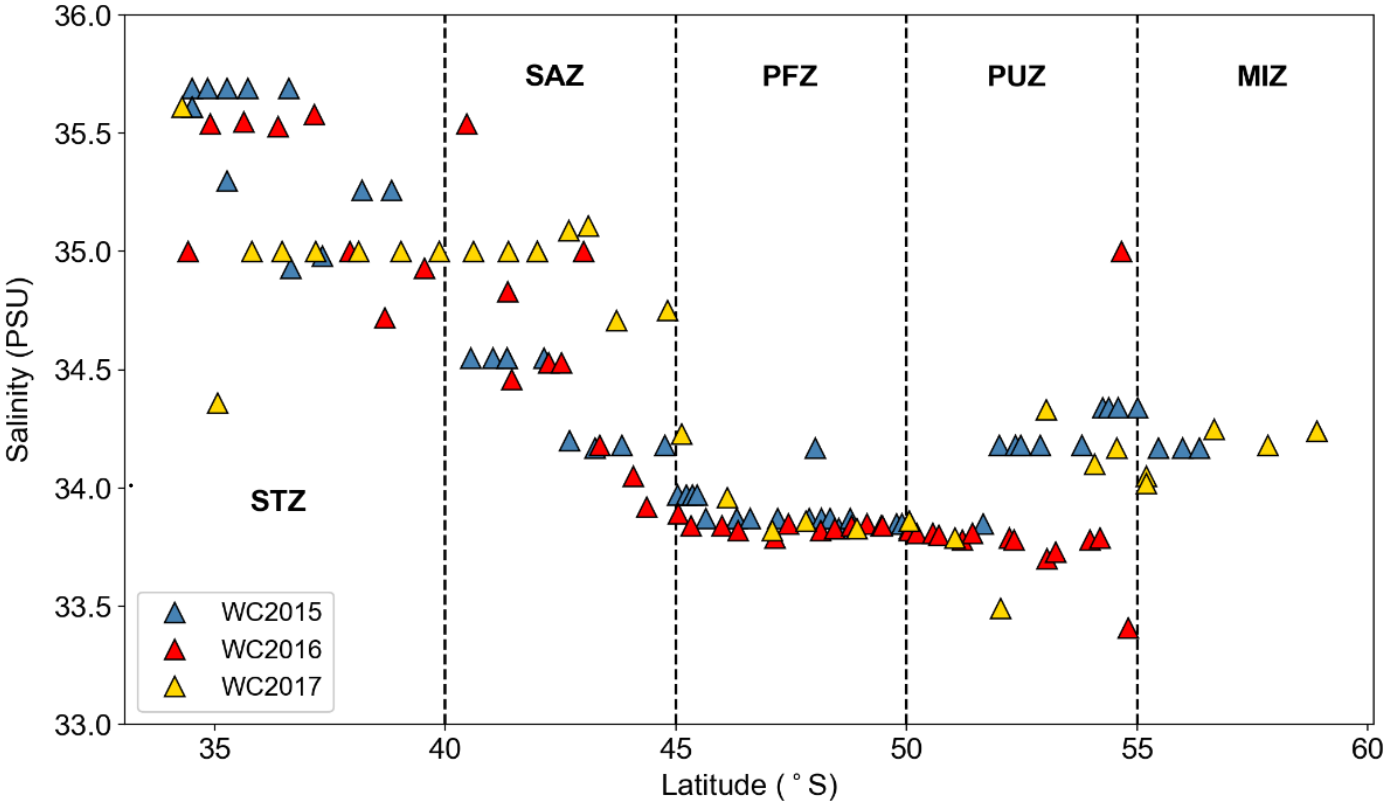

Figure 4.9: Salinity observations for WC2015 - WC2017 from the STZ to the MIZ

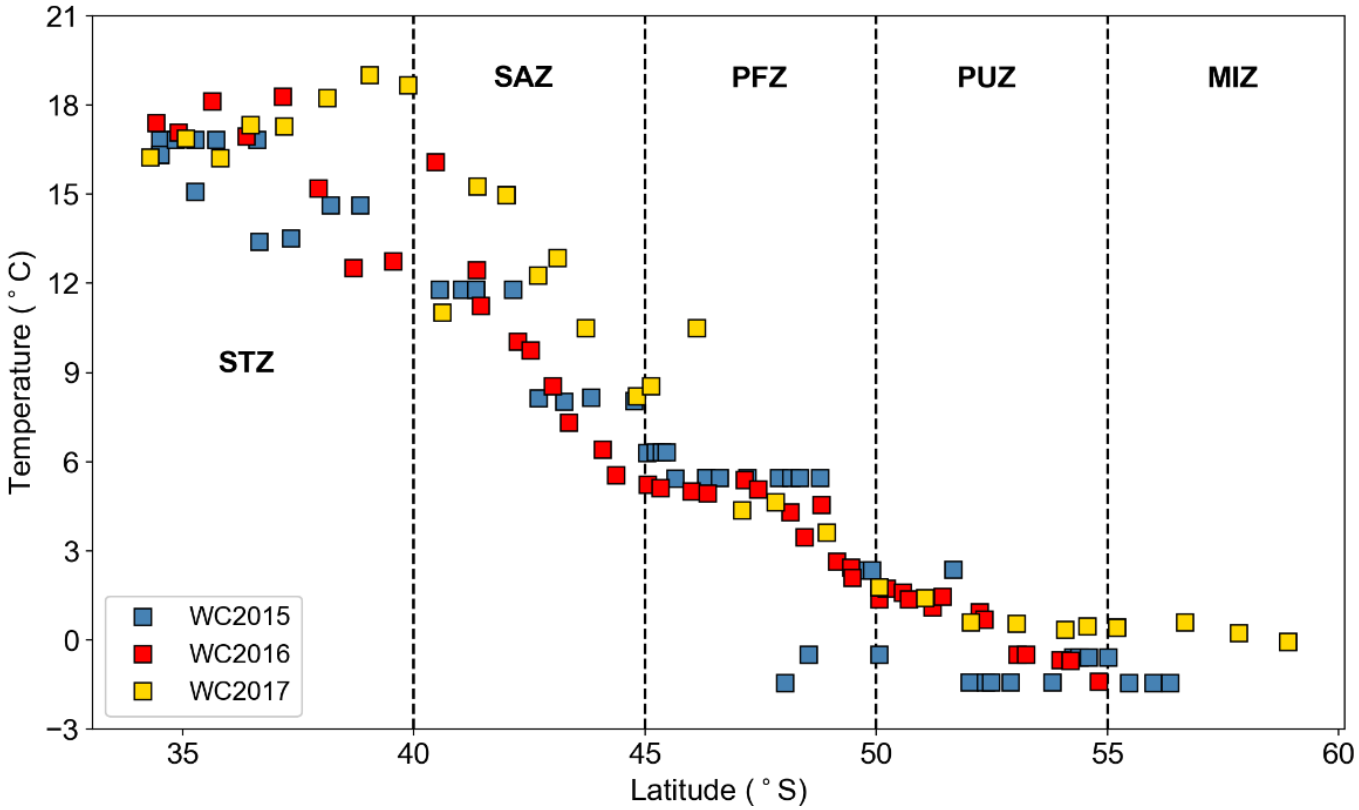

Figure 4.10: Temperature observations for WC2015 – WC2017 from the STZ to the MIZ

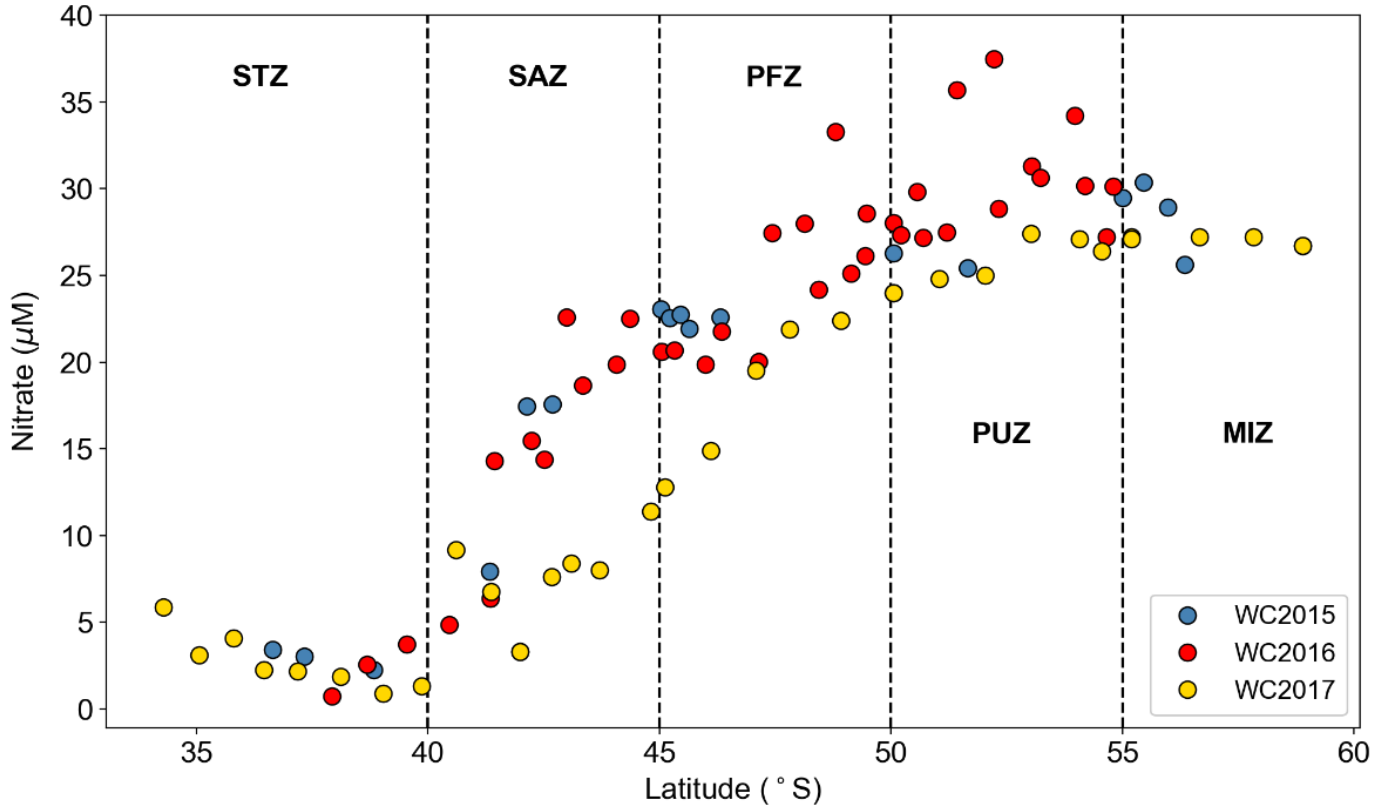

Figure 4.11: Nitrate distribution from the STZ to the MIZ for WC2015 – WC2017

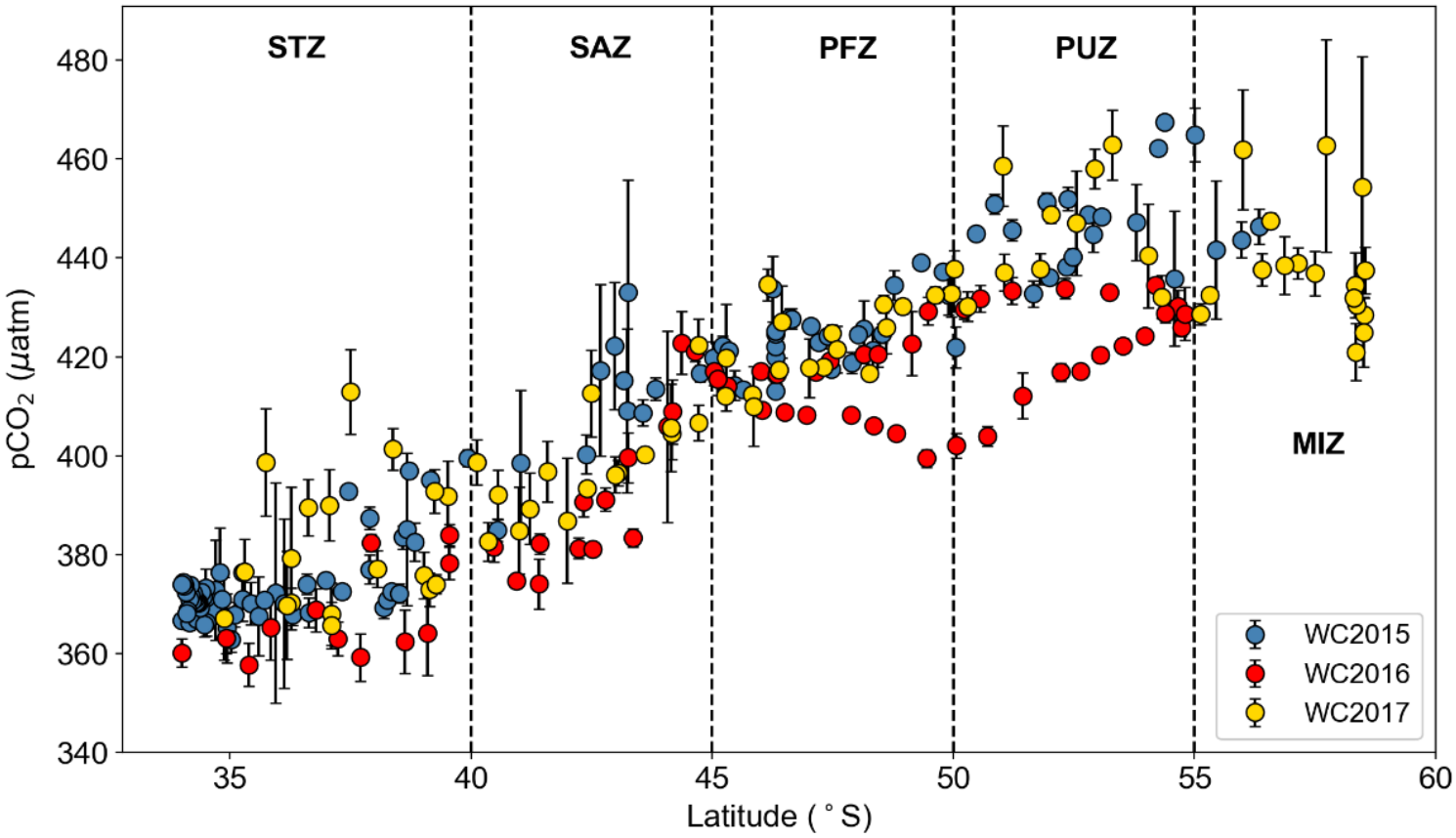

Figure 4.12: Underway pCO_2 measurements averaged over 4-hour intervals, along the each transect for WC2015 – WC2017

TA observations for WC2015 – WC2017 are illustrated in Figure 4.13. The STZ showed high concentrations of TA (2326 ± 19.74 μmol/kg) that decreased moving further south into the SAZ (2284 ± 18.98 μmol/kg) and the PFZ (2270 ± 10.09 μmol/kg). The PUZ and MIZ are characterised by an increase in TA (2292 ± 8.97 and 2307 μmol/kg respectively) closest to the ice edge (Figure 4.13, Table 4.2). Examining the Lee relationship against these TA observations, Figure 4.14 shows the corresponding LeeTA values for each measured TA observation (shown in Figure 4.13). The LeeTA estimates showed a similar trend to the TA observations in each zone, however, LeeTA and TA are significantly different in the PFZ and PUZ between WC2015 and WC2016, and in the STZ during WC2017 (See Table C6 in Appendix C). A closer analysis of TA will be discussed further in Chapter 5, Section 5.1.3.

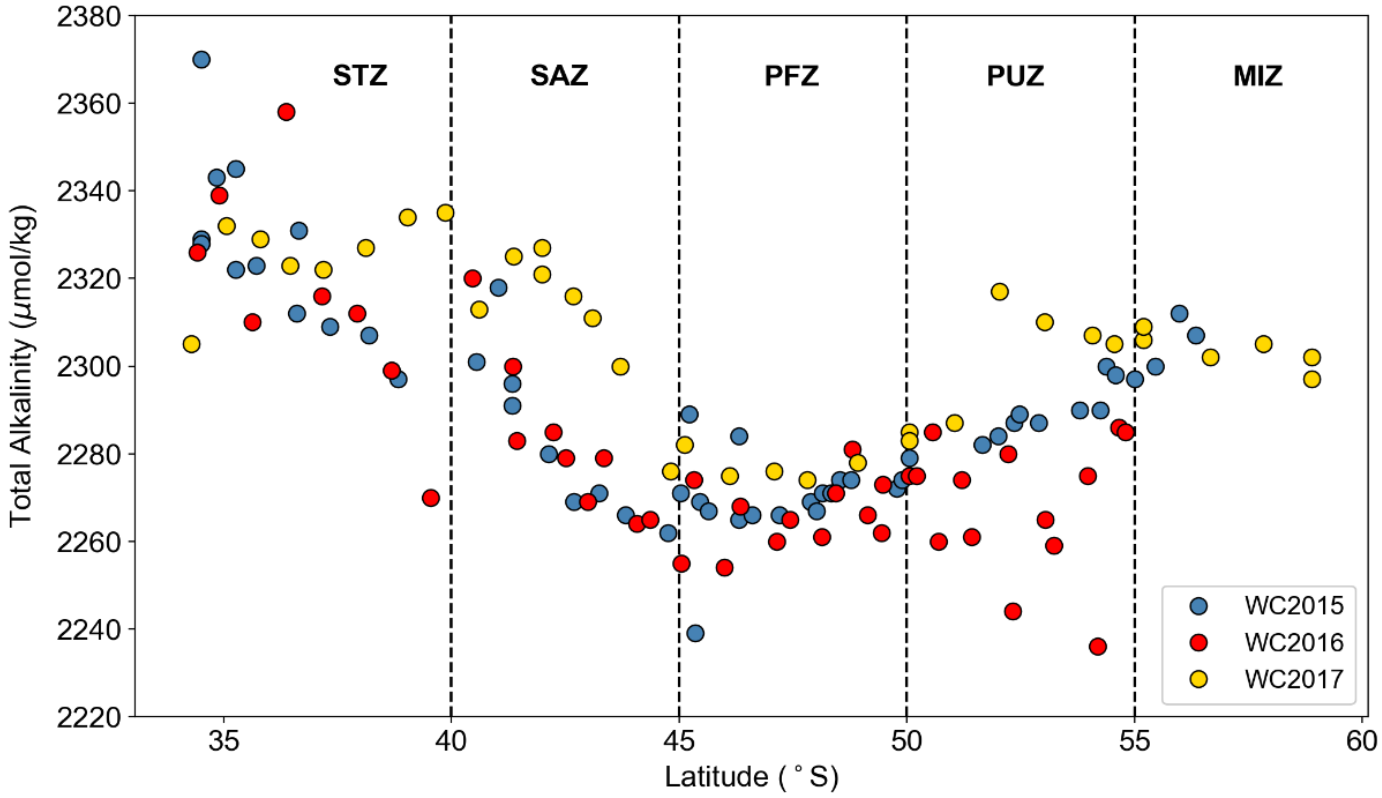

Figure 4.13: TA observations along transects spanning the subtropical zone (STZ) to the marginal ice zone (MIZ) during WC2015 – WC2017

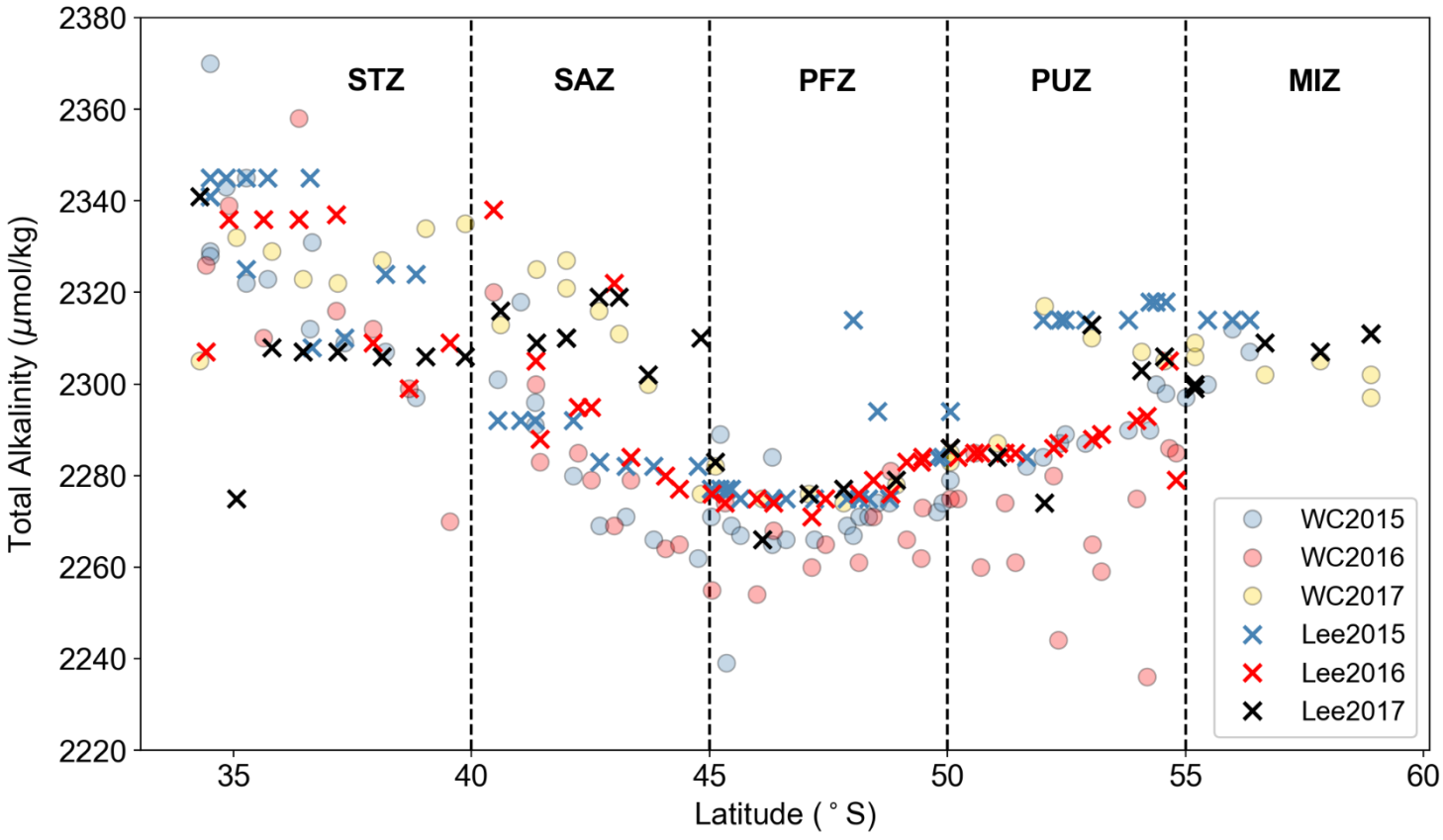

Figure 4.14: LeeTA estimates in comparison with the TA observations along transects spanning the subtropical zone (STZ) to the marginal ice zone (MIZ) during WC2015 – WC2017

Table 4.2: Mean observed values of salinity, temperature and nitrate concentrations for each winter cruise from the STZ to the MIZ. Note that WC2017 was conducted in a different geographical location from WC2015 and WC2016.

Cruise	Zone	Salinity (PSU)	Temperature (°C)	$[NO_3^-]$ (µM)
2015	STZ	35.45 ± 0.29	15.7 ± 1.35	2.89 ± 0.60
	SAZ	34.39 ± 0.19	10.2 ± 1.95	14.3 ± 5.53
	PFZ	33.91 ± 0.08	4.54 ± 2.38	22.6 ± 0.41
	PUZ	34.18 ± 0.17	-0.78 ± 1.04	28.1 ± 2.13
	MIZ	34.17	-1.43	25.6
2016	STZ	35.23 ± 0.35	16.1 ± 2.30	2.34 ± 1.50
	SAZ	34.56 ± 0.51	9.73 ± 3.27	15.5 ± 6.39
	PFZ	33.84 ± 0.023	4.20 ± 1.20	24.6 ± 4.23
	PUZ	33.84 ± 0.35	2.26 ± 6.63	30.4 ± 3.29
2017	STZ	35.00 ± 0.33	17.50 ± 1.06	2.69 ± 1.62
	SAZ	34.96 ± 0.15	12.52 ± 2.53	7.24 ± 2.80
	PFZ	33.94 ± 0.17	6.35 ± 3.02	18.3 ± 4.29
	PUZ	33.94 ± 0.28	1.00 ± 0.65	25.5 ± 1.41
	MIZ	34.16 ± 0.10	0.27 ± 0.28	27.0 ± 0.24

Table 4.3: Mean observations and estimates for TA and pCO_2 for each winter cruise from the STZ to the MIZ. Note that WC2017 was conducted in a different geographical location from WC2015 and WC2016.

Cruise	Zone	Measured TA (µmol/kg)	LeeTA (µmol/kg)	*Significant Difference	pCO_2 (µatm)
2015	STZ	2326 ± 19.74	2333 ± 14.16	✗	373 ± 7.66
	SAZ	2284 ± 18.98	2287 ± 5.181	✗	411 ± 12.9
	PFZ	2270 ± 10.09	2280 ± 10.08	✓	424 ± 6.88
	PUZ	2292 ± 8.97	2311 ± 10.39	✓	445 ± 10.8
	MIZ	2307	2314	-	449 ± 10.7
2016	STZ	2316 ± 26.45	2321 ± 16.54	✗	367 ± 9.08
	SAZ	2283 ± 17.77	2298 ± 20.18	✗	392 ± 16.0
	PFZ	2266 ± 8.040	2277 ± 4.189	✓	414 ± 7.41
	PUZ	2269 ± 15.14	2288 ± 5.986	✓	424 ± 10.00
2017	STZ	2326 ± 9.67	2307 ± 17.72	✓	382 ± 13.6
	SAZ	2311 ± 16.57	2312 ± 5.653	✗	398 ± 10.5
	PFZ	2277 ± 3.29	2276 ± 6.332	✗	423 ± 7.89
	PUZ	2299 ± 13.73	2293 ± 14.05	✗	445 ± 11.2
	MIZ	2304 ± 4.26	2306 ± 5.459	✗	438 ± 12.0

*Significant difference is statistically defined as a measurable difference between measured TA and LeeTA, with a p-value < 0.05. The dash signifies that there is not sufficient data to perform statistical analysis within the specified region.

4.4 SOCCOM float observations

The selected floats (9313, 9260, 9096) are taken to be representative of conditions from the STZ to the MIZ, in the Atlantic-Indian sector of the SO (Figure 4.15). Float 9313 was situated in the SAZ from December 2014 – April 2016 and moved to the STZ from April 2016 – November 2017. Float 9260 was located in the PFZ from January 2015 – October 2015. Float 9096 was located in the PUZ from December 2014 –September 2017 and moved to the MIZ from September 2017 – April 2018 (Figure 4.15). The selected floats were all operational in a similar time period from Oct 2014 – Oct 2015, whereas only floats 9313 and 9096 were both operational until 2018.

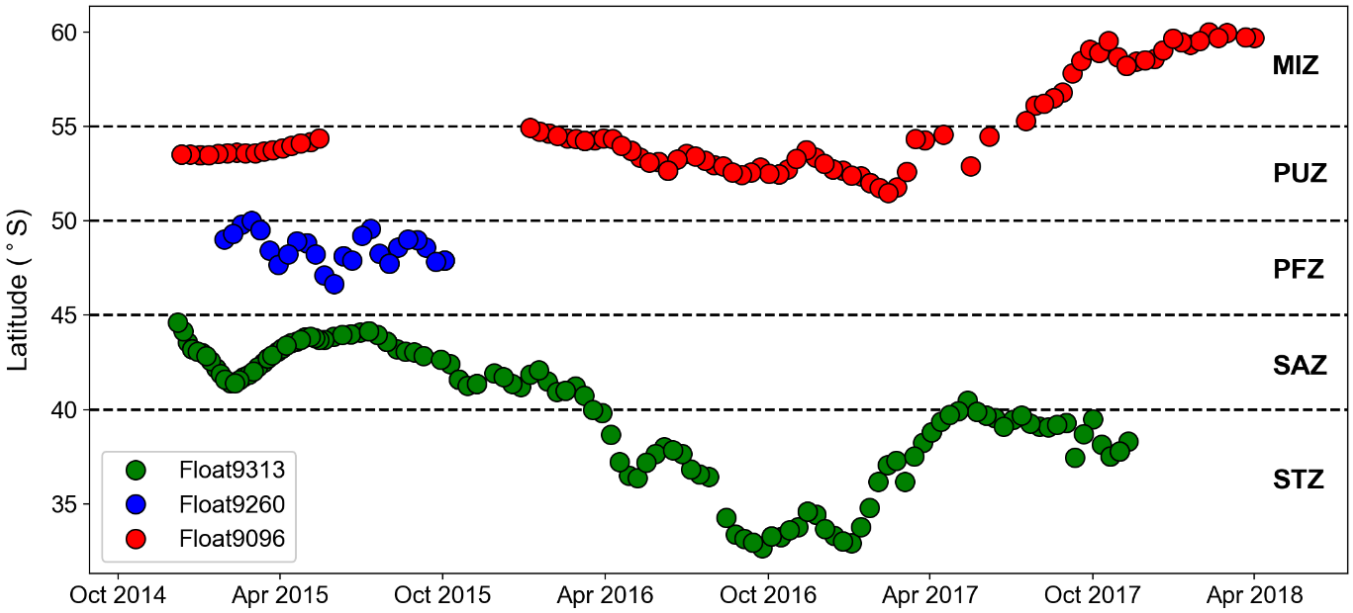

Figure 4.15: Latitudinal position of each selected float from December 2014 – April 2018

Figures 4.16 and 4.17 show the spatial distribution of the average measured TA over a two-degree latitude band, compared to LeeTA and LIAR_TA, from the STZ to the MIZ observed during WC2016 and WC2017, respectively. TA was seen to vary more in the Atlantic Ocean sector compared to the Indian Ocean sector, evident from the range of TA observed (2225 – 2360 µmol/kg and 2265 – 2345 µmol/kg, respectively). A similar trend was seen in both ocean basins with TA decreasing from the STZ to the PFZ and increasing from the PUZ to the MIZ.

A significant difference between TA measurements and LeeTA estimates are observed in the PFZ and PUZ in the Atlantic Ocean sector (WC2016) of the SO. LeeTA was observed to overestimate TA measurements in these regions during the "winter" season. By comparison,

there was no significant difference between observations and LeeTA in the Indian Ocean sector (WC2017) of the SO from the SAZ to the MIZ. The difference in the performance of LeeTA in these sectors is attributed to the bias of the Lee expression to summer, as conditions in the Indian Ocean sector have not yet transitioned into winter conditions.

LIAR_TA was observed to be within the margin of error of measured TA in the STZ and SAZ in the Atlantic Ocean sector during "winter" (Figure 4.16). However, the majority of the data points were captured outside of the winter season and are not consistent temporally with the time of WC2016 – only one data point corresponds in time and space in the SAZ (Figure 4.16). We note that in the SAZ, one data point seems to indicate that float-based data begins to overestimate ship-board measurements, however, there is not enough data available presently to confirm this. LeeTA (both ship and float-based) were observed to overestimate ship-board measurements of TA from the SAZ, leading into the PFZ and PUZ in the Atlantic sector. LIAR_TA performs better in the STZ which has a greater number of data points, and is not historically under-sampled, as is the case with the zones of the ACC, particularly in the winter season. This discrepancy between LIAR_TA and observed TA is further emphasised from the SAZ – PUZ in the Atlantic Ocean sector.

In the Indian Ocean sector, LIAR_TA estimates are observed to converge with TA measurements from the STZ into the SAZ (Figrure 4.17). We suspect that the convergence between observed TA and LIAR_TA occurs as a result of the assumed salinity values at this frontal position. However, the winter LIAR_TA observation heavily underestimates the TA observations in the STZ, and overestimates TA observations in the PUZ. LIAR_TA in the PUZ and MIZ are consistent with TA observations, within the margin of error. We suggest here that the LIAR_TA during the summer season better matches TA observations in the Indian Ocean sector during winter, due to the warmer ocean currents experienced in this ocean basin.

The deviations between LIAR_TA and Lee TA across the SO, at temperatures below 0 °C and between 11-12 °C are outlined in Appendix D, Section D.3.

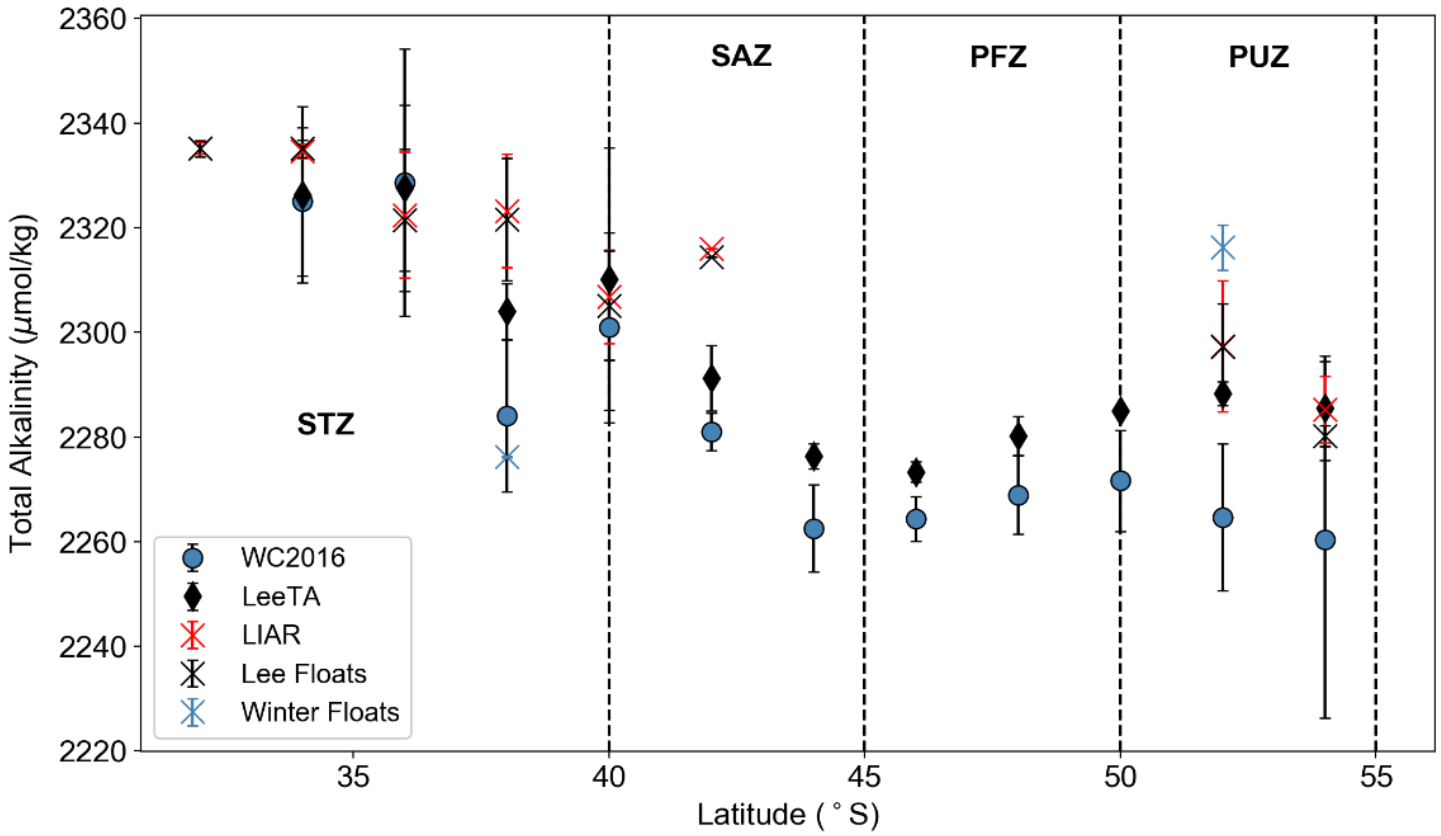

Figure 4.16: Winter cruise 2016 TA values in the Atlantic Ocean sector averaged over two degree intervals, compared to Lee TA and float LIAR_TA along the same latitude band in the year of 2016. TA ranged between 2225 – 2360 µmol/kg.

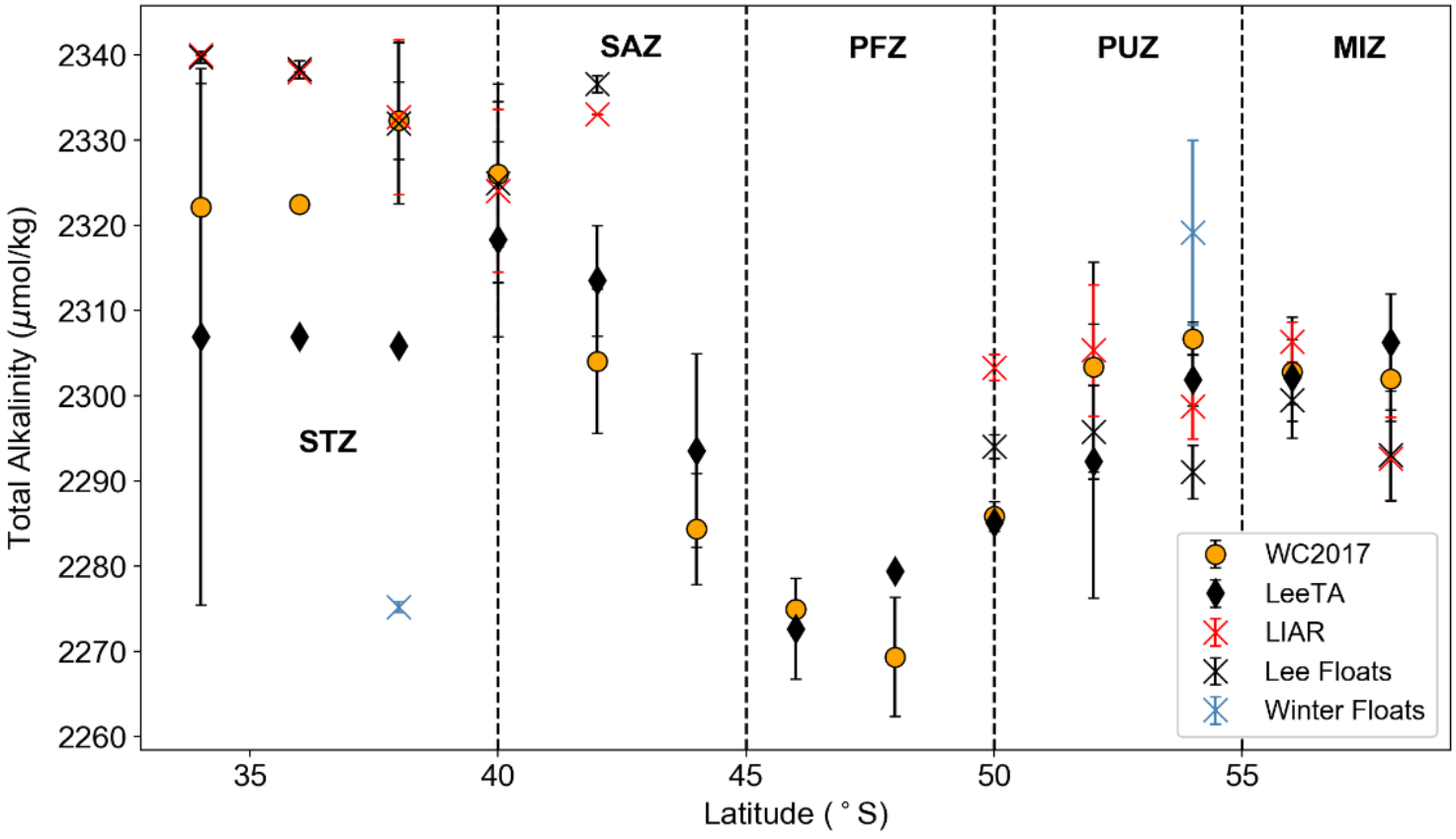

Figure 4.17: Winter cruise 2017 TA values in the Indian Ocean sector averaged over two degree intervals, compared to Lee TA and float LIAR_TA along the same latitude band in the year of 2017. TA ranged between 2265 – 2345 µmol/kg.

5 Discussion

5.1 Research questions

The discussion addresses the three main research questions of this study outlined in Section 2.2, namely:

- Can pH_T be used to estimate seasonal variations in pCO_2?
- What is the performance of the Lee formula in winter?
- How do SOCCOM results compare to ship- and glider-based measurements?

5.1.1 Can pH_T be used to estimate seasonal variations in pCO_2?

Due to a paucity of seasonal data in the Southern Ocean, climatology estimates of carbonate chemistry in the surface ocean are seasonally biased, thus high resolution spatial and temporal measurements of the carbonate system in seawater are necessary to reduce the uncertainty and biases for mean annual fluxes and constrain model predictions in this region (Williams et al., 2017, Gray et al., 2018, Takeshita et al., 2018, Gregor et al., 2018, Gruber et al., 2019). Resolving the seasonal cycle, to address the seasonal bias of the carbonate system, in the SO is a step towards reducing the uncertainty in empirical model estimates. An increased number of observations better distributed in space and time are starting to be achieved by the SOCCOM project, with the deployment of 200 profiling floats throughout the Southern Ocean that have been in operation since December 2014 (Group, 2016, Johnson et al., 2017). However, the floats are only capable of measuring one carbonate parameter (i.e., pH) and rely on the measurement of ancillary variables salinity, temperature, oxygen and nitrate to estimate a value for TA.

In this study, the WG dataset provides a unique simultaneous high resolution dataset of hourly measurements of pH_T and pCO_2 (Monteiro et al., 2015) over the spring-summer transition period in the SO, which allows for the calculation of TA and pCO_2 in the SAZ region of the SO to be resolved and compared to the derived estimates from ancillary variables. These high-resolution observations showed the effect of enhanced biological activity, the spring bloom, on the variability of the carbonate parameters in seawater at seasonal and inter-annual scales. This allows us to ascertain how these changes can affect our ability to predict TA by the means of empirical algorithms, and subsequently evaluate pH as an estimator of pCO_2.

Wave Glider Total Alkalinity (WGTA) was calculated from pH and $WGpCO_2$ and compared to LeeTA (Figure 4.8). There is a significant difference observed between WGTA and LeeTA

across the entire dataset, where LeeTA shows no change in TA during the transition from spring to summer. The Lee formula assumes a linear relationship with salinity in the region, and as such provides a higher estimate of TA (Lee et al., 2006). The salinity normalised WGTA is also shown in Figure 4.8 to account for possible contributions from changes in water physical properties in the surface ocean. However, a significant increase in normalised WGTA was still seen throughout the bloom period. We see from Figure 4.4 that salinity fluctuates between 34.15 and 34.4 PSU throughout the pre-bloom and bloom period and showed a weak freshening of the surface ocean toward the bloom period. The fluctuations in salinity were mirrored by the fluctuations seen in LeeTA over this period. This emphasises that the Lee formula is highly dependent on changes affecting salinity.

However, this does not account for other drivers of TA which can be affected by changes in pH_T via the precipitation/dissolution of calcite, and the uptake of nutrients in the surface ocean via the "nutrient-H^+-compensation principle" (Wolf-Gladrow et al., 2007). Thus, LeeTA during the pre-bloom period can potentially be attributed to the changes in salinity, however, the lower WGTA is proposed to indicate a more complex system of drivers at play in the surface ocean, which act to lower TA – for example, the precipitation of calcium carbonate, the remineralization of nutrients (Wolf-Gladrow et al., 2007), or the entrainment of nitrate below the mixed layer (Gregor et al., 2018).

The calculated WGTA also showed a seasonal trend in sharp contrast to LeeTA (Figure 4.8). The two showed a difference of 76.53 ± 14.77 μmol/kg in the pre-bloom and converged during the spring bloom (Figure 4.8). The increase in WGTA observed during the bloom period points to the reduction of nitrate in the surface ocean in the presence of increased biological activity (evident from the increase in chlorophyll-*a* noted in Figure 4.5).

The change in WGTA seen from the pre-bloom to the bloom period also coincides with the decrease in pCO_2 (expected from the biological uptake of CO_2 for photosynthesis) and the consequent increase in pH (Figure 4.6). Thus, the change in WGTA can be attributed to the impact of biological productivity in the region during the bloom period. Wolf-Gladrow et al., (2007) showed by the expression of TA_{ec} (Eq. 21, Section 1.4) that the uptake of 1 mole of nitrate or nitrite by photoautotrophs will lead to an increase in TA by 1 mole. Thus, we conclude that the Lee formula cannot resolve the seasonal changes in TA induced by nitrate uptake in the SO.

We suggest that summer bias stems from the foundation of the Lee formula as this empirical expression for TA is averaged over the entire Southern Ocean regime, with most measurements based in the summer season (Lee et al., 2006). The summer bias in the estimated TA suggests that a region and/or season specific formula for TA needs be devised. Considering that this bias exists here, it is probable that similar formulations for TA based on salinity and temperature data, which are calibrated in different regions, may not pertain to all sectors of the SO. Given what we now know of the TA seasonal cycle during the spring-summer period, we investigate the effect of the summer bias of the Lee formula on predicting pCO_2 from pH (Figure 4.7).

The largest disparity between the measured and calculated pCO_2 occurred during the pre-bloom period, with differences in pCO_2 ranging from 5 – 20 μatm i.e. $LEEpCO_2$ was significantly higher than $WGpCO_2$ during the pre-bloom period. However, $LEEpCO_2$ was more accurate during and after the bloom period with an average difference in pCO_2 ($LEEpCO_2 – WGpCO_2$) of ± 5 μatm. $LEEpCO_2$ and $WGpCO_2$ were also not significantly different during the bloom period. The overestimation of pCO_2 in the pre-bloom period suggests that the summer bias in LeeTA leads to higher estimates of pCO_2 in pre-bloom conditions. Our results suggest that if current TA algorithms are used with measured pH_T, there is potential to overestimate pCO_2 by 3.6% during pre-bloom conditions.

Thus, our ability to predict pCO_2 accurately from pH_T is limited by the accuracy of the TA algorithm to resolve the seasonal cycle of TA. We have shown here that the seasonal cycle for TA that is predominantly driven by nitrate uptake in the summer and re-entrainment in the winter. The Lee formula causes a further seasonal bias in the calculation of pCO_2, as it does not factor in the impact of nitrate uptake on TA. As a result, we conclude that pH_T can only be used as a predictor for pCO_2 if concurrent measurements of TA are observed, or if the Lee et al., (2006) formula can be corrected for the uptake of nitrate from nitrate observations i.e. a critical component of elucidating the regional differences in pCO_2 is first resolving the seasonal cycle of TA, and determining what impact this has on the estimation of pCO_2 in the SO.

Further evaluation of TA is required in the winter season SO to confirm that there is no change across the different zones of the ACC, perhaps zone and/or sector specific algorithms required to calculate TA are necessary here as well – more observations are needed to resolve the scope of this phenomenon across the seasonal cycle in the SO.

5.1.2 What is the performance of the Lee algorithm in austral winter across the Southern Ocean?

We have established that the largest discrepancy in calculated pCO_2 from pH_T and LeeTA occur during the pre-bloom period, prior to the onset of spring. This indicates that the bias in the calculated pCO_2 extends back into the winter season, and therefore potentially overestimates the magnitude of pCO_2 particularly during that part of the seasonal cycle.

A recent study by Gray et al., (2018), suggested that the amplitude of the pCO_2 seasonal cycle is underestimated by ship-board measurements, as they found that the calculated pCO_2 derived from float-based data was consistently higher than ship-board measurements in the PUZ and MIZ during autumn and winter. Gray et al., (2018) suggested that the large source of CO_2 from the PUZ during the winter season may be compensated for by a stronger CO_2 sink in another ocean region. Similarly, Williams et al., (2017) compared float-based data to climatological data for pCO_2 and found that most discrepancies between the datasets occurred in the PUZ, where float-based data indicated a source of CO_2 to the atmosphere, as opposed to the neutral sink/source implied by climatology. However, in our study of surface ocean pCO_2 derived from pH and LeeTA, we observed lower pCO_2 values than would be calculated using algorithms similar to the float-based approach, prior to the onset of the spring-summer season in the SO.

The seasonal cycle of pCO_2 in the SO winter is driven by the southward deepening of the mixed layer depth, indicating that light and iron limitation in the SO are inhibiting biological productivity, and a resupply of enriched waters to the surface ocean via upwelling increases pCO_2 in the surface ocean (Gregor et al., 2018). Thus, there is a higher concentration of pCO_2 measured in the surface ocean moving poleward during the winter season (Figure 4.12). In the summertime, this shifts as temperature and biological activity driven changes predominate, the melting of sea-ice provide a source of iron, and the stratification of the surface ocean promotes biological activity through added light limitation, thereby lowering the pCO_2 concentration in the surface ocean (Gregor et al., 2018).

Thus, to assess if float-derived pCO_2 are anomalous due to a bias in resolving TA through empirical algorithms in the winter, we look at the Lee formula across the seasonal cycle. Here, we compare observational data obtained from winter-time research cruises in the SO, across the Atlantic and Indian Ocean sectors. WC2015 and WC2016 took place along the Good Hope transect from June – July 2015 and July – August 2016, respectively in the Atlantic Ocean

sector. WC2017 took place across a transect in the Indian Ocean sector of the SO from June – July 2017 down to 62 °S in the winter MIZ (Figure 3.2).

Discrete measurements of TA (Figure 4.14) are seen to decrease from the STZ to the PFZ, and increase in the southern most regions of the PUZ and MIZ. The decrease in TA can be attributed to added precipitation along the transect moving south, as well as Ekman transport, which coincides with the freshening of the surface waters (Figure 4.10). The increase in TA can be attributed to the upwelling of deep water in this region (Figure 4.11), coupled with biological productivity taking place in the MIZ through sea-ice brine channels, where we also see a corresponding slight decrease in nitrate (Figure 4.12). The increase in TA observed during WC2017 (Indian Ocean sector of the SO) was seen to plateau in the MIZ region. However, in the Atlantic sector, both WC2015 and WC2016 show a rise in TA from the PUZ to the MIZ, with no corresponding change in nitrate (Figure 4.12). There was a significant difference in TA observed between WC2016 and WC2017 from the SAZ to the PUZ, indicating that the Indian and Atlantic Ocean sectors of the SO are sufficiently different to warrant a region specific formula to estimate TA.

We compare the discrete measurements of TA to the Lee et al., (2006) estimated TA (Figure 4.15). We see that for WC2017 in the Indian Ocean, there is no significant difference between measured TA and the corresponding LeeTA. Conversely, TA for both WC2015 and WC2016 are significantly different from the corresponding LeeTA estimates in the Atlantic Ocean sector of the SO, particularly in the PFZ and PUZ where LeeTA overestimates observations. These regions coincide with colder temperatures and more saline waters in the Atlantic Ocean sector as compared to the Indian Ocean sector of the SO (Figures 4.10 and 4.11). This suggests that the Indian Ocean sector still exhibits Lee expression characteristics into what is considered the austral "winter" season i.e. the warmer and more saline waters of the Indian Ocean mimic summer biogeochemical trends, and thus early austral winter in the SO is thus less pronounced in this sector.

Comparing our ship-board measurements to those collected from the WG, we would expect the difference in LeeTA and observations to be most divergent in the winter season. However, we see that there is still a large discrepancy between data gathered by ship-board measurements in the periods from late June to early August, and the WG data gathered from mid-October into December. Pre-bloom averages of WGTA (2206 ± 13.86 μmol/kg) are significantly lower than Winter Cruise TA observations in the SAZ (2287 ± 5.181 μmol/kg, 2298 ± 20.18 μmol/kg and

2312 ± 5.653 μmol/kg for WC2015 – WC2017, respectively). Thus, the late August to early October period that would represent the winter-spring transition period, remains unaccounted for as there is no available data.

Assuming that the WG is representative of the spring-summer transition period, the discrepancy between the WC observations in June – August combined with the WGTA estimates in October – November during the pre-bloom period suggest that there is a further decrease (approximately 81 – 92 μmol/kg) in TA occurring in the SAZ between August and October. By comparison with WGTA, the higher LeeTA estimates during October (Figure 4.8) are likely an artefact of the summer bias in observations on which the algorithm is built. Thus, the discrepancy that occurs between WC and WG data for the winter-spring period, indicates that there is likely a shift in drivers affecting TA that promote a lower TA concentration.

It is expected that TA would decrease during winter via entrainment and the reduction in biological productivity from light limitation coupled with the deepening of the mixed layer depth, however, it is difficult to resolve which process dominates the lowering of TA in this period without available data. To reconcile the discrepancy for the proposed winter-spring transition period, we suggest that the WC observations presented here are more representative of the autumn-winter transition period, rather than the winter period itself.

This idea is re-enforced by looking at the differences in nitrate concentrations between the Atlantic and Indian Ocean sectors of the SO (Figure 4.12). No significant difference in nitrate concentration was observed for WC2016 and WC2015 along the same transect, indicating that the Atlantic Ocean sector is closer autumn-winter transition state period. However, there was a significant difference observed between WC2016 and WC2017 from the SAZ to the PUZ. We suggest that this is due to the Indian Ocean sector not having completed the transition to the winter season – as opposed to the Atlantic Ocean sector, where nitrate concentrations are significantly higher than those observed in the Indian Ocean sector (Appendix B, Table B5).

Our results showed that LeeTA is significantly different from ship-board measurements of TA in the Atlantic Ocean sector of the SO as compared to the Indian Ocean sector, during the "winter" season i.e. the Lee algorithm is unable to predict TA in the "winter" season in the Atlantic Ocean sector. Thus, future developments of TA expressions should look at formulating an algorithm in each sector, and in particular, the PFZ, PUZ and MIZ regions based on repeat hydrography in different seasons. Autonomous systems will be paramount in

constraining the seasonal cycle of TA and gather much needed data to further constrain Earth's system models, and to determine which regions are thus responsible for carbon drawdown and carbon efflux.

5.1.3 How do SOCCOM results compare to ship- and glider-based measurements?

Gregor et al., (2018) showed that a discrepancy between empirical products for the prediction of pCO_2 resulted in a low confidence of changes in pCO_2 on a regional scale throughout the SO, despite a consistency in overall trends between the empirical products. We see that TA also varies in the different regions of the SO, with empirical algorithms of TA able to predict TA in the Indian Ocean sector than the Atlantic Ocean sector more accurately during the autumn-winter season. The Locally Interpolated Alkalinity Regression (LIAR) method (Carter et al., 2016) to interpolate TA across the SO is another empirical product, such as the Lee et al., (2006) formula, that is used to interpret the SOCCOM project float measurements. Here we discuss what implications the findings above have on the calculation of pCO_2 from float-derived TA (LIAR_TA).

Although the SOCCOM floats are able to gain coverage of the SO in the winter, the Atlantic and Indian Ocean sectors in line with the Good Hope Line are still under-represented for the winter season – with only two operational floats out of a fleet of approximately 100 deployed floats to observe winter conditions in the STZ and MIZ regions of the SO. The disadvantage of the floats are that they cannot be controlled remotely in order to gather location-specific data. The risk here is collecting a bias of information as floats are subject to the flow of the current and cannot target specific areas of interest outside of this flow. Observations of TA are needed across all seasonal conditions to create an accurate representation of the seasonal cycle of TA in the SO.

This study considered three floats in the Southern Ocean, spanning across the Atlantic and Indian Ocean basins down to the marginal ice zone (Figure 3.2). A comparative analysis of LeeTA, LIAR_TA, WGTA and ship-board measurements of TA will be explored in this section. SOCCOM observational data is illustrated in Appendix B. To understand the SOCCOM float data in context of the TA seasonal cycle, we compare these data to measurements from WC2016 and WC2017 (Figures 4.16 and 4.17). A further seasonal bias analysis was compiled with the addition of GLODAPv2.2019 data from the glider location and compared with SOCCOM Float 9313 LIAR_TA, LeeTA values, WC and WGTA (Appendix D, Section D.2).

The corresponding LeeTA estimates for float-based measurements (LeeFloats) are not significantly different from LIAR_TA for WC2016 and WC2017 (p-value significant

difference tables can be found in Appendix C), which indicate that calculations are largely dependent on salinity, and must be adjusted to account for the seasonal cycle of TA when biological controls of TA are dominant. WC2017 showed no significant difference with corresponding LeeTA values in the Indian Ocean, across all zones of the ACC. In comparison, both WC2015 and WC2016 showed a significant difference with corresponding LeeTA values with particular emphasis on the PFZ and PUZ. LIAR_TA and the corresponding LeeTA estimates are not significantly different, which indicate that the LIAR algorithm is potentially subject to the same winter bias as the Lee expression.

Figure 5.1 shows the WGTA and the corresponding LeeTA averaged over two-day intervals from Oct – Dec 2013. LIAR_TA is shown in the same region during Dec 2014. WGTA indicated consistent TA during the pre-bloom period, and an increasing trend during the bloom period (Section 5.1). The corresponding LeeTA estimates based on WG measurements showed a constant TA throughout the period, with no variation corresponding to the seasonal changes. LeeTA was seen to overestimate WGTA in the pre-bloom period, and underestimate WGTA during the bloom period. In comparison to LeeTA and WGTA, we observed that LIAR_TA

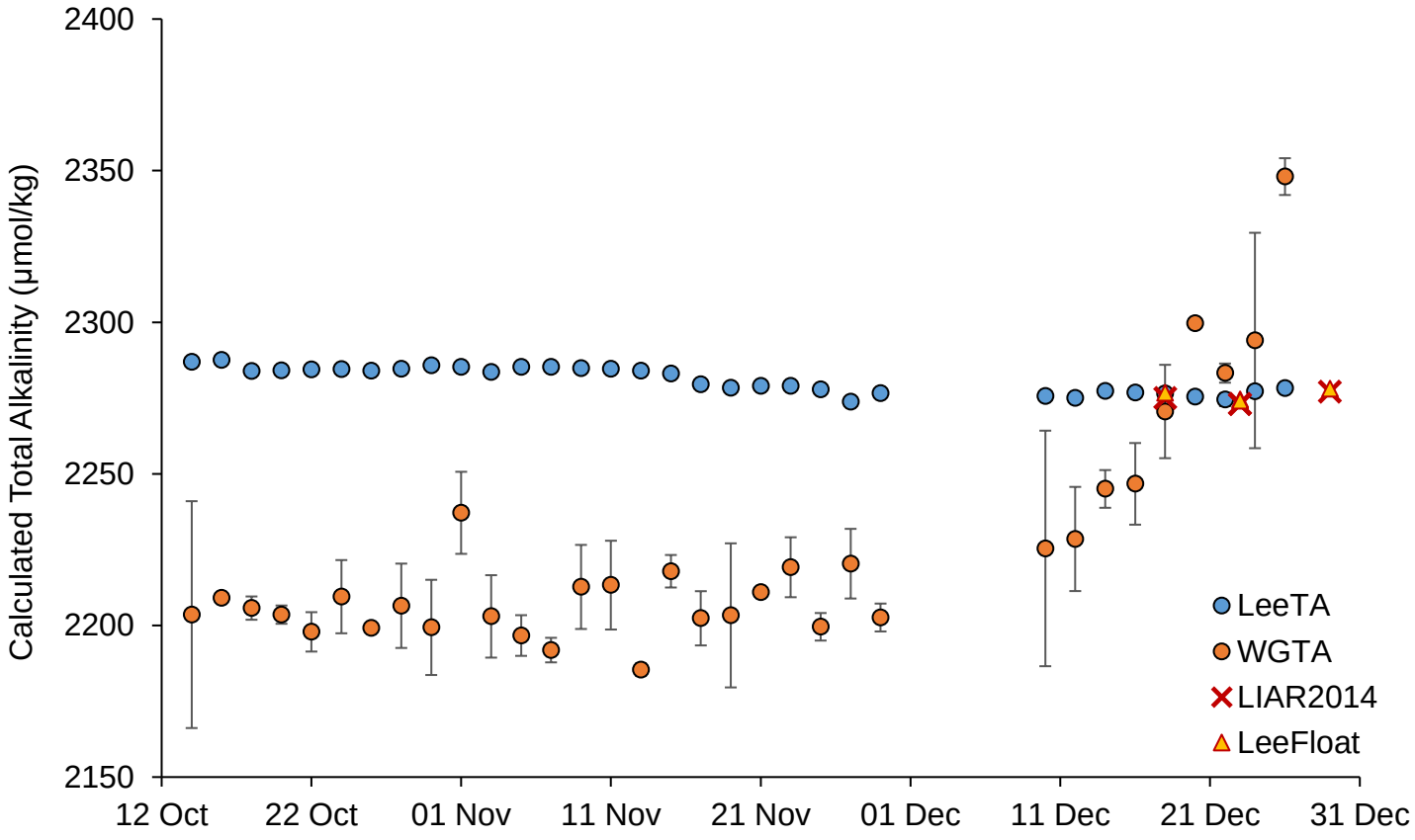

Figure 5.1: WGTA averaged over two days intervals compared with estimated LeeTA, and LIAR_TA estimates for Dec 2014

corresponds exactly with the LeeTA estimate during the bloom period. Although LIAR_TA and LeeTA only coincide in space, we expect to observe increased TA during the summer season. This indicates that the LIAR_TA estimate is also strongly driven by changes in salinity and does not adequately account for the increase in TA due to nitrate uptake.

We know that the uptake of nitrate in the summer season drives an increase in TA, however, this is not accounted for in the Lee formula, causing an uncertainty in the subsequent pCO_2 calculation. The uncertainty in the calculation of pCO_2 is highest in the winter season when the error between observed TA and derived TA is most apparent (Figure 4.7).

To illustrate the magnitude of the effect a change in TA due to nitrate uptake has on the estimation of pCO_2 under winter time conditions, we present four scenarios based on data obtained from Float 9096 situated in the PUZ and MIZ of the SO. We expect low concentrations of TA in the winter season as established from the WG dataset. Figure 5.2 shows the difference in pCO_2 calculated from LIAR_TA and pH, and the calculated pCO_2 from pH and a decrease in LIAR_TA by 10, 20, 30 and 50 µmol/kg for scenario 1 – 4, respectively.

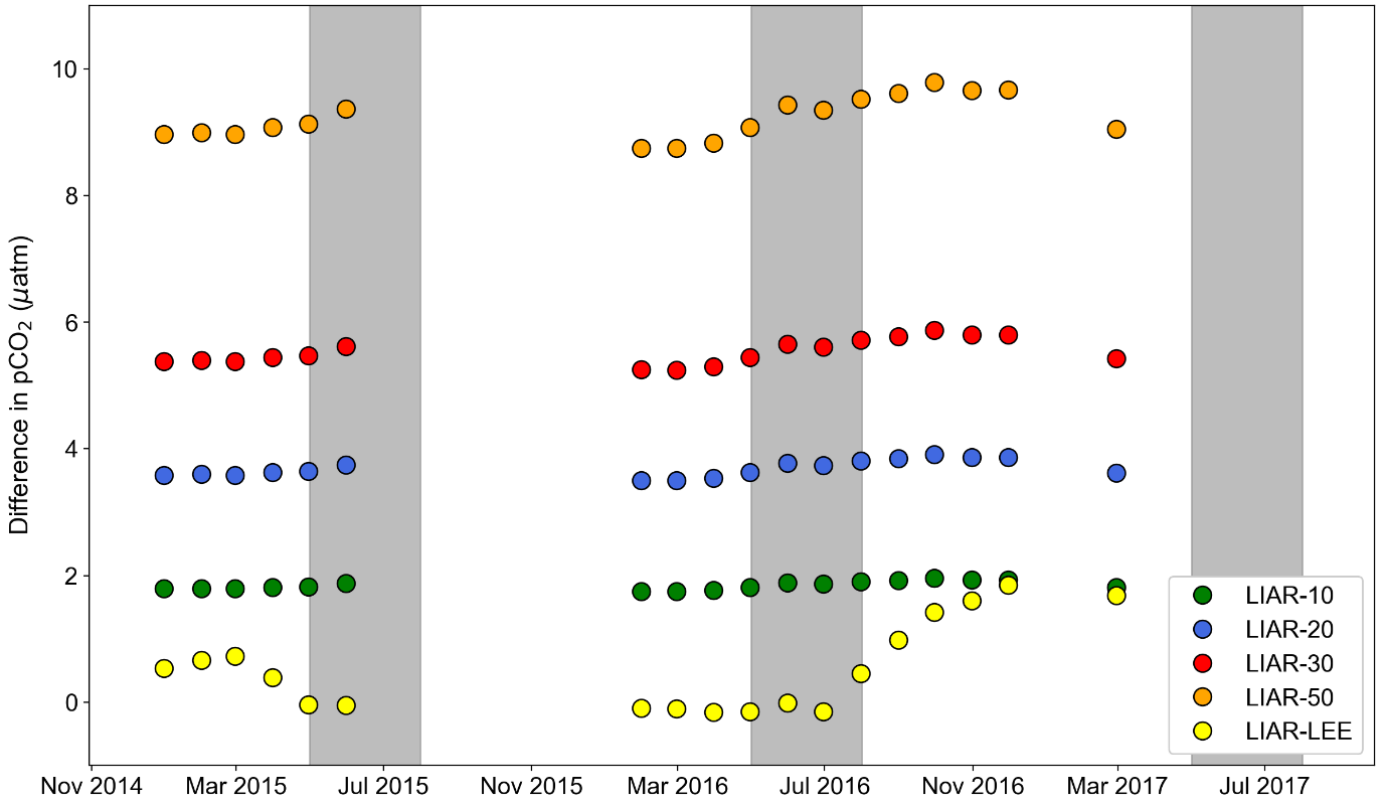

Figure 5.2: pCO_2 scenarios based on the difference in calculated pCO_2 between pCO_2 as a function of LIAR_TA and pH and pCO_2 as a function of LIAR_TA corrected for nitrate and pH. *Scenario 1:* LIAR_TA less 10 µmol/kg, *Scenario 2:* LIAR_TA less 20 µmol/kg, *Scenario 3:* LIAR_TA less 30 µmol/kg, *Scenario 4:* LIAR_TA less 50 µmol/kg and the difference between LIARpCO_2 and LEEpCO_2. Data used to render this graph applies to Float 9096 in the PUZ.

We see that there is an inverse relationship between LIAR_TA and the calculated pCO_2. The lower the concentration of LIAR_TA, the greater the difference in calculated pCO_2. This shows that not considering nitrate-linked changes in the calculation of TA will lead to an overestimation of pCO_2 in the surface ocean i.e. measurements of nitrate are essential to resolving the seasonal cycle of TA. This consideration may account for the discrepancy between float estimated pCO_2 exceeding ship-based pCO_2 measurements in the surface ocean in the PUZ of the SO as reported by Williams et al., (2017) and Gray et al., (2018).

The implications of this inverse relationship suggest that the discrepancy observed between WGTA and LeeTA (Figure 5.1) with a difference of ~ 100 µmol/kg in the pre-bloom period, indicates that the lowering the LeeTA concentration can lead to an increased change in pCO_2, or rather in the case of LeeTA, to reconcile the difference discrepancy observed in pre-bloom conditions as the formula is optimised for nitrate uptake in the summer season. A further analysis of this scenario is shown in Appendix D, Section D.4.

Another factor that may contribute to the elevated calculated pCO_2 estimates from float-based measurements, is the sampling frequency at which the seasonal cycle of pCO_2 is extrapolated from. Monteiro et al., (2015) reported an alias in sampling frequency of the mean hourly flux of CO_2, are highest in the SAZ and MIZ with a sampling time frame of 10 days. The uncertainty in the measurement of the hourly mean flux of CO_2 increases with the sampling time frame for example, from one day to 10-day sampling intervals. Thus, it is more likely to calculate a mean that is significantly different to the hourly mean. The study also reported that the sampling alias occurred more frequently in the Atlantic Ocean sector of the SO (Monteiro et al., 2015). This may also account for the regional differences we observe between derived TA between the Atlantic and Indian Ocean sectors of the SO.

Considering that the SOCCOM float measurements occur at a 10-day frequency, it is possible that a sampling alias exists, and as such, the accurate prediction of pCO_2 across the seasonal cycle is influenced (Monteiro et al., 2015). The floats do not acquire repeat measurements in the same position every 10 days, but rather dive down to greater depths and move with the flow of current. Thus, the floats are measuring the surface ocean through bloom and non-bloom conditions, and as suggested by our WG dataset, accurate measurements of pCO_2 may be difficult to attain if captured in pre-bloom conditions.

Our study of ship-based TA observations, LIAR_TA and LeeTA suggest that more data is needed in the winter season to draw more conclusive findings. However, this initial

investigation indicates that TA is varying across zones and sectors of the SO, which make it difficult for empirical algorithms based on salinity and temperature to predict changes in the seasonal cycle of TA i.e. the regional changes in TA are aggregated when averaged across the entire SO regime, as is the case with the Lee et al., (2006) formula, and influenced by the summer bias of TA due to the higher resolution of data in the summer season. Autonomous measuring platforms are necessary to resolve the seasonal bias in the SO due to the paucity in winter-time data, as well as constrain the differences between each sector. However, the sparse data collected at 10-day intervals by the SOCCOM project cannot accurately convey trends in TA on the intra-seasonal scale.

The seasonal cycle of TA across each ocean sector of the SO needs to be constrained by measurements of nitrate to determine more accurate estimates of pCO_2 in the surface ocean, particularly in the winter season. A preliminary analysis of the impacts of the nitrate seasonal cycle on TA are discussed in Appendix D, Section D.5. Our current understanding of the seasonal dynamics of the CO_2 in the SO is dependent on the accuracy of the empirical TA algorithms, which are better predictors of pCO_2 in the summer season. Given the potential bias of TA algorithms, we can expect elevated pCO_2 estimates in the winter season until the seasonal cycle of TA in each sector of the SO can be better resolved.

Possible experiments to achieve the accurate prediction of pCO_2 during the winter season would involve gathering more surface measurements by the floats at a higher sampling frequency in different sectors to reduce a regional bias. This would give us a better idea of the intra-seasonal dynamics in each sector in the SO, as well as constrain the empirical TA algorithms and allow for the improved location-specific prediction of pCO_2.

6 Conclusions and recommendations

Conclusions

The aim of this study was to investigate whether pH_T together a simple algorithm for the calculation of TA, could be used to determine an accurate measure of pCO_2 and the carbonate system in seawater. We have shown that the changes in TA related to the seasonal cycle of nitrate are critical to the correct estimation of the seasonal cycle of pCO_2 and its fluxes in the SO.

The high resolution Wave Glider observations in the sub-Antarctic zone of the Southern Ocean showed that the seasonal variation of TA was larger than predicted by empirical algorithms (Lee et al., 2006, Carter et al., 2016) in the summer season. The main reason was that the empirical formulations are unable to resolve the seasonal changes in TA, which are attributed to the uptake of nitrate in the summer time and the entrainment of nitrate below the mixed layer depth in the winter time.

Evaluating the Lee formula against ship-board observations of TA taken during the autumn-winter season, show a significant difference in TA between the Atlantic and Indian Ocean sectors of the Southern Ocean. This re-enforces that there are also regional differences in the seasonal cycle of TA that cannot be accounted for by the empirical algorithms which are averaged over the entire Southern Ocean basin. Therefore, it is suggested that TA algorithms be devised per region to better constrain the seasonal cycle of TA in the SO.

The magnitude of the bias of the TA expressions on pCO_2 was shown to decrease by constraining the effect of nitrate on the seasonal cycle of TA. The assessment of float-based measurements also demonstrated that pCO_2 may be overestimated as the winter season progresses, stemming from the bias in calculated TA due to changes in the uptake of nitrate. The effect of nitrate on the seasonal cycle of TA must be accounted for in order to reduce uncertainty in pCO_2 estimates.

Hence, it is recommended that an additional carbonate variable be measured alongside pH_T in order to elucidate seasonal changes in TA, or that the impact of the uptake of nutrients by the spring bloom on TA be corrected for.

Recommendations for future study

To further this study, the following recommendations and improvements can be considered for further experimentation:

More high-resolution data collection of SO sea surface TA and nitrate concentrations are needed to resolve trends in the seasonal cycles of TA and nitrate. Together, these measurements can be used to develop more accurate expressions of TA, and to reduce the uncertainty in pCO_2 estimates prior to the summer season.

The WG could be deployed in different zones of varying sectors to gain a greater understanding of the seasonal changes in the SO. CTD profiles and underway samples should be included in the calibration protocol for glider recoveries and deployments. At these stations, duplicate sampling of CTD cast and underway samples can be used to calibrate glider measurements and account for sensor drift over time.

The SOCCOM comparison to should be extended to analyse other sectors and zones of the SO around the Antarctic continent, with particular emphasis on the winter season i.e. segment float data per ocean basin and zone across the ACC to constrain regions of pCO_2 sinks and sources.

The sampling frequency of the SOCCOM floats should be increased during the inter-seasonal periods at opportunistic events, which can be determined by monitoring satellite ocean colour and sea-ice cover data.

References

ANTON, V., F. PÉREZ, F., LIN, X., M. KEY, R., TANHUA, T., DE LA PAZ, M., OLSEN, A., VAN HEUVEN, S., JUTTERSTRÖM, S. & RIOS, A. 2010. *CARINA data synthesis project: pH data scale unification and cruise adjustments*.

BAKKER, D. C. E., HOPPEMA, M., SCHRÖDER, M., GEIBERT, W. & DE BAAR, H. J. W. 2008. A rapid transition from ice covered CO_2-rich waters to a biologically mediated CO_2 sink in the eastern Weddell Gyre. *Biogeosciences Discussions,* 5**,** 1205-1235.

BAKKER, D. C. E., PFEIL, B., O'BRIEN, K. M., CURRIE, K. I., JONES, S. D., LANDA, C. S., LAUVSET, S. K., METZL, N., MUNRO, D. R., NAKAOKA, S.-I., OLSEN, A., PIERROT, D., SAITO, S., SMITH, K., SWEENEY, C., TAKAHASHI, T., WADA, C., WANNINKHOF, R., ALIN, S. R., BECKER, M., BELLERBY, R. G. J., BORGES, A. V., BOUTIN, J., BOZEC, Y., BURGER, E., CAI, W.-J., CASTLE, R. D., COSCA, C. E., DEGRANDPRE, M. D., DONNELLY, M., EISCHEID, G., FEELY, R. A., GKRITZALIS, T., GONZÁLEZ-DÁVILA, M., GOYET, C., GUILLOT, A., HARDMAN-MOUNTFORD, N. J., HAUCK, J., HOPPEMA, M., HUMPHREYS, M. P., HUNT, C. W., IBÁNHEZ, J. S. P., ICHIKAWA, T., ISHII, M., JURANEK, L. W., KITIDIS, V., KÖRTZINGER, A., KOFFI, U. K., KOZYR, A., KUWATA, A., LEFÈVRE, N., LO MONACO, C., MANKE, A., MARREC, P., MATHIS, J. T., MILLERO, F. J., MONACCI, N., MONTEIRO, P. M. S., MURATA, A., NEWBERGER, T., NOJIRI, Y., NONAKA, I., OMAR, A. M., ONO, T., PADÍN, X. A., REHDER, G., RUTGERSSON, A., SABINE, C. L., SALISBURY, J., SANTANA-CASIANO, J. M., SASANO, D., SCHUSTER, U., SIEGER, R., SKJELVAN, I., STEINHOFF, T., SULLIVAN, K., SUTHERLAND, S. C., SUTTON, A., TADOKORO, K., TELSZEWSKI, M., THOMAS, H., TILBROOK, B., VAN HEUVEN, S., VANDEMARK, D., WALLACE, D. W. R. & WOOSLEY, R. 2016. Surface Ocean CO2 Atlas (SOCAT) V4. PANGAEA.

BREWER, P. G., BRADSHAW, A. L. & WILLIAMS, R. T. 1986. Measurements of Total Carbon Dioxide and Alkalinity in the North Atlantic Ocean in 1981. *In:* TRABALKA, J. R. & REICHLE, D. E. (eds.) *The Changing Carbon Cycle: A Global Analysis.* New York, NY: Springer New York.

BREWER, P. G. & GOLDMAN, J. C. 1976. Alkalinity changes generated by phytoplankton growth1. *Limnology and Oceanography,* 21**,** 108-117.

BREWER, P. G., WONG, G. T., BACON, M. P. & SPENCER, D. W. 1975. An oceanic calcium problem? *Earth and Planetary Science Letters,* 26**,** 81-87.

CARTER, B. R., FEELY, R. A., WILLIAMS, N. L., DICKSON, A. G., FONG, M. B. & TAKESHITA, Y. 2018. Updated methods for global locally interpolated estimation of alkalinity, pH, and nitrate. *Limnology and Oceanography: Methods,* 16**,** 119-131.

CARTER, B. R., WILLIAMS, N. L., GRAY, A. R. & FEELY, R. A. 2016. Locally interpolated alkalinity regression for global alkalinity estimation. *Limnology and Oceanography: Methods,* 14**,** 268-277.

CHEN, C.-T. A. 1978. Decomposition of Calcium Carbonate and Organic Carbon in the Deep Oceans. *Science,* 201**,** 735-736.

CLAYTON, T. D. & BYRNE, R. H. 1993. Spectrophotometric seawater pH measurements: total hydrogen ion concentration scale calibration of m-cresol purple and at-sea results. *Deep Sea Research Part I: Oceanographic Research Papers,* 40**,** 2115-2129.

CLAYTON, T. D., BYRNE, R. H., BRELAND, J. A., FEELY, R. A., MILLERO, F. J., CAMPBELL, D. M., MURPHY, P. P. & LAMB, M. F. 1995. The role of pH measurements in modern oceanic CO2-system characterizations: Precision and thermodynamic consistency. *Deep Sea Research Part II: Topical Studies in Oceanography,* 42**,** 411-429.

DICKSON, A. G. 1981. An exact definition of total alkalinity and a procedure for the estimation of alkalinity and total inorganic carbon from titration data. *Deep Sea Research Part A. Oceanographic Research Papers,* 28**,** 609-623.

DICKSON, A. G. 1990. Thermodynamics of the dissociation of boric acid in synthetic seawater from 273.15 to 318.15 K. *Deep Sea Research Part A. Oceanographic Research Papers,* 37**,** 755-766.

DICKSON, A. G. & GOYET, C. 1994. Handbook of methods for the analysis of the various parameters of the carbon dioxide system in sea water. Version 2. Oak Ridge National Lab., TN (United States).

DICKSON, A. G., SABINE, C. L., CHRISTIAN, J. R. & ORGANIZATION, N. P. M. S. 2007. *Guide to Best Practices for Ocean CO2 Measurements,* North Pacific Marine Science Organization.

EMERSON, S. & HEDGES, J. 2008. *Chemical Oceanography and the Marine Carbon Cycle,* Cambridge University Press.

EMERY, W. J. 2015. OCEANOGRAPHIC TOPICS | Water Types and Water Masses. *In:* NORTH, G. R., PYLE, J. & ZHANG, F. (eds.) *Encyclopedia of Atmospheric Sciences (Second Edition).* Oxford: Academic Press.

ETHERIDGE, D. M., STEELE, L. P., LANGENFELDS, R. L., FRANCEY, R. J., BARNOLA, J. M. & MORGAN, V. I. 1996. Natural and anthropogenic changes in atmospheric CO2 over the last 1000 years from air in Antarctic ice and firn. *Journal of Geophysical Research: Atmospheres,* 101**,** 4115-4128.

FRANSSON, A., CHIERICI, M. & ANDERSON, L. G. 2004. Diurnal variability in the oceanic carbon dioxide system and oxygen in the Southern Ocean surface water. *Deep Sea Research Part II: Topical Studies in Oceanography,* 51**,** 2827-2839.

FRIIS, K., KÖRTZINGER, A. & WALLACE, D. W. R. 2003. The salinity normalization of marine inorganic carbon chemistry data. *Geophysical Research Letters,* 30.

FRÖLICHER, T. L., SARMIENTO, J. L., PAYNTER, D. J., DUNNE, J. P., KRASTING, J. P. & WINTON, M. 2015. Dominance of the Southern Ocean in Anthropogenic Carbon and Heat Uptake in CMIP5 Models. *Journal of Climate,* 28**,** 862-886.

GOLDMAN, J. C. & BREWER, P. G. 1980. Effect of nitrogen source and growth rate on phytoplankton-mediated changes in alkalinity1. *Limnology and Oceanography,* 25**,** 352-357.

GRAY, A. R., JOHNSON, K. S., BUSHINSKY, S. M., RISER, S. C., RUSSELL, J. L., TALLEY, L. D., WANNINKHOF, R., WILLIAMS, N. L. & SARMIENTO, J. L. 2018. Autonomous Biogeochemical Floats Detect Significant Carbon Dioxide Outgassing in the High-Latitude Southern Ocean. *Geophysical Research Letters,* 45**,** 9049-9057.

GREGOR, L. 2017. *Improved estimates and understanding of interannual trends of CO2 fluxes in the Southern Ocean.* PhD, University of Cape Town.

GREGOR, L., KOK, S. & MONTEIRO, P. M. S. 2018. Interannual drivers of the seasonal cycle of CO2 in the Southern Ocean. *Biogeosciences,* 15**,** 2361-2378.

GROUP, B.-A. P. 2016. The scientific rationale, design and implementation plan for a Biogeochemical-Argo float array.

GRUBER, N., LANDSCHÜTZER, P. & LOVENDUSKI, N. S. 2019. The Variable Southern Ocean Carbon Sink. *Annual Review of Marine Science,* 11**,** 159-186.

HANSSON, I. 1973. A new set of pH-scales and standard buffers for sea water. *Deep Sea Research and Oceanographic Abstracts,* 20**,** 479-491.

HARRIS, D. C. 2010. *Quantitative Chemical Analysis,* W. H. Freeman.

HOUSECROFT, C. E. & SHARPE, A. G. 2005. *Inorganic Chemistry,* Pearson Prentice Hall.

JOHNSON, K., S., PLANT, J., N., COLETTI, L., J., JANNASCH, H., W., SAKAMOTO, C., M., RISER, S., C., SWIFT, D., D., WILLIAMS, N., L., BOSS, E., HAËNTJENS, N., TALLEY, L., D. & SARMIENTO, J., L. 2017. Biogeochemical sensor performance in the SOCCOM profiling float array. *Journal of Geophysical Research: Oceans*, 122**,** 6416-6436.

JOHNSON, K. S., JANNASCH, H. W., COLETTI, L. J., ELROD, V. A., MARTZ, T. R., TAKESHITA, Y., CARLSON, R. J. & CONNERY, J. G. 2016. Deep-Sea DuraFET: A Pressure Tolerant pH Sensor Designed for Global Sensor Networks. *Analytical Chemistry*, 88**,** 3249-3256.

KEY, R. M., KOZYR, A., SABINE, C. L., LEE, K., WANNINKHOF, R., BULLISTER, J. L., FEELY, R. A., MILLERO, F. J., MORDY, C. & PENG, T.-H. 2004. A global ocean carbon climatology: Results from Global Data Analysis Project (GLODAP). *Global Biogeochemical Cycles*, 18.

KEY, R. M., OLSEN, A., VAN HEUVEN, S., LAUVSET, S. K., VELO, A., LIN, X., SCHIRNICK, C., KOZYR, A., TANHUA, T., HOPPEMA, M., JUTTERSTRÖM, S., STEINFELDT, R., JEANSSON, E., ISHII, M., PEREZ, F. F. AND SUZUKI, T. (2015): Global Ocean Data Analysis Project, Version 2 (GLODAPv2), [Miscellaneous] doi: 10.3334/CDIAC/OTG. NDP093_GLODAPv2

KHATIWALA, S., TANHUA, T., MIKALOFF FLETCHER, S., GERBER, M., DONEY, S. C., GRAVEN, H. D., GRUBER, N., MCKINLEY, G. A., MURATA, A., RÍOS, A. F. & SABINE, C. L. 2013. Global ocean storage of anthropogenic carbon. *Biogeosciences*, 10**,** 2169-2191.

KHOO, K. H., RAMETTE, R. W., CULBERSON, C. H. & BATES, R. G. 1977. Determination of hydrogen ion concentrations in seawater from 5 to 40.degree.C: standard potentials at salinities from 20 to 45%. *Analytical Chemistry*, 49**,** 29-34.

LANDSCHÜTZER, P., GRUBER, N., HAUMANN, F. A., RÖDENBECK, C., BAKKER, D. C. E., VAN HEUVEN, S., HOPPEMA, M., METZL, N., SWEENEY, C., TAKAHASHI, T., TILBROOK, B. & WANNINKHOF, R. 2015. The reinvigoration of the Southern Ocean carbon sink. *Science*, 349**,** 1221-1224.

LE QUÉRÉ, C., ANDREW, R. M., CANADELL, J. G., SITCH, S., KORSBAKKEN, J. I., PETERS, G. P., MANNING, A. C., BODEN, T. A., TANS, P. P., HOUGHTON, R. A., KEELING, R. F., ALIN, S., ANDREWS, O. D., ANTHONI, P., BARBERO, L., BOPP, L., CHEVALLIER, F., CHINI, L. P., CIAIS, P., CURRIE, K., DELIRE, C., DONEY, S. C., FRIEDLINGSTEIN, P., GKRITZALIS, T., HARRIS, I., HAUCK, J., HAVERD, V., HOPPEMA, M., KLEIN GOLDEWIJK, K., JAIN, A. K., KATO, E., KÖRTZINGER, A., LANDSCHÜTZER, P., LEFÈVRE, N., LENTON, A., LIENERT, S., LOMBARDOZZI, D., MELTON, J. R., METZL, N., MILLERO, F., MONTEIRO, P. M. S., MUNRO, D. R., NABEL, J. E. M. S., NAKAOKA, S. I., O'BRIEN, K., OLSEN, A., OMAR, A. M., ONO, T., PIERROT, D., POULTER, B., RÖDENBECK, C., SALISBURY, J., SCHUSTER, U., SCHWINGER, J., SÉFÉRIAN, R., SKJELVAN, I., STOCKER, B. D., SUTTON, A. J., TAKAHASHI, T., TIAN, H., TILBROOK, B., VAN DER LAAN-LUIJKX, I. T., VAN DER WERF, G. R., VIOVY, N., WALKER, A. P., WILTSHIRE, A. J. & ZAEHLE, S. 2016. Global Carbon Budget 2016. *Earth Syst. Sci. Data*, 8**,** 605-649.

LE QUÉRÉ, C., ANDREW, R. M., FRIEDLINGSTEIN, P., SITCH, S., PONGRATZ, J., MANNING, A. C., KORSBAKKEN, J. I., PETERS, G. P., CANADELL, J. G., JACKSON, R. B., BODEN, T. A., TANS, P. P., ANDREWS, O. D., ARORA, V. K., BAKKER, D. C. E., BARBERO, L., BECKER, M., BETTS, R. A., BOPP, L., CHEVALLIER, F., CHINI, L. P., CIAIS, P., COSCA, C. E., CROSS, J., CURRIE, K., GASSER, T., HARRIS, I., HAUCK, J., HAVERD, V., HOUGHTON, R. A., HUNT, C. W., HURTT, G., ILYINA, T., JAIN, A. K., KATO, E., KAUTZ, M., KEELING, R. F., KLEIN GOLDEWIJK, K., KÖRTZINGER, A., LANDSCHÜTZER, P., LEFÈVRE, N., LENTON, A., LIENERT, S., LIMA, I., LOMBARDOZZI, D., METZL, N., MILLERO, F., MONTEIRO, P. M. S., MUNRO, D. R., NABEL, J. E. M. S., NAKAOKA, S.-I., NOJIRI, Y., PADIN, X. A., PEREGON, A., PFEIL, B., PIERROT, D., POULTER, B., REHDER, G., REIMER, J., RÖDENBECK, C., SCHWINGER,

J., SÉFÉRIAN, R., SKJELVAN, I., STOCKER, B. D., TIAN, H., TILBROOK, B., TUBIELLO, F. N., VAN DER LAAN-LUIJKX, I. T., VAN DER WERF, G. R., VAN HEUVEN, S., VIOVY, N., VUICHARD, N., WALKER, A. P., WATSON, A. J., WILTSHIRE, A. J., ZAEHLE, S. & ZHU, D. 2018. Global Carbon Budget 2017. *Earth System Science Data,* 10**,** 405-448.

LE QUÉRÉ, C., RÖDENBECK, C., BUITENHUIS, E. T., CONWAY, T. J., LANGENFELDS, R., GOMEZ, A., LABUSCHAGNE, C., RAMONET, M., NAKAZAWA, T., METZL, N., GILLETT, N. & HEIMANN, M. 2007. Saturation of the Southern Ocean CO2 Sink Due to Recent Climate Change. *Science,* 316**,** 1735-1738.

LEE, K., KIM, T.-W., BYRNE, R. H., MILLERO, F. J., FEELY, R. A. & LIU, Y.-M. 2010. The universal ratio of boron to chlorinity for the North Pacific and North Atlantic oceans. *Geochimica et Cosmochimica Acta,* 74**,** 1801-1811.

LEE, K., MILLERO, F. J. & CAMPBELL, D. M. 1996. The reliability of the thermodynamic constants for the dissociation of carbonic acid in seawater. *Marine Chemistry,* 55**,** 233-245.

LEE, K., TONG, L. T., MILLERO, F. J., SABINE, C. L., DICKSON, A. G., GOYET, C., PARK, G.-H., WANNINKHOF, R., FEELY, R. A. & KEY, R. M. 2006. Global relationships of total alkalinity with salinity and temperature in surface waters of the world's oceans. *Geophysical Research Letters,* 33.

LEI, J. & XIAN-KUN, L. 1997. Study on determination of dic in seawater by coulometric method. *Chinese Journal of Oceanology and Limnology,* 15**,** 357-362.

LIU, X., WANG, Z. A., BYRNE, R. H., KALTENBACHER, E. A. & BERNSTEIN, R. E. 2006. Spectrophotometric Measurements of pH in-Situ: Laboratory and Field Evaluations of Instrumental Performance. *Environmental Science & Technology,* 40**,** 5036-5044.

LOEWENTHAL, R. E. & VAN ROOYEN MARAIS, G. 1976. *Carbonate Chemistry of Aquatic Systems: High salinity waters,* Ann Arbor Science.

LUEKER, T. J., DICKSON, A. G. & KEELING, C. D. 2000. Ocean pCO_2 calculated from dissolved inorganic carbon, alkalinity, and equations for K1 and K2: validation based on laboratory measurements of CO2 in gas and seawater at equilibrium. *Marine Chemistry,* 70**,** 105-119.

MAJKUT, J. D., SARMIENTO, J. L. & RODGERS, K. B. 2014. A growing oceanic carbon uptake: Results from an inversion study of surface pCO_2 data. *Global Biogeochemical Cycles,* 28**,** 335-351.

MARTZ, T. R., CONNERY, J. G. & JOHNSON, K. S. 2010. Testing the Honeywell Durafet® for seawater pH applications. *Limnology and Oceanography: Methods,* 8**,** 172-184.

MATEAR, R. J., HIRST, A. C. & MCNEIL, B. I. 2000. Changes in dissolved oxygen in the Southern Ocean with climate change. *Geochemistry, Geophysics, Geosystems,* 1.

MCNEIL, B. I. M., R.J. 2013. The non-steady state oceanic CO2 signal: its importance, magnitude and a novel way to detect it. *Biogeosciences,* 10**,** 2219-2228.

MEHRBACH, C., CULBERSON, C. H., HAWLEY, J. E. & PYTKOWICX, R. M. 1973. MEASUREMENT OF THE APPARENT DISSOCIATION CONSTANTS OF CARBONIC ACID IN SEAWATER AT ATMOSPHERIC PRESSURE1. *Limnology and Oceanography,* 18**,** 897-907.

METZL, N., BRUNET, C., JABAUD-JAN, A., POISSON, A. & SCHAUER, B. 2006. Summer and winter air–sea CO2 fluxes in the Southern Ocean. *Deep Sea Research Part I: Oceanographic Research Papers,* 53**,** 1548-1563.

MILLERO, F., PIERROT, D., LEE, K., WANNINKHOF, R., FEELY, R., CHRIS, S., KEY, R. & TAKAHASHI, T. 2002. *Dissociation constants for carbonic acid determined from field measurements*.

MILLERO, F. J., GRAHAM, T. B., HUANG, F., BUSTOS-SERRANO, H. & PIERROT, D. 2006. Dissociation constants of carbonic acid in seawater as a function of salinity and temperature. *Marine Chemistry,* 100**,** 80-94.

MILLERO, F. J., LEE, K. & ROCHE, M. 1998. Distribution of alkalinity in the surface waters of the major oceans. *Marine Chemistry,* 60**,** 111-130.

MINTROP, L. 2010. VINDTA: Manual for Versions 3S and 3C. Kiel, Germany.

MONTEIRO, P. M. S., GREGOR, L., LÉVY, M., MAENNER, S., SABINE, C. L. & SWART, S. 2015. Intraseasonal variability linked to sampling alias in air-sea CO2 fluxes in the Southern Ocean. *Geophysical Research Letters,* 42**,** 8507-8514.

MUNRO, D. R., LOVENDUSKI, N. S., TAKAHASHI, T., STEPHENS, B. B., NEWBERGER, T. & SWEENEY, C. 2015. Recent evidence for a strengthening CO2 sink in the Southern Ocean from carbonate system measurements in the Drake Passage (2002–2015). *Geophysical Research Letters,* 42**,** 7623-7630.

OLSEN, A., R. M. KEY, S. VAN HEUVEN, S. K. LAUVSET, A. VELO, X. LIN, C. SCHIRNICK, A. KOZYR, T. TANHUA, M. HOPPEMA, S. JUTTERSTRÖM, R. STEINFELDT, E. JEANSSON, M. ISHII, F. F. PÉREZ AND T. SUZUKI. The Global Ocean Data Analysis Project version 2 (GLODAPv2) – an internally consistent data product for the world ocean, *Earth Syst. Sci. Data*, 8, 297–323, 2016, doi:10.5194/essd-8-297-2016.

OLSEN, A.; KEY, R. M.; LAUVSET, S. K.; KOZYR, A.; TANHUA, T.; HOPPEMA, M.; ISHII, M.; JEANSSON, E.; VAN HEUVEN, S.; JUTTERSTRÖM, S.; SCHIRNICK, C.; STEINFELDT, R.; SUZUKI, T.; LIN, X.; VELO, A.; PÉREZ, F. F. (2017). Global Ocean Data Analysis Project, Version 2 (GLODAPv2) (NCEI Accession 0162565). Version 1.1. NOAA National Centers for Environmental Information. Dataset. doi:10.7289/V5KW5D97PEREZ, F. F. & FRAGA, F. 1987. A precise and rapid analytical procedure for alkalinity determination. *Marine Chemistry,* 21**,** 169-182.

PIERROT, D., NEILL, C., SULLIVAN, K., CASTLE, R., WANNINKHOF, R., NAIGUR, H., JOHANNESSEN, T., OLSEN, A., FEELY, R. & E. COSCA, C. 2009. *Recommendations for autonomous underway pCO_2 measuring systems and data-reduction routines*.

RILEY, J. P. 1976. GRASSHOFF, K. [ED.] 1976. Methods of seawater analysis. Verlag Chemie, Weinheim and New York, xv + 317 p. $43.60. *Limnology and Oceanography,* 22**,** 1103-1103.

RINTOUL, S., W. HUGHES, C. & OLBERS, D. 2001. *The Antarctic Circumpolar Current system*.

RISER, S., C., RUPAN, R., SWIFT, D., D., JOHNSON, C., SAKAMOTO, C., M. & TALLEY, L., D. 2017. *SOCCOM BGC Floats: Deployment and Cleaning Procedures* [Online]. Available: https://soccom.princeton.edu/content/manuals [Accessed 2017].

ROBBINS, L. L., HANSEN, M. E., KLEYPAS, J. A. & MEYLAN, S. C. 2010. CO2calc: A User-Friendly Seawater Carbon Calculator for Windows, Mac OS X, and iOS (iPhone). *Open-File Report*. Reston, VA.

RUSSEL, J., SARMIENTO, J., CULLEN, H., HOTINSKI, R., JOHNSON, K., RISER, S. & TALLEY, L. 2014. *The Southern Ocean Carbon and Climate Observations and Modeling Program (SOCCOM)* [Online]. Ocean Carbon and Biogeochemistry News. Available: https://web.whoi.edu/ocb/wp-content/uploads/sites/43/2016/12/OCB_NEWS_FALL14.pdf [Accessed March 2018].

SABINE, C. & FEELY, R. 2007. The oceanic sink for carbon dioxide. *Greenhouse Gas Sinks***,** 31-49.

SABINE, C. L., FEELY, R. A., GRUBER, N., KEY, R. M., LEE, K., BULLISTER, J. L., WANNINKHOF, R., WONG, C. S., WALLACE, D. W. R., TILBROOK, B., MILLERO, F. J., PENG, T.-H., KOZYR, A., ONO, T. & RIOS, A. F. 2004. The Oceanic Sink for Anthropogenic CO2. *Science,* 305**,** 367.

SARMIENTO, J. L. & GRUBER, N. 2013. *Ocean Biogeochemical Dynamics*, Princeton University Press.

SCIENTIFIC, S.-B. 2018. SeaFET Sensor User Manual. USA: Sea-Bird Electronics.

SEIDEL, M. P., DEGRANDPRE, M. D. & DICKSON, A. G. 2008. A sensor for in situ indicator-based measurements of seawater pH. *Marine Chemistry,* 109**,** 18-28.

SKOOG, D. A. 2004. *Fundamentals of Analytical Chemistry*, Thomson-Brooks/Cole.

SPEER, K., RINTOUL, S. R. & SLOYAN, B. 2000. The Diabatic Deacon Cell. *Journal of Physical Oceanography,* 30**,** 3212-3222.

STRICKLAND, J. D. & PARSONS, T. R. 1977. *A Practical Handbook of Seawater Analysis*, Min. of Supply and Services.

SUTTON, A., SABINE, C. L., MAENNER-JONES, S., LAWRENCE-SLAVAS, N., MEINIG, C., FEELY, R. A., MATHIS, J. T., MUSIELEWICZ, S., BOTT, R., MCLAIN, P. D., FOUGHT, H. J. & KOZYR, A. 2014. A high-frequency atmospheric and seawater pCO_2 data set from 14 open ocean sites using a moored autonomous system. *Earth Syst. Sci. Data,* 6**,** 353-366.

SUZUKI, T., M. ISHII, M. AOYAMA, J. R. CHRISTIAN, K. ENYO, T. KAWANO, R. M. KEY, N. KOSUGI, , A. KOZYR, L. A. M., A. MURATA, T. NAKANO, T. ONO, T. SAINO, K. SASAKI, D. SASANO, Y. TAKATANI, & SABINE, M. W. A. C. L. 2013. PACIFICA Data Synthesis Project.

TAKESHITA, Y., JOHNSON, K. S., MARTZ, T. R., PLANT, J. N. & SARMIENTO, J. L. 2018. Assessment of Autonomous pH Measurements for Determining Surface Seawater Partial Pressure of CO2. *Journal of Geophysical Research: Oceans,* 123**,** 4003-4013.

TALLEY, L. D. 2011. *Descriptive Physical Oceanography: An Introduction,* Elsevier Science.

TANS, P. & KEELING, R. 2018. *Trends in Atmospheric Carbon Dioxide* [Online]. NOAA/ESRL. Available: www.esrl.noaa.gov/gmd/ccgg/trends/ [Accessed April 2018].

WALLACE, J. M. & HOBBS, P. V. 2006. *Atmospheric Science: An Introductory Survey*, Elsevier Science.

WANNINKHOF, R. 1992. Relationship between wind speed and gas exchange over the ocean. *Journal of Geophysical Research: Oceans,* 97**,** 7373-7382.

WANNINKHOF, R., JOHNSON, K., WILLIAMS, N., SARMIENTO, J., RISER, S., BRIGGS, E., BUSHINSKY, S., CARTER, B., DICKSON, A., FEELY, R., GRAY, A., JURANEK, L., KEY, R., TALLEY, L., RUSSELL, J. & VERDY, A. 2016. *An evaluation of pH and NO3 sensor data from SOCCOM floats and their utilization to develop ocean inorganic carbon products: A summary of discussions and recommendations of the Carbon Working Group (CWG) of the Southern Ocean Carbon and Climate Observations and Modeling project (SOCCOM)*.

WATANABE, A., KAYANNE, H., NOZAKI, K., KATO, K., NEGISHI, A., KUDO, S., KIMOTO, H., TSUDA, M. & DICKSON, A. G. 2004. A rapid, precise potentiometric determination of total alkalinity in seawater by a newly developed flow-through analyzer designed for coastal regions. *Marine Chemistry,* 85**,** 75-87.

WILLIAMS, N., JURANEK, L., FEELY, R., S. JOHNSON, K., L. SARMIENTO, J., TALLEY, L., DICKSON, A., GRAY, A., WANNINKHOF, R., RUSSELL, J., C. RISER, S. & TAKESHITA, Y. 2017. *Calculating surface ocean pCO_2 from biogeochemical Argo floats equipped with pH: An uncertainty analysis*.

WILLIAMS, N. L., JURANEK, L. W., JOHNSON, K. S., FEELY, R. A., RISER, S. C., TALLEY, L. D., RUSSELL, J. L., SARMIENTO, J. L. & WANNINKHOF, R. 2016. Empirical algorithms to estimate water column pH in the Southern Ocean. *Geophysical Research Letters,* 43**,** 3415-3422.

WOLF-GLADROW, D. A., ZEEBE, R. E., KLAAS, C., KÖRTZINGER, A. & DICKSON, A. G. 2007. Total alkalinity: The explicit conservative expression and its application to biogeochemical processes. *Marine Chemistry,* 106**,** 287-300.

XIE, H.-B., ZHOU, Y., ZHANG, Y. & JOHNSON, J. K. 2010. Reaction Mechanism of Monoethanolamine with CO2 in Aqueous Solution from Molecular Modeling. *The Journal of Physical Chemistry A,* 114**,** 11844-11852.

ZEEBE, R. E. & WOLF-GLADROW, D. A. 2001. *CO2 in Seawater: Equilibrium, Kinetics, Isotopes*, Elsevier.

APPENDIX A

A.1 The Gran Method

The Gran method is used to accurately determine the endpoint of a potentiometric titration by mathematically manipulating the data close to the endpoint region. While derivative plots are a close estimate, they are not as accurate as the Gran method. The deviation in accuracy occurs due to the erratic electrode response close to the endpoint, and the low receptivity of the buffer close to the endpoint. The Gran method mathematically transforms a titration curve into a straight line which intersects the x-axis at the equivalence point, or rather, the endpoint.

In order to calculate the endpoint by means of the Gran method, it is necessary to use the activity coefficient of hydrogen since the pH_T electrode measures the activity of the hydrogen ions in solution. Consider the potentiometric titration of a weak acid with a strong base, such as carbonic acid with sodium hydroxide; the corrected plot to yield a straight line is as follows: (Harris, 2010)

The weak acid will completely dissociate upon titration with a strong base:

$$HA \rightleftharpoons H^+ + A^-$$

The activity of each of the hydrogen species is related to the pH_T as follows:

$$a_{H^+} = [H^+]\gamma_{H^+} = 10^{-pH}$$

At equilibrium:

$$K_a = \frac{[H^+]\gamma_{H^+}[A^-]\gamma_{A^-}}{[HA]\gamma_{HA}}$$

It is assumed that at any point before reaching the endpoint, that 1 mole of strong base (such as NaOH) will convert one mole of HA to one mole of A^-. If a known volume of acid (V_a) with concentration C_a is titrated with a volume of base (V_b) with concentration C_b, then:

$$[A^-] = \frac{moles\ OH^-delivered}{total\ volume} = \frac{V_bC_b}{V_b + V_a}$$

$$[HA] = \frac{initial\ moles\ HA - moles\ OH^-}{total\ volume} = \frac{V_aC_a - V_bC_b}{V_b + V_a}$$

Substituting the values of A^- and HA into the equilibrium expression:

$$K_a = \frac{[H^+]\gamma_{H^+}\, V_b C_b\, \gamma_A}{(V_a C_a - V_b C_b)\gamma_{HA}}$$

Rearranging the above formula:

$$10^{-pH} V_b = \frac{\gamma_{HA}}{\gamma_{A^-}} \left(\frac{V_a C_a - V_b C_b}{C_b} \right) K_a$$

The term in parentheses equates to the endpoint volume minus the volume of base delivered:

$$\left(\frac{V_a C_a - V_b C_b}{C_b} \right) = \frac{V_a C_a}{C_b} - V_b = V_e - V_b$$

Thus, the Gran plot equation simplifies to:

$$10^{-pH} V_b = \frac{\gamma_{HA}}{\gamma_{A^-}} (V_e - V_b) K_a$$

The Gran plot is attained from a graph of $V_b 10^{-pH_T}$ against V_b. For a constant ratio of γ_{HA}/γ_{A^-} the plot will yield a straight line intercepting the x-axis at V_e and the slope $-K_a \gamma_{HA}/\gamma_{A^-}$. In order to obtain V_e, the curve plotted must be extrapolated to zero. (Harris, 2010)

Any curvature arising on the plot as the curve approaches and passes the endpoint, can be attributed to the changing ionic strength of the solution and the assumption that 1 mole of base will completely dissociate 1 mole of acid into 1 mole equivalents of its constituent species. The curvature at this point in the curve is disregarded, as 10-20 % of the data ($0.8V_e$ -$0.9V_e$) before the endpoint, V_e, is sufficient to produce to a straight line, provided that the ionic strength of the solution is kept constant. (Harris, 2010).

A.2.1 pCO_2 derived from pH_T and TA (Zeebe and Wolf-Gladrow, 2001)

$$pH = -\log[H^+]$$

$$TA = 2[{CO_3}^{2-}] + [HCO_3^-] + [B(OH)_4^-] + [OH^-] - [H^+]$$

$$CA = TA - [B(OH)_4^-] - [OH^-] + [H^+]$$

$$= 2[{CO_3}^{2-}] + [HCO_3^-]$$

Solve for $[CO_3^{2-}]$ and $[HCO_3^-]$ from the equilibrium equation:

$$HCO_3^- \overset{K_2}{\leftrightarrow} {CO_3}^{2-} + H^+$$

$$\therefore [HCO_3^-] = \frac{[{CO_3}^{2-}][H^+]}{K_2}$$

Substitute K_2 into CA:

$$CA = \frac{[{CO_3}^{2-}][H^+]}{K_2} + 2[{CO_3}^{2-}]$$

$$= [{CO_3}^{2-}]\left(\frac{[H^+]}{K_2} + 2\right)$$

$$\therefore [{CO_3}^{2-}] = \frac{\left(\frac{[H^+]}{K_2} + 2\right)}{CA}$$

Solve for CO_2 from the equilibrium equation:

$$CO_{2(aq)} + H_2O \overset{K_1}{\leftrightarrow} HCO_3^- + H^+$$

$$K_1 = \frac{[HCO_3^-][H^+]}{[CO_{2(aq)}]}$$

$$\therefore [CO_{2(aq)}] = \frac{[HCO_3^-][H^+]}{K_1}$$

$$\therefore DIC = \left[CO_{2(aq)}\right] + [HCO_3{}^-] + \left[CO_3{}^{2-}\right]$$

Solve for $CO_{2\,(g)}$ i.e. pCO_2 from the equilibrium equation:

$$CO_{2(g)} \overset{K_0}{\leftrightarrow} CO_{2(aq)}$$

$$\therefore \left[CO_{2(g)}\right] = \frac{[CO_{2(aq)}]}{K_0}$$

A.2.2 pH_T derived from DIC and TA (Zeebe and Wolf-Gladrow, 2001)

$h = [H^+]$ and $s = [CO_2]$:

$$DIC = s\left(1 + \frac{K_1}{h} + \frac{K_1K_2}{h^2}\right)$$

$$\therefore s = \frac{DIC}{\left(1 + \frac{K_1}{h} + \frac{K_1K_2}{h^2}\right)}$$

and

$$TA = s\left(\frac{K_1}{h} + \frac{2K_1K_2}{h^2}\right) + \frac{B_TK_B}{K_B + h} + \frac{K_w}{h} - h$$

$$\therefore s = \frac{TA - \frac{B_TK_B}{K_B + h} - \frac{K_w}{h} + h}{\left(\frac{K_1}{h} + \frac{2K_1K_2}{h^2}\right)}$$

Equating s:

$$DIC\left(\frac{K_1}{h} + \frac{2K_1K_2}{h^2}\right) = \left[TA - \frac{B_TK_B}{K_B + h} - \frac{K_w}{h} + h\right]\left(1 + \frac{K_1}{h} + \frac{K_1K_2}{h^2}\right)$$

$$DIC\left(\frac{hK_1 + 2K_1K_2}{h^2}\right)$$

$$= \left[\frac{hTA(K_B + h) - hB_TK_B - K_w(K_B + h) + h^2(K_B + h)}{h(K_B + h)}\right]\left(\frac{h^2 + hK_1 + K_1K_2}{h^2}\right)$$

Multiply through by $h^3(K_B+h)$:

LHS:

$$DIC \cdot h^{\cancel{3}}(K_B + h)\left(\frac{hK_1 + 2K_1K_2}{h^{\cancel{2}}}\right) = DIC \cdot (K_B + h)(h^2K_1 + h2K_1K_2)$$

$$= h^2K_1K_BDIC + h2K_1K_2K_BDIC + h^3K_1DIC + h^2 2K_1K_2DIC$$

RHS:

$$\cancel{h^3(K_B + h)}\left[\frac{hTA(K_B + h) - hB_TK_B - K_w(K_B + h) + h^2(K_B + h)}{\cancel{h(K_B + h)}}\right]\left(\frac{h^2 + hK_1 + K_1K_2}{h^{\cancel{2}}}\right)$$

$$= [hTA(K_B + h) - hB_TK_B - K_w(K_B + h) + h^2(K_B + h)](h^2 + hK_1 + K_1K_2)$$

$$= [hTAK_B + h^2TA - hB_TK_B - K_wK_B - hK_w + h^2K_B + h^3](h^2 + hK_1 + K_1K_2)$$

$$\begin{aligned} = {} & h^3TAK_B + h^4TA - h^3B_TK_B - h^2K_wK_B - h^3K_w + h^4K_B + h^5 + h^2K_1TAK_B + h^3K_1TA \\ & - h^2K_1B_TK_B - hK_1K_wK_B - h^2K_1K_w + h^3K_1K_B + h^4K_1 + hK_1K_2TAK_B \\ & + h^2K_1K_2TA - hK_1K_2B_TK_B - K_1K_2K_wK_B - hK_1K_2K_w + h^2K_1K_2K_B \\ & + h^3K_1K_2 \end{aligned}$$

$$\begin{aligned} = {} & h^5 + h^4(TA + K_B + K_1) + h^3(TAK_B - B_TK_B - K_w + K_1TA + K_1K_B + K_1K_2) \\ & + h^2(-K_wK_B + K_1TAK_B - K_1B_TK_B - K_1K_w + K_1K_2TA + K_1K_2K_B) \\ & + h(-K_1K_wK_B + K_1K_2TAK_B - K_1K_2B_TK_B - K_1K_2K_w) - K_1K_2K_wK_B \end{aligned}$$

$$\therefore LHS + RHS = 0$$

$$\begin{aligned} & h^5 + h^4(TA + K_B + K_1) + h^3(TAK_B - B_TK_B - K_w + K_1TA + K_1K_B + K_1K_2 - K_1DIC) \\ & + h^2(-K_wK_B + K_1TAK_B - K_1B_TK_B - K_1K_w + K_1K_2TA + K_1K_2K_B \\ & - K_1K_BDIC - 2K_1K_2DIC) \\ & + h(-K_1K_wK_B + K_1K_2TAK_B - K_1K_2B_TK_B - K_1K_2K_w - 2K_1K_2K_BDIC) \\ & - K_1K_2K_wK_B = 0 \end{aligned}$$

$$\begin{aligned} \therefore h^5 = {} & K_1K_2K_wK_B - h^4(TA + K_B + K_1) \\ & - h^3(TAK_B - B_TK_B - K_w + K_1TA + K_1K_B + K_1K_2 - K_1DIC) \\ & - h^2(-K_wK_B + K_1TAK_B - K_1B_TK_B - K_1K_w + K_1K_2TA + K_1K_2K_B \\ & - K_1K_BDIC - 2K_1K_2DIC) \\ & - h(-K_1K_wK_B + K_1K_2TAK_B - K_1K_2B_TK_B - K_1K_2K_w - 2K_1K_2K_BDIC) \end{aligned}$$

5th order polynomial of h yields one positive root and four negative roots. Once h has been determined, s can be solved and subsequently each of the carbonate variables, as well as pH_T = -log(h).

A.2.1 Derivation of TA_{ec} (Wolf-Gladrow et al., 2007)

The derivation of TAec pertains to equations 19, 20 and 21 in Section 1.4, Pages 23 – 25.

$$\begin{aligned} TA = {} & [HCO_3^-] + 2[CO_3^{2-}] + [B(OH)_4^-] + [OH^-] + [HPO_4^{2-}] + 2[PO_4^{3-}] \\ & + [H_3SiO_4^-] + [NH_3] + [HS^-] + x - [H^+]_F - [HSO_4^-] \\ & - [HF] - [H_3PO_4] - [HNO_2] + x \end{aligned} \tag{19}$$

$$\sum_i q_i[C_i] = 0 \tag{20}$$

$$\begin{aligned} = {} & [Na^+] + 2\,[Mg^{2+}] + 2[Ca^{2+}] + [K^+] + 2[Sr^{2+}] + x + [NH_4^+] + [H^+] + x \\ & - [Cl^-] - 2[SO_4^{2-}] - [Br^-] - [NO_3^-] - [NO_2^-] - x \\ & - [HCO_3^-] - 2[CO_3^{2-}] - [B(OH)_4^-] - [OH^-] - [HS^-] \\ & - [H_3SiO_4^-] - [HSO_4^-] - [F^-] - [H_2PO_4^-] - 2[HPO_4^{2-}] \\ & - 3[PO_4^{3-}] \end{aligned}$$

where x represents unidentified species of the acid-base system in seawater.

Dickson's expression for TA (Eq. 19), with the addition of HNO_2, is added to both sides of equation 20 such that the right hand side is equal to Eq 19, and the left hand side of the equation simplifies to TAec (Eq. 21):

$$\therefore \sum_i q_i[C_i] + TA = TA$$

$$\therefore \sum_i q_i[C_i] + TA$$

$$\begin{aligned} = {} & [Na^+] + 2\,[Mg^{2+}] + 2[Ca^{2+}] + [K^+] + 2[Sr^{2+}] + \cdots + [NH_4^+] \cancel{+ [H^+]} + \cdots - [Cl^-] \\ & - 2[SO_4^{2-}] - [Br^-] - [NO_3^-] - [NO_2^-] - \cdots \cancel{- [HCO_3^-] - 2[CO_3^{2-}]} \\ & \cancel{- [B(OH)_4^-] - [OH^-] - [HS^-] - [H_3SiO_4^-]} - [HSO_4^-] - [F^-] \\ & - [H_2PO_4^-] - \cancel{2}[HPO_4^{2-}] - \cancel{3}[PO_4^{3-}] + \cancel{([HCO_3^-] + 2[CO_3^{2-}]} \\ & \cancel{+ [B(OH)_4^-] + [OH^-] + [HPO_4^{2-}] + 2[PO_4^{3-}] + [H_3SiO_4^-]} + [NH_3] \\ & + \cancel{[HS^-] + \cdots - [H^+]_F} - [HSO_4^-] - [HF] - [H_3PO_4] - [HNO_2] + \cdots) \\ = {} & [Na^+] + 2\,[Mg^{2+}] + 2[Ca^{2+}] + [K^+] + 2[Sr^{2+}] + \cdots + [NH_4^+] + + \cdots - [Cl^-] \\ & - 2[SO_4^{2-}] - [Br^-] - [NO_3^-] - [NO_2^-] - \cdots - [HSO_4^-] - [F^-] \\ & - [H_2PO_4^-] - [HPO_4^{2-}] - [PO_4^{3-}] \\ = {} & TA_{ec} \end{aligned}$$

Therefore:

$$\begin{aligned} TA_{ec} = {} & [Na^+] + 2\,[Mg^{2+}] + 2[Ca^{2+}] + [K^+] + 2[Sr^{2+}] + \cdots + [NH_4{}^+] \\ & + + \cdots - [Cl^-] - 2\left[SO_4{}^{2-}\right] - [Br^-] - [NO_3{}^-] - [NO_2{}^-] - \cdots \\ & - [HSO_4{}^-] - [F^-] - [H_2PO_4{}^-] - \left[HPO_4{}^{2-}\right] - \left[PO_4{}^{3-}\right] \\ = {} & [Na^+] + 2[Mg^{2+}] + [K^+] + 2[Sr^{2+}] + \cdots + [NH_4{}^+] + \cdots - [Cl^-] \\ & - [Br^-] - [NO_3{}^-] - \cdots TPO_4 + TNH_3 - 2TSO_4 - THF \\ & - THNO_2 \end{aligned} \tag{20}$$

where

$$TPO_4 = [H_3PO_4] + [H_2PO_4{}^-] + \left[HPO_4{}^{2-}\right] + \left[PO_4{}^{3-}\right]$$

$$TNH_3 = [NH_4{}^+] + [NH_3]$$

$$TSO_4 = \left[SO_4{}^{2-}\right] + [HSO_4{}^-]$$

$$THF = [F^-] + [HF]$$

$$THNO_2 = [NO_2{}^-] + [HNO_2]$$

Ellipses represent unidentified acid-base species in seawater.

APPENDIX B

B.1 SOCCOM observational data

SOCCOM float observations (Figures B1 – B10) showed a decrease in temperature ranging from ~ 22 °C in the STZ (Float 9313) down to ~ -2 °C in the MIZ (Float 9096). The highest sea surface temperatures were observed in the STZ and decreased moving south into the higher latitudes (Figure B2). The STZ had an average temperature of 17.29 ± 2.041 °C, which decreased to 11.10 ± 2.506 °C in the SAZ, 4.529 ± 0.666 °C in the PFZ, 0.542 ± 0.909 °C in the PUZ, and -0.089 ± 1.190 °C in the MIZ (Table 4.4). The lowest temperatures were observed in the MIZ, closest to the ice edge.

Figure B2 shows the temporal distribution of the sea surface temperature measurements from Dec 2014 to Nov 2017. Autumn/winter months in the southern hemisphere are demarcated in grey from May to August of each year. Float 9313 situated in the SAZ showed an upward trend in sea surface temperature over the time period moving from the SAZ to the STZ, with maximum temperatures between Jan – Feb 2015, Apr 2016, Dec 2016 – Jan 2017 and Nov 2017. Minimum temperatures in the SAZ/STZ region occur between Jul 2017, Jun 2016 and Jul – Aug 2017. Float 9260 situated in the PFZ showed little variation in observed temperatures, with minimum temperatures seen from Aug – Sep 2015. The PUZ/MIZ showed increasing temperatures during Feb – Apr 2015, Feb – Mar 2016, Jan – Apr 2017, and Dec 2017 – Apr 2018. Decreasing temperatures were observed in the PUZ/MIZ from May – Jun 2015, May – Dec 2016 and May – Nov 2017. The MIZ was characterised by warmer sea surface temperatures in the winter months as ice coverage inhibits the exchange of heat between the ocean and the atmosphere, and slightly cooler temperatures in the summer months coupled with the melting of sea-ice in the region.

Coinciding with the decrease in temperature, was a freshening of the sea surface salinity from more saline waters in the STZ, to relatively fresher waters in the MIZ. (Figure B3). The STZ had an average salinity of 35.40 ± 0.227 PSU, and decreased to 34.35 ± 0.450 PSU in the SAZ. The PFZ had the lowest average salinity at 33.78 ± 0.075 PSU, which increased to 33.86 ± 0.161 PSU in the PUZ and 33.81 ± 0.0113 PSU in the MIZ.

The temporal distribution of sea surface salinity in each region (Figure B4) showed an increasing trend in salinity as Float 9313 moved from the SAZ to the STZ, little variation in salinity in the PFZ and a varying salinity in the PUZ/MIZ. Salinity is observed to increase

from May – Jun 2015, Apr – Nov 2016, and Jun – Sep 2017 in the PUZ/MIZ, which coincide with the winter-time months in the southern hemisphere. The surface waters of the MIZ are seen to be less saline at the onset of the winter months, and increased leading up to the summer season. This coincides with brine rejection from sea-ice formation i.e. waters grow more saline as ice forms, and fresher as the ice melts throughout the summer.

In situ pH_T measurements at the sea surface were observed to range between 7.1 and 8.1 on the pH_T scale (Figure B5). The lower end of the pH_T readings, indicating a neutral pH_T are attributed to sea-ice thaw at the sensor interface in the PUZ and MIZ. The largest variation in pH_T was observed in the MIZ, as pH_T drops to < 8.0. pH_T observations showed a decrease in pH_T as the float drifted from the SAZ in 2014 (8.067 ±0.021) to the STZ in 2016 – 2017 (8.027 ± 0.029). The average pH_T decreased from the PFZ at 8.026 ± 0.028, to 7.973 ± 0.181 in the PUZ, and to 7.927 ± 0.182 in the MIZ.

Surface ocean pH_T measurements from the STZ to the MIZ show a similar seasonal trend (Figure B6) through time. The MIZ, closest to the ice edge had the most variation in pH_T measurements. The seasonal trend of pH_T in the low latitudes (STZ and SAZ) indicated a high during the summer months, and lows during the winter months. This was in contrast to the seasonal trend in the high latitudes (PFZ and MIZ), where highs were observed in the winter months and lows in the summer months, which coincides with the trend observed in salinity. It is expected that the melting of sea-ice freshens the surface waters of the MIZ in summer thereby lowering pH_T. Conversely, the winter-time exchange of CO_2 between upwelled deep water and the atmosphere are seen to increase pH_T in the surface ocean. Anomalous observations of pH_T that appeared to be unreasonably low are likely due to sea-ice thaw at the sensor interface, and are not considered in this study.

The sea surface average float-based measurements for each zone are summarised in Table B1.

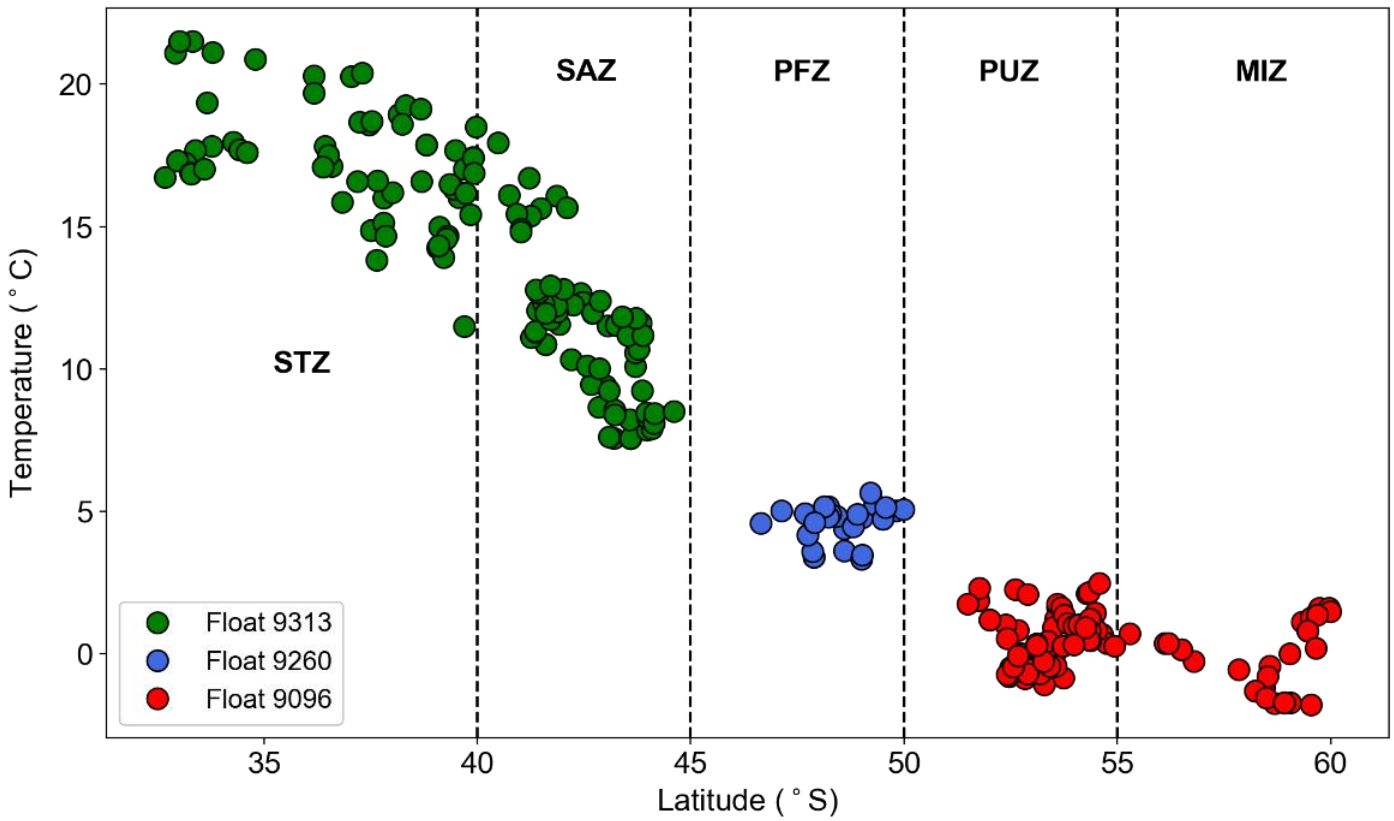

Figure B1: Sea surface temperature measured in each zone from 30 °S – 60 °S

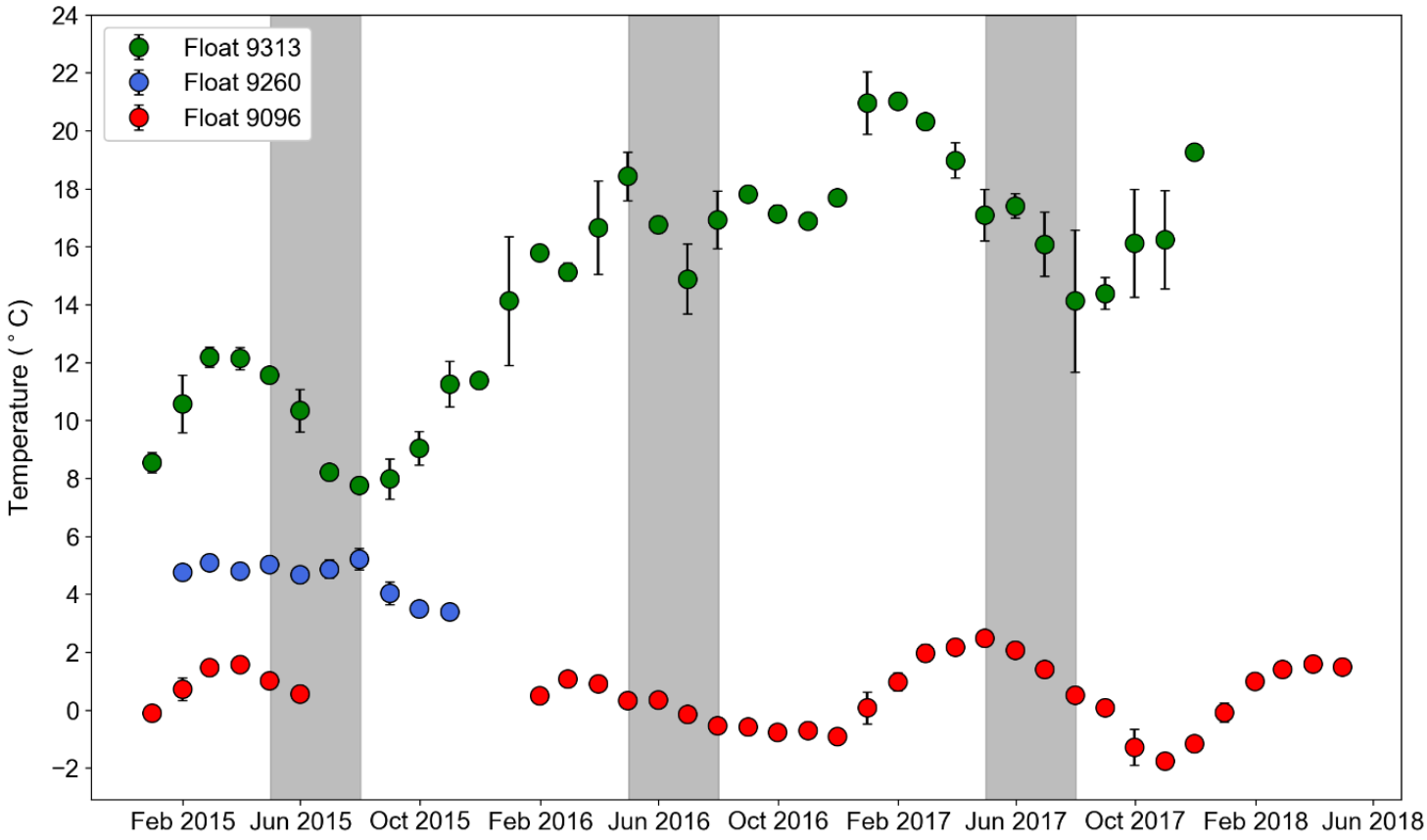

Figure B2: Available monthly average sea surface temperature measurements in each zone from December 2014 – April 2018

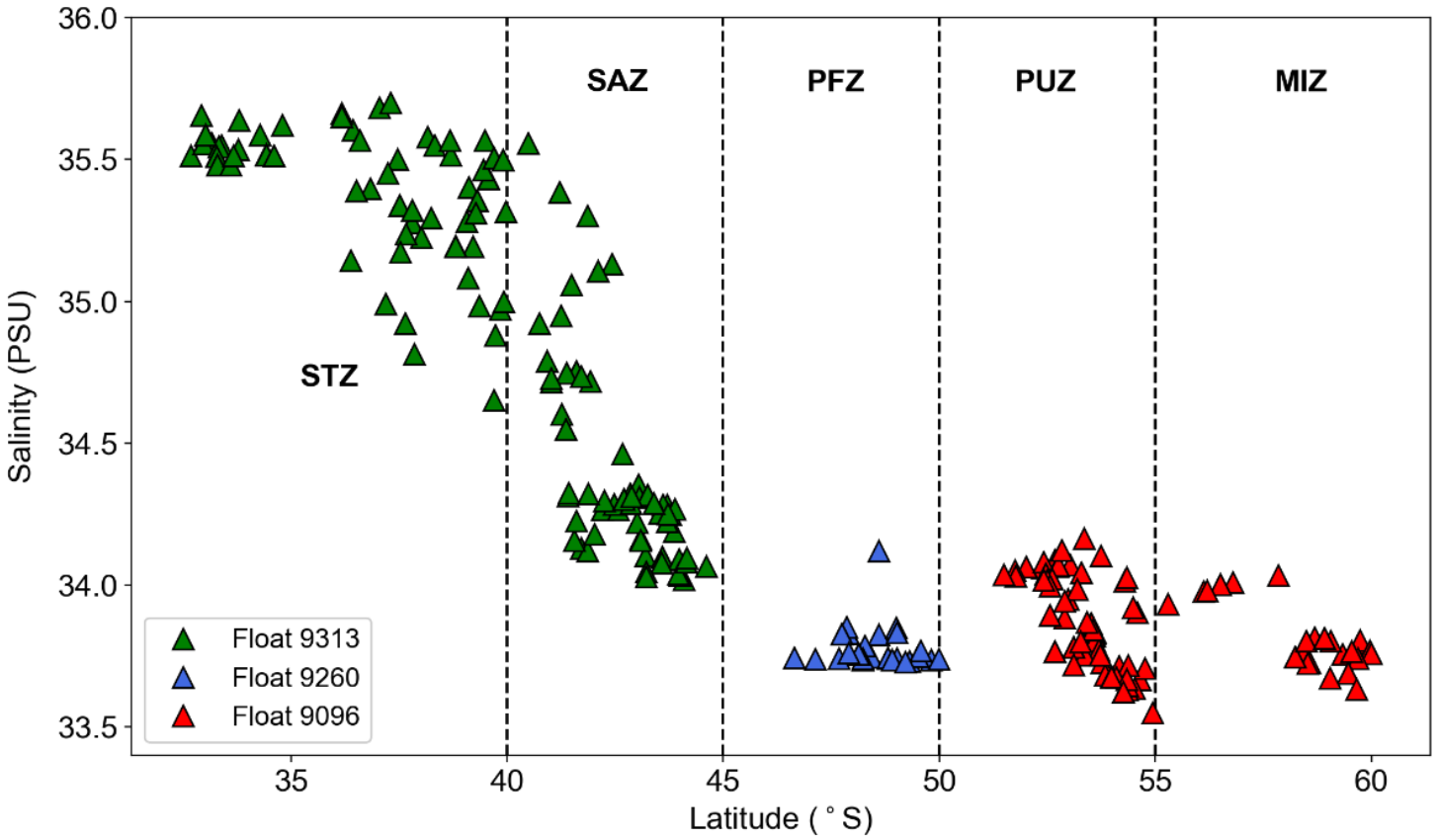

Figure B3: Sea surface salinity measurements in each zone from 30 °S – 60 °S

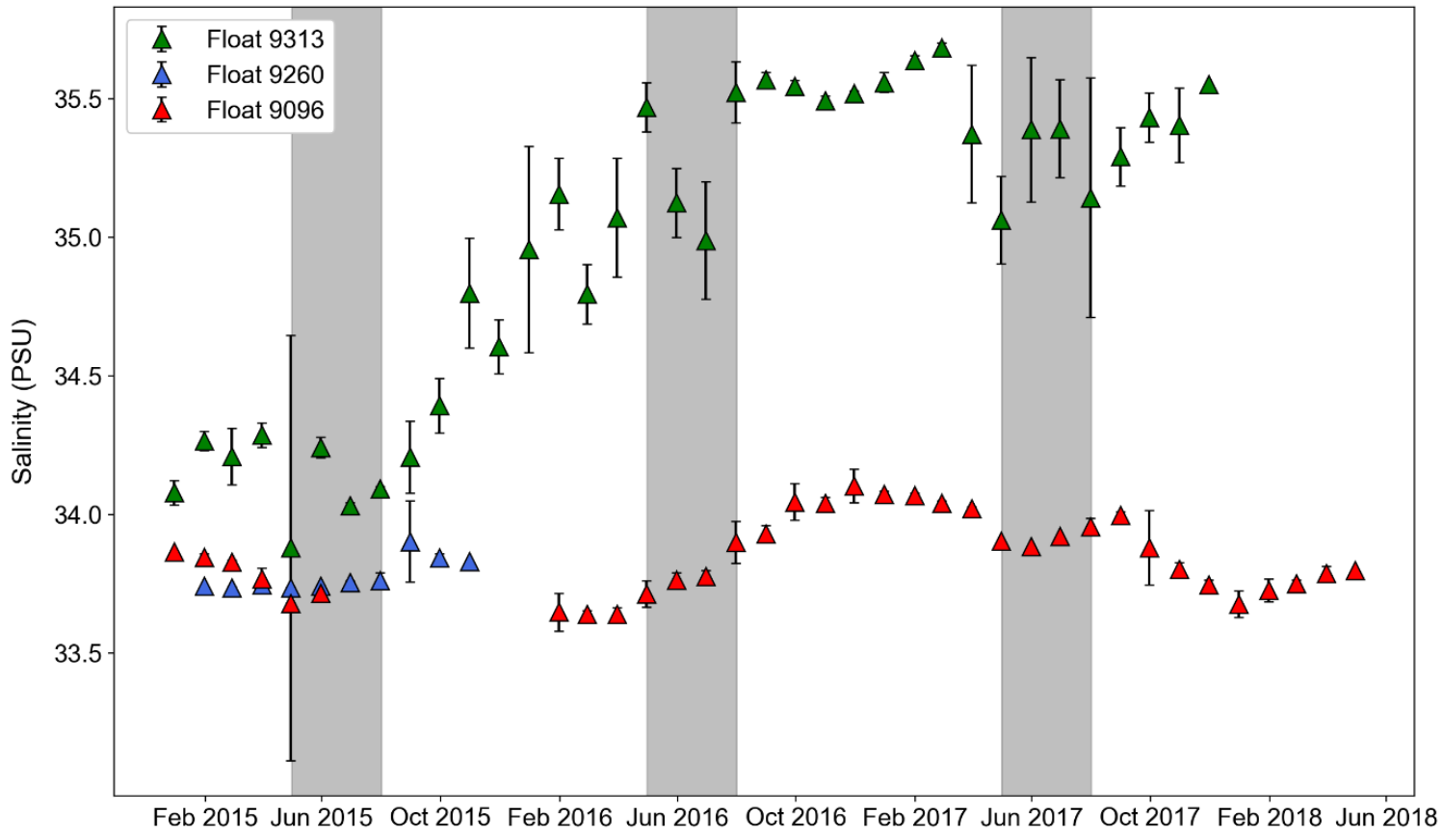

Figure B4: Available monthly average sea surface salinity measurements in each zone from December 2014 – April 2018

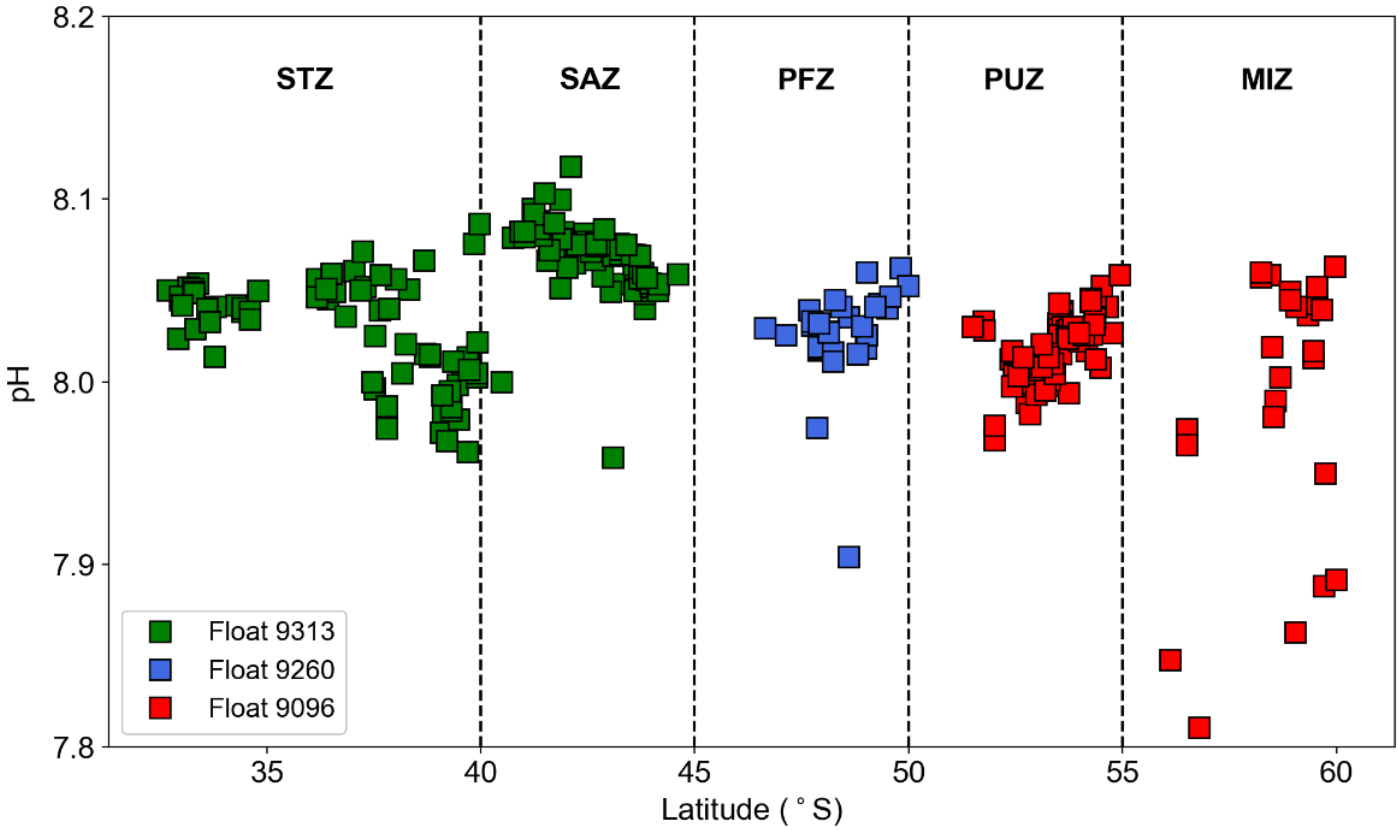

Figure B5: Sea surface *in situ* pH measurements in each zone from 30 °S – 60 °S

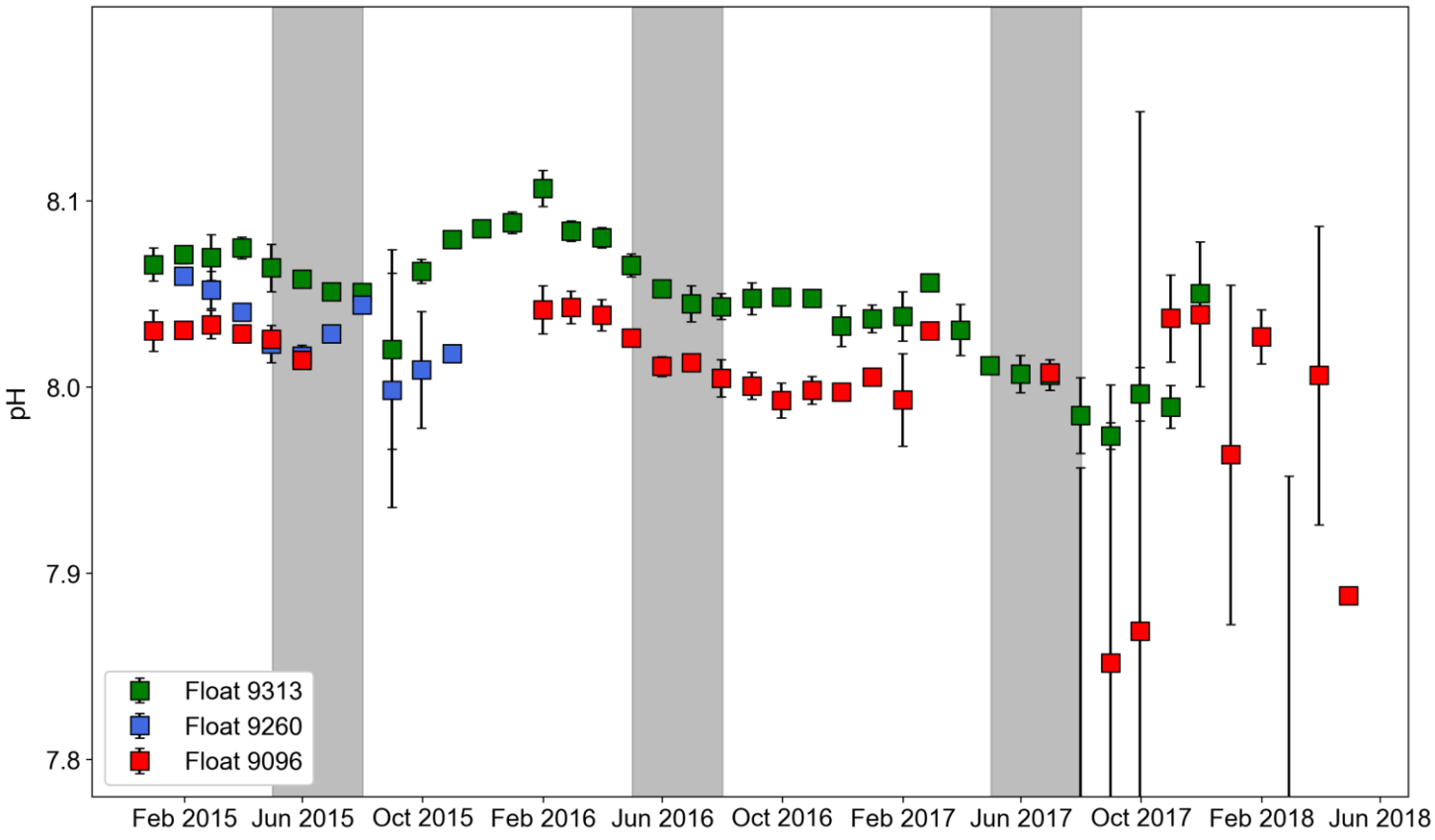

Figure B6: Available monthly average sea surface pH measurements in each zone from December 2014 – April 2018

Surface ocean TA estimates calculated from float-based measurements by means of the LIAR algorithm (LIAR_TA) and the Lee expression (LeeTA) are shown in Figure B7. LIAR_TA estimates showed an increase in TA as Float 9313 moved from the SAZ (2283 ± 20.17 μmol/kg) to the STZ (2329 ± 9.912 μmol/kg). The regional average of LIAR_TA showed a decrease from the SAZ to the PFZ (2274 ± 6.275 μmol/kg). The PUZ and MIZ had an average LIAR_TA of 2295 ± 12.69 μmol/kg and 2294 ± 7.950 μmol/kg, respectively. By comparison, LeeTA showed an almost constant average of 2291 ± 8.879 μmol/kg and 2291 ± 7.065 μmol/kg in the PUZ and MIZ, respectively. It is seen that LIAR_TA showed a good correlation with LeeTA in the STZ, SAZ and PFZ, however, it is shown to have had a higher estimate of TA in the MIZ. This suggests that the LIAR expression is also affected by a summer bias which will be further explored in Section 5.4

The temporal distribution of LIAR_TA and LeeTA are shown in Figure B8. An increasing trend in TA was observed moving from the SAZ to the STZ according to data from Float 9313, with no significant difference seen between LIAR_TA and LeeTA, and little seasonal variation observed across the annual cycle. This suggests that the LIAR_TA algorithm is insensitive to changes in TA due to biological activity as we expect to see biological activity in the SAZ during the spring-summer transition. Float 9260 situated in the PFZ showed an increase in TA from the winter (May – Aug 2015) into the summer period (Jun – Nov 2015), with no significant difference observed between LIAR_TA and LeeTA.

In contrast, LIAR_TA in the MIZ (Float 9260) showed a strong seasonal trend, with high values of TA seen in the summer months of 2014/2015 and 2016/2017, and additionally, right before the onset of the winter months in April/May 2016. A significant difference between LIAR_TA and LeeTA was observed in the PUZ/MIZ from Aug 2016 – Apr 2018. However, it is noted here that these highs for LIAR_TA directly coincide with the trend in measured salinity by the float during the same time period, which is expected from what we know of TA expressions being heavily correlated with salinity.

The resulting calculated pCO_2 values based on pH_T measurements and LIAR derived TA are shown in Figures B9 – B10. pCO_2 is seen to increase as Float 9313 moves from the SAZ (369.7 ± 20.84 μatm) to the STZ (406.6 ± 21.32 μatm), which showed a seasonal trend of highs during the winter months, and lows during the summer months. This is expected in the STZ region as it is dominated by changes in temperature – we see a loss of pCO_2 to the atmosphere in the warmer season, and an intake of pCO_2 from the atmosphere into the ocean during the colder

season. In addition, due to the uptake of CO_2 by biology, we expect to see a low pCO_2 during the summer in the SAZ, as evidenced by the WG, and high pCO_2 in the winter, as seen from ship-board measurements.

pCO_2 is shown to increase from the SAZ to the PUZ (408.0 ± 18.60 μatm). The PFZ (406.4 ± 32.73 μatm) showed a significant increase in pCO_2 in the winter of 2015, but essentially showed a similar trend as the SAZ. The PUZ showed low pCO_2 in the winter months, likely due to the inhibition of exchange at the air-sea interface from sea-ice coverage, and highs in the summer months coincident with a lack of ice-cover. pCO_2 values from 2016 to 2017 in the MIZ are not shown here due to bad data flags in the dataset and were thus excluded. Calculated values for TA and pCO_2 are summarised in Table 4.5.

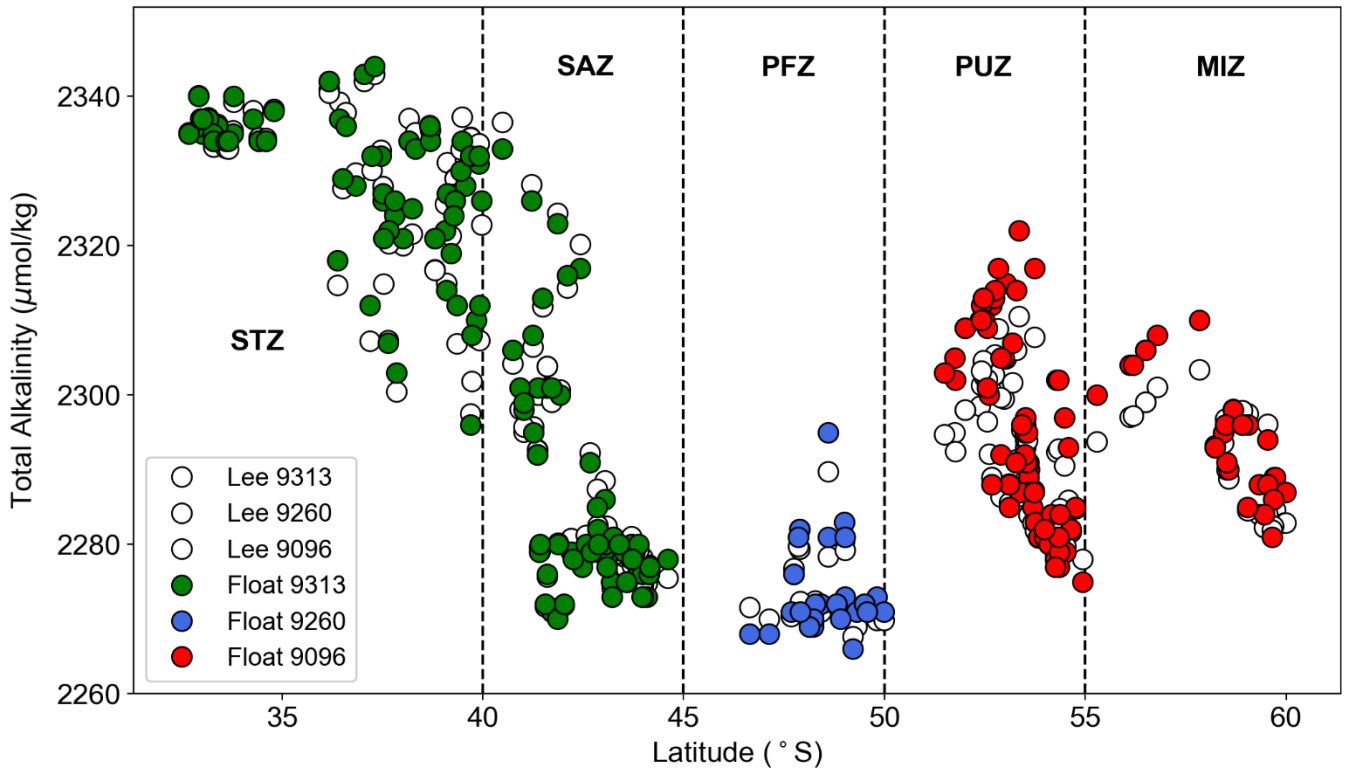

Figure B7: TA estimated by the LIAR algorithm for floats 9096 (red), 9260 (blue) and 9313 (green) in the surface-ocean (upper 10 m) compared to TA derived from the Lee expression (white).

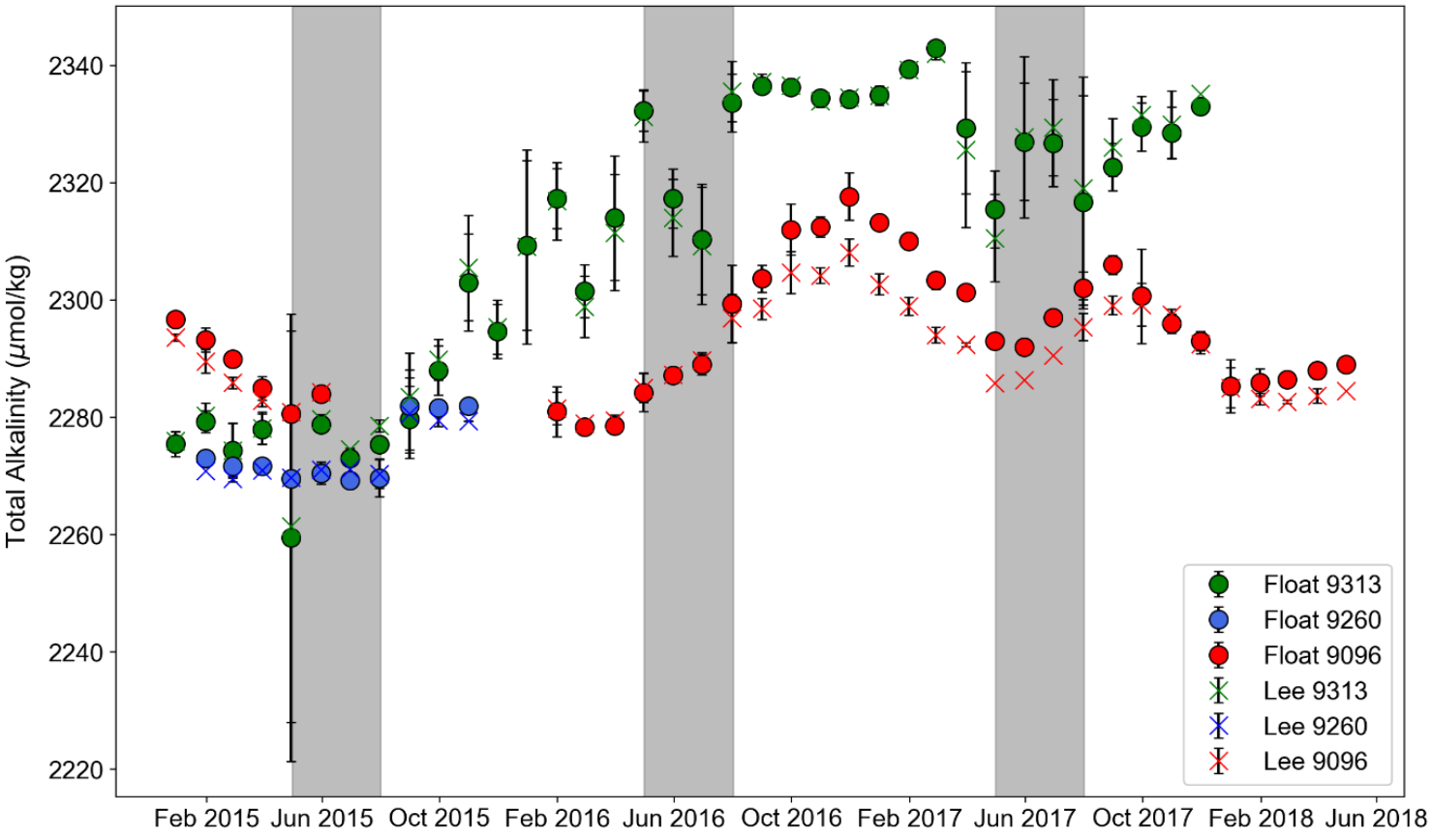

Figure B8: Available monthly average estimated TA at the sea surface, calculated from LIAR and Lee equations from December 2014 – April 2018

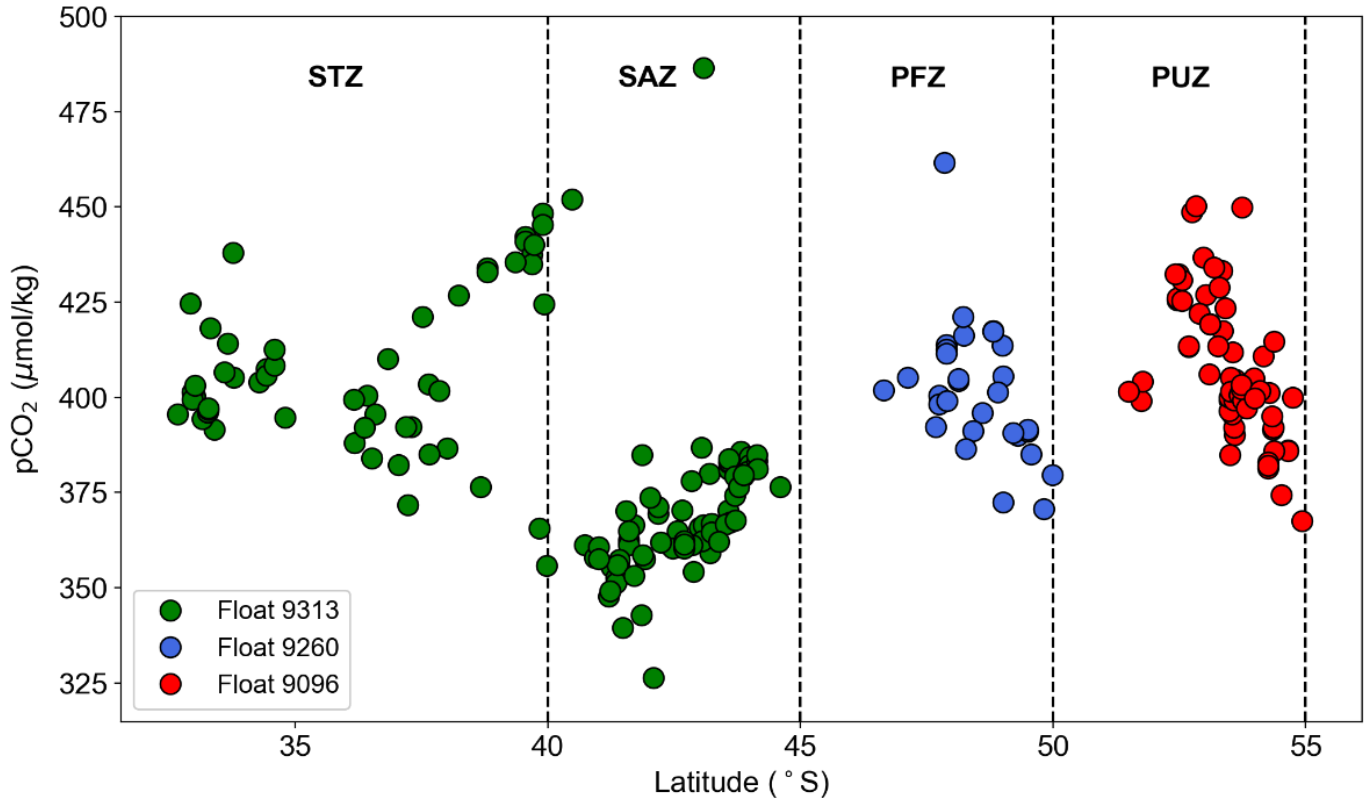

Figure B9: Estimated pCO_2 at the sea surface in each zone from 30 °S – 60 °S

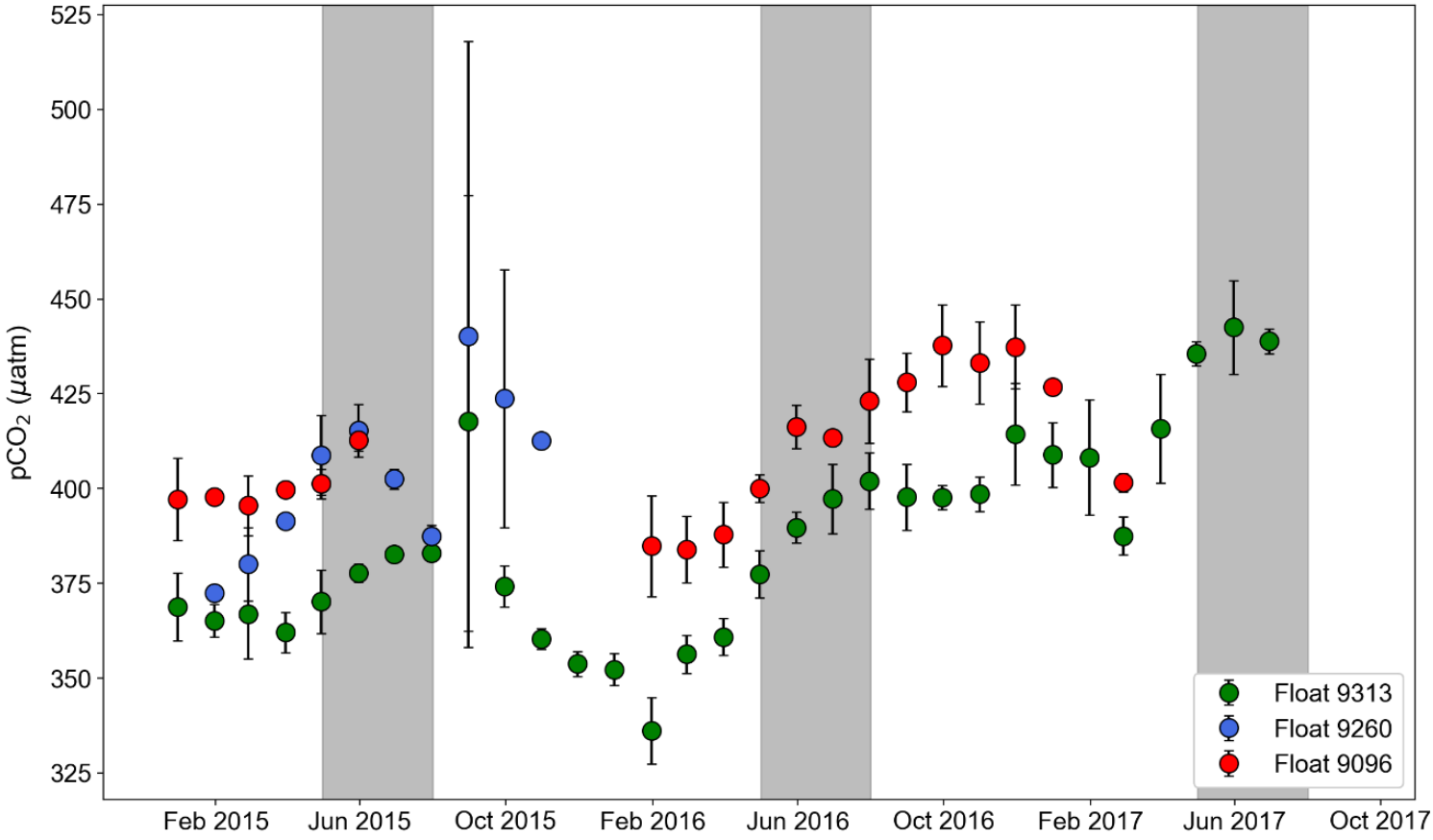

Figure B10: Available monthly average estimated pCO_2 at the sea surface in each zone from December 2014 –Sep 2017

Table B1: Average sea surface float-based measurements for each zone

Float	Temperature (°C)	Salinity (PSU)	pH_T
STZ	17.29 ± 2.041	35.40 ± 0.227	8.027 ± 0.029
SAZ	11.10 ± 2.506	34.35 ± 0.450	8.067 ± 0.021
PFZ	4.529 ± 0.666	33.78 ± 0.075	8.026 ± 0.028
PUZ	0.542 ± 0.909	33.86 ± 0.161	7.973 ± 0.181
MIZ	-0.089 ± 1.190	33.81 ± 0.113	7.927 ± 0.182

Table B2: Average estimated TA and pCO_2 for the LIAR and Lee expressions per zone

Float	LIAR_TA (µmol/kg)	LeeTA (µmol/kg)	LIAR pCO_2 (µatm)
STZ	2329 ± 9.912	2329 ± 10.95	406.6 ± 21.32
SAZ	2283 ± 20.17	2284 ± 19.10	369.7 ± 20.84
PFZ	2274 ± 6.275	2274 ± 4.937	406.4 ± 32.73
PUZ	2295 ± 12.69	2291 ± 8.879	408.0 ± 18.60
MIZ	2294 ± 7.950	2291 ± 7.065	-

Discrete data in Southern Ocean is limited in winter, however, a seasonal cycle of nitrate can be constructed from summer voyage datasets which is outside the scope of this study. The illustration of nitrate for the winter season in the SO showed the latitudinal changes of nitrate moving from the SAZ to the MIZ, which is necessary to have the full picture of what is occurring in each zone for this season in particular. The basis of this study is that winter-time datasets are scarce, and while the nitrate seasonal cycle can be shown for the SOCCOM float data, it is still necessary to see how sensor data compares to discrete shipboard measurements in the region.

From Figure B11 we see that nitrate concentrations increase in the winter months in each zone, as expected with the decrease in biological activity and low light conditions in the Southern Ocean.

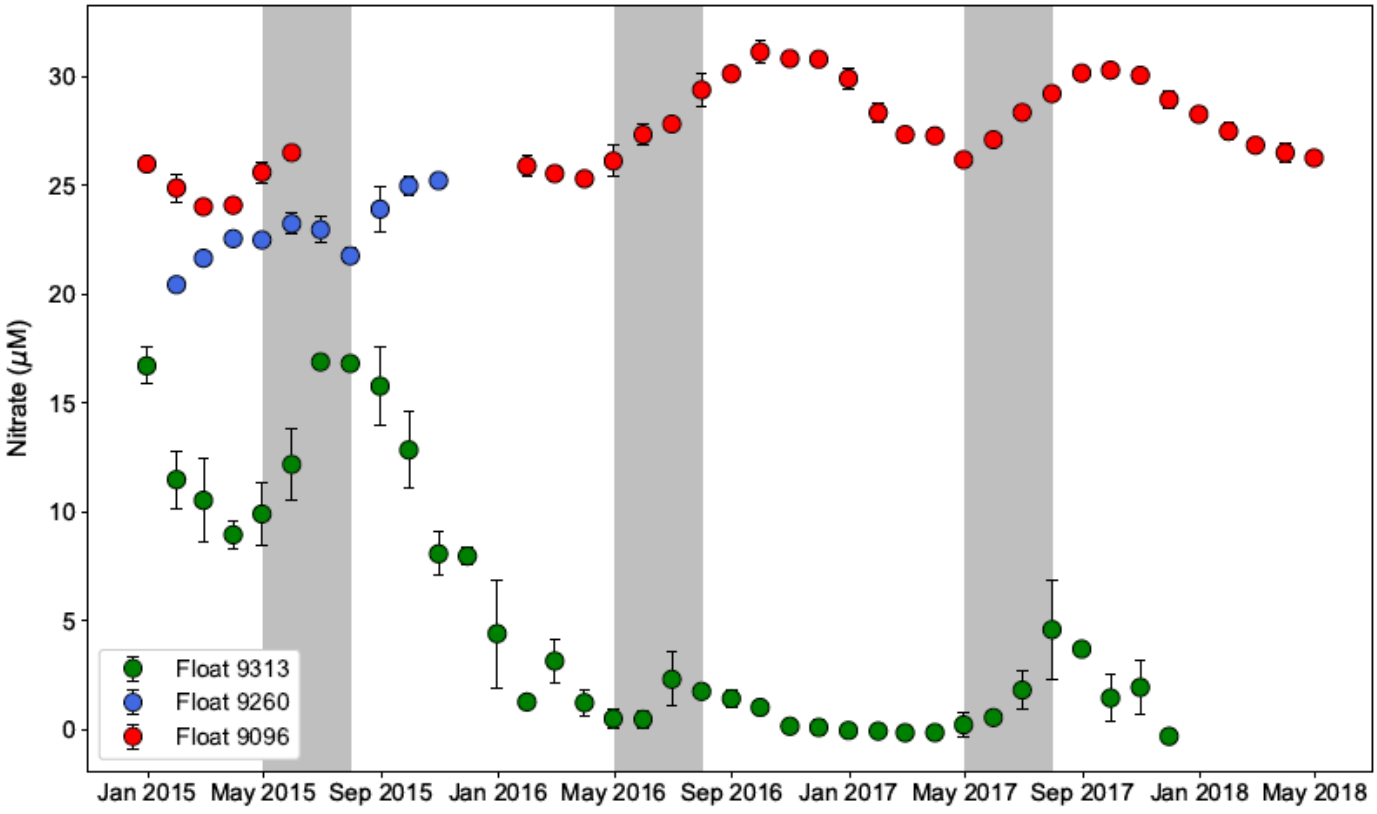

Figure B11: Available monthly average nitrate concentrations at the sea surface in each zone from December 2014 – April 2018

APPENDIX C

Key	
✓	There is a significant difference between the datasets

C.1.1 Wave Glider p-value tables

Table C1: p-values for WGTA compared to LeeTA

	LeeTA		**LeeTA_pre**		**LeeTA-bloom**	**WGTA-bloom**	
WGTA	2.20×10^{-16}	✓					
WGTA-pre			2.20×10^{-16}	✓		2.39×10^{-6}	✓
WGTA-bloom					0.6019		
WGTA_pre							
LeeTA_pre					8.095×10^{-16}		

Table C2: p-values for $WGpCO_2$ compared to $LEEpCO_2$

	$LEEpCO_2$		**$LEEpCO_2$_pre**		**$LEEpCO_2$_bloom**
$WGpCO_2$	2.92×10^{-2}	✓			
$WGpCO_2$-pre			2.13×10^{-15}	✓	
$WGpCO_2$-bloom					0.8658

C.1.2 Winter Cruise p-value tables

Table C3: p-values from WC2015-WC2017 on significant difference of salinity

Salinity	15v17		16v17		15v16	
STZ	0.007542	✓	0.1924		0.1683	
SAZ	5.90×10^{-6}	✓	0.04957	✓	0.3597	
PFZ	0.6913		0.2525		0.00408	✓
PUZ	0.07686	✓	0.4919		0.004859	✓

Table C4: p-values from WC2015-WC2017 on significant difference of temperature

Temperature	15v17		16v17		15v16	
STZ	0.003473	✓	0.1359		0.6927	
SAZ	0.05228		0.06658		0.7373	
PFZ	0.2677		0.189		0.6144	
PUZ	0.0001824	✓	0.4922		0.112	

Table C5: p-values from WC2015-WC2017 on significant difference of nitrate

Nitrate	15v17		16v17		15v16	
STZ	0.7777		0.7525		0.6043	
SAZ	0.1473		0.004869	✓	0.782	
PFZ	0.08925	✓	0.02497	✓	0.1197	
PUZ	0.05432		0.0001514	✓	0.1027	

Table C6: p-values from WC2015-WC2017 on significant difference of total alkalinity

Total Alk	**15v17**		**16v17**		**15v16**	
STZ	0.9461		0.3575		0.3741	
SAZ	0.006244	✓	0.003989	✓	0.8998	
PFZ	0.02109	✓	0.0009246	✓	0.2419	
PUZ	0.2441		0.0004533	✓	7.70×10^{-5}	✓

Table C7: p-values from WC2015-WC2017 on significant difference of LeeTA

LeeTA	**16v16**		**17v17**		**15v15**	
STZ	0.665		0.0228	✓	0.3441	
SAZ	0.1047		0.9067		0.5657	
PFZ	0.000473	✓	0.8083		0.006861	✓
PUZ	0.000409	✓	0.4381		3.30×10^{-5}	✓
MIZ			0.36			

Table C8: p-values from WC2015-WC2017 on significant difference of pCO_2

pCO_2	**15v17**		**16v17**		**15v16**	
STZ	0.02089	✓	0.001604	✓	0.04799	✓
SAZ	0.01381	✓	0.2264		0.002877	✓
PFZ	0.5248		0.002504	✓	6.19×10^{-5}	✓
PUZ	0.893		6.90×10^{-5}	✓	8.45×10^{-7}	✓

Table C9: p-values from WC transects compared to LeeTA

	LeeTA	
WC2017	0.2343	
WC2016	6.01×10^{-3}	✓
WC2015	0.03269	✓

C.1.3 SOCCOM float p-value tables

Table C10: p-values for significant difference between LeeTA and Liar_TA for each float

SOCCOM	**Liar vs Lee**
Float 9096	0.01253
Float 9260	0.6789
Float 9313	0.08662

Table C11: p-values for significant difference between LeeTA and Liar_TA for each zone

SOCCOM by zone	
STZ	0.9921
SAZ	0.7448
PFZ	0.6789
PUZ	0.03088
MIZ	0.2019

APPENDIX D

This section serves to outline possible considerations, limitations, and uncertainties related to this study.

D.1 Alternate correction method for pH calibration

The decision to use a percentage error method to calibrate the pH sensor as the raw measured readings from the WG I dataset proved to have unrealistic corresponding DIC and TA values when combined with WGpCO_2 observations to derive all the carbonate values, which were far outside of the acceptable margins of error for such a calculation. Rather than affecting the apparent trend in the data that was captured by the sensor, a percentage error approach was applied to bring the pH observations within an acceptable range of values.

We acknowledge that this method makes the WG dataset and subsequent calculations of WGTA dependent on the reference value for pH. However, the reference value is supported by discrete samples of DIC and TA that were acquired from the deployment of the second WG, as well as climatological pH derived from available pCO_2 and TA monthly estimates in the region. Both WG I and II were subjected to the same correction, while WG II did not have a significant adjustment like WG I, it was still corrected in the same manner. pH was calculated from this to determine what would be a 'likely' pH value and taken to be the reported reference values for the correction.

However, owing to the inverse relationship between pH and pCO_2 (Figure D1), and logarithmic nature of pH, a further step in the correction process was performed on $[H^+]$ concentration derived from the raw pH data obtained by the Durafet sensor, which has a linear relation to pCO_2 (Figure D2). The $[H^+]$ concentration was then corrected by the percentage error method outlined in Section 3.4.1 and converted to pH.

Figure D1 shows the relation between WGpCO_2 and pH derived from the pH % correction and the $[H^+]$ % correction – clearly showing that the $[H^+]$ % correction pH values have more variation than the pH % correction values, which have a strongly inverse relationship with WGpCO_2. Figure D2 shows the relation between WGpCO_2 and $[H^+]$ between WG I and WG II, where WG I concentrations show less correlation with WGpCO_2 than WG II, reinforcing the need for additional calibration to the sensor readings that require a less sensitive approach to changes.

Figure D3 shows the raw pH data, the pH corrected by % error, and the pH derived from the corrected [H^+] concentration. As expected, the alternate correction of [H^+] concentration also acts to lower the pH within acceptable reported ranges for surface ocean seawater. At present there is not enough data to account for a reason for the observed variations for pH derived from the [H^+] concentration correction. We acknowledge that the slight decreasing trend observed in the pH [H]corr values from October - November may be attributed to a number of factors such as initial calibration of the sensor on WG I, drift between the internal and external electrodes of the Durafet pH sensor (Martz et al., 2010), or shifts in the surface ocean properties temperature (Figure 4.4).

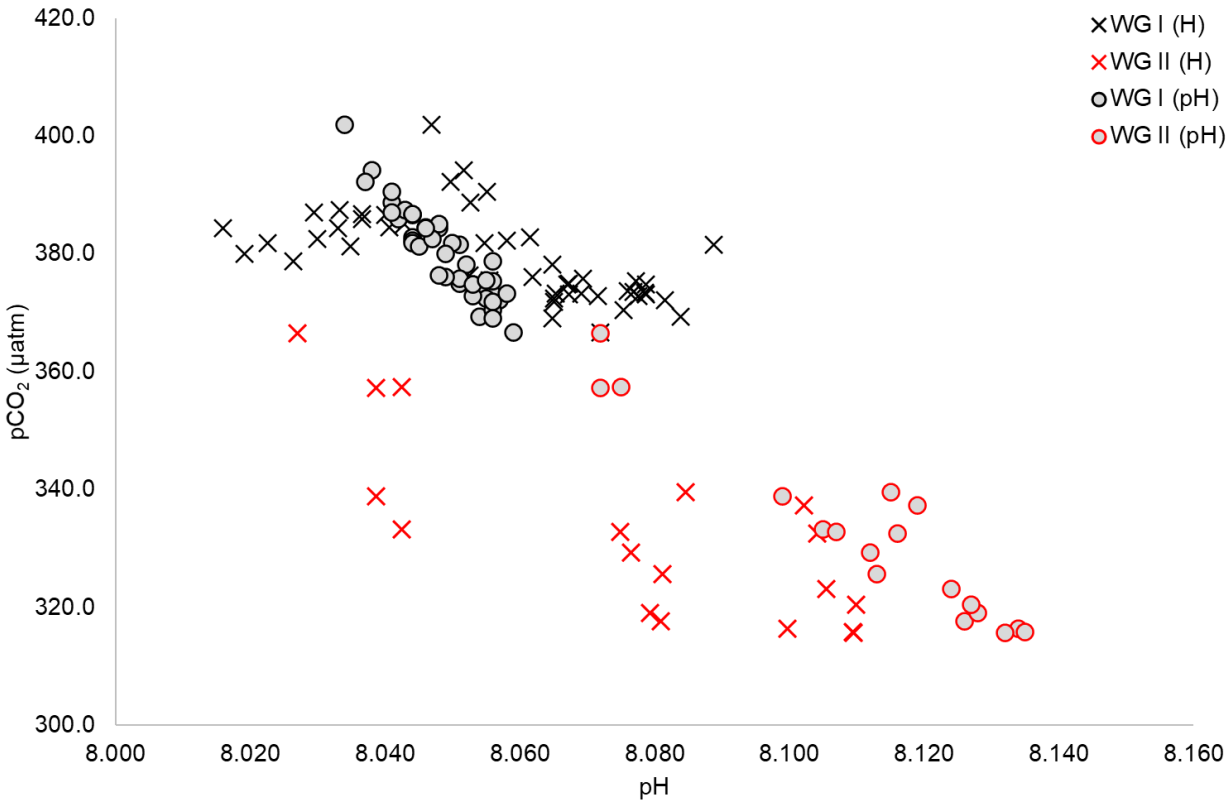

Figure D1: Relationship between WGpCO_2 and pH from [H^+] and pH % corrected values for WG I and WG II between October and December 2013

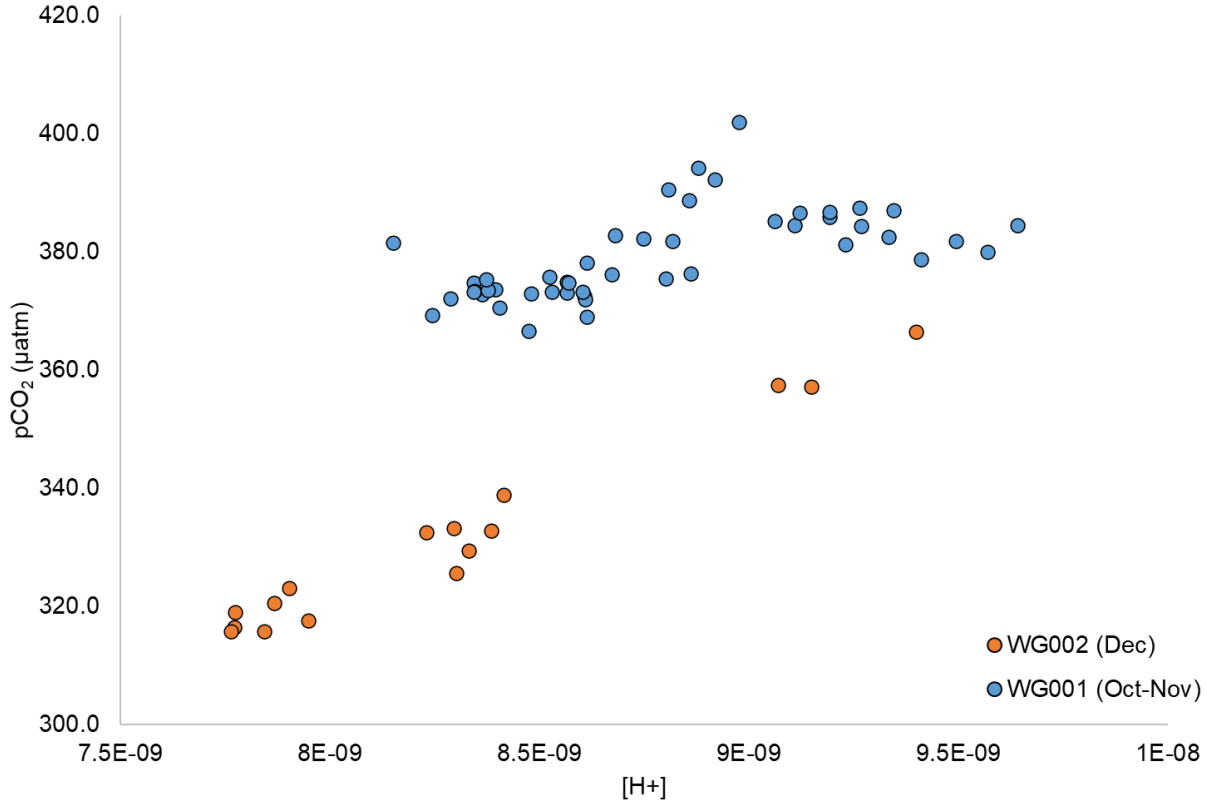

Figure D2: Relationship between $WGpCO_2$ and $[H^+]$ corrected values for WG I and WG II between October and December 2013

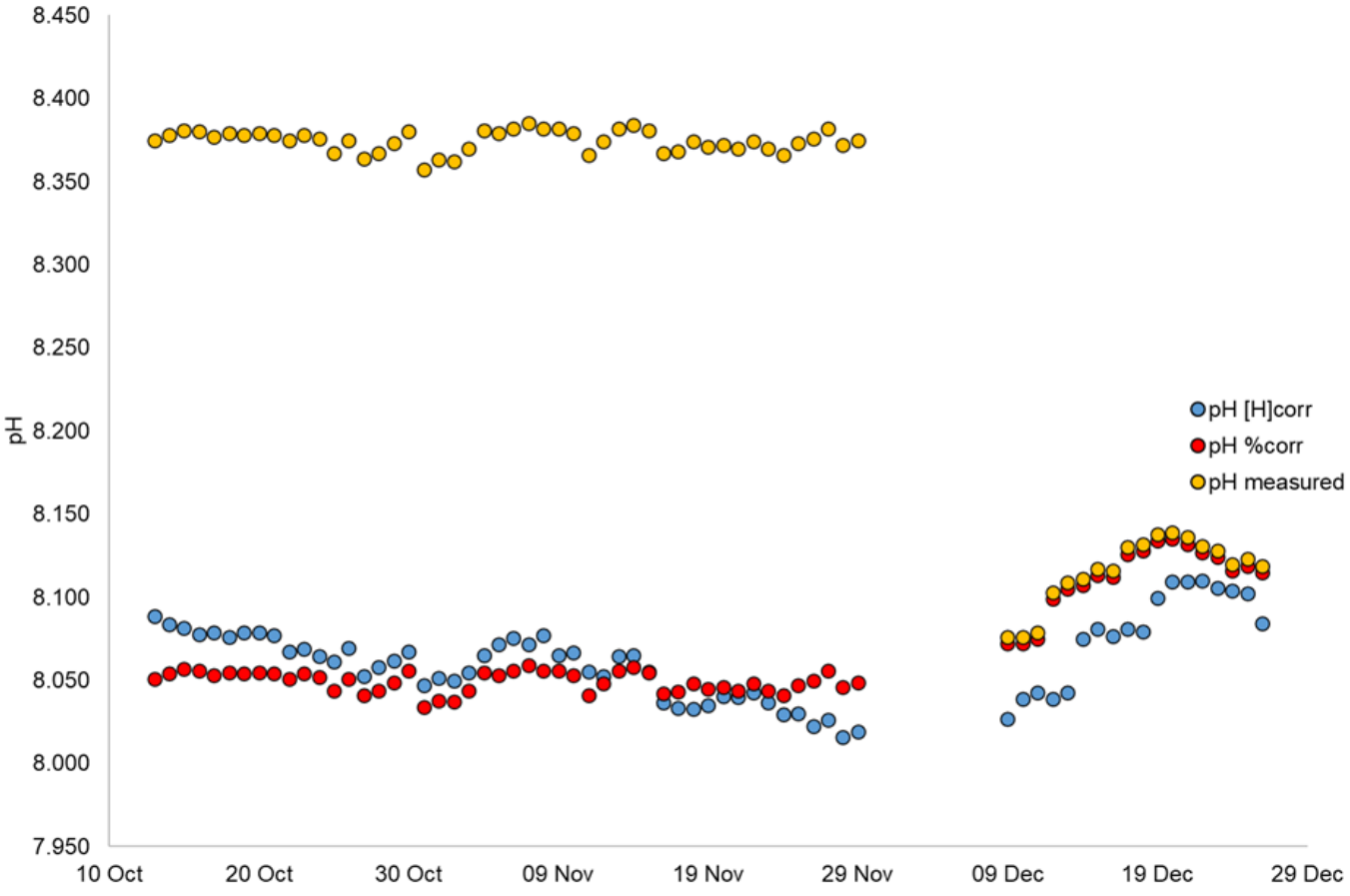

Figure D3: Raw pH data output from the Wave Glider compared to the percentage error corrected values($[H^+]$ and pH) between October and December 2013

D.2 Seasonal bias of TA algorithms

In trying to resolve the seasonal bias of measurements, we compared GLODAPv2.2019 data (Key et al., 2015, Olsen et al., 2016) with WC, WG, LeeTA and LIAR_TA data available in the region of study (WG location). However, we acknowledge that these values are not temporally consistent with the SOCCOM, WC, or WG datasets. Spatially comparative GLODAP data was obtained from February 2008, November 2004, and December 2014, all of which fall within the austral summer months.

The seasonal bias of the data points is clearly not representative of a complete seasonal cycle in TA. As seen from Figure D4, GLODAPv2.2019 data points coincide with LIAR_TA and LeeTA estimates from October – December, with higher values in February that are similar in range to the WGTA data points – whether or not this coincides with a late summer bloom cannot be determined without additional data. Similarly, WC data show that there is a range in TA during the winter season that is not captured by the algorithms, reinforcing that there exists a seasonal bias in the formulae. This study does not expand the domain of study outside of the sampled region would be subject to the same data bias that already exist due to the scarce data measurements in the Southern Ocean.

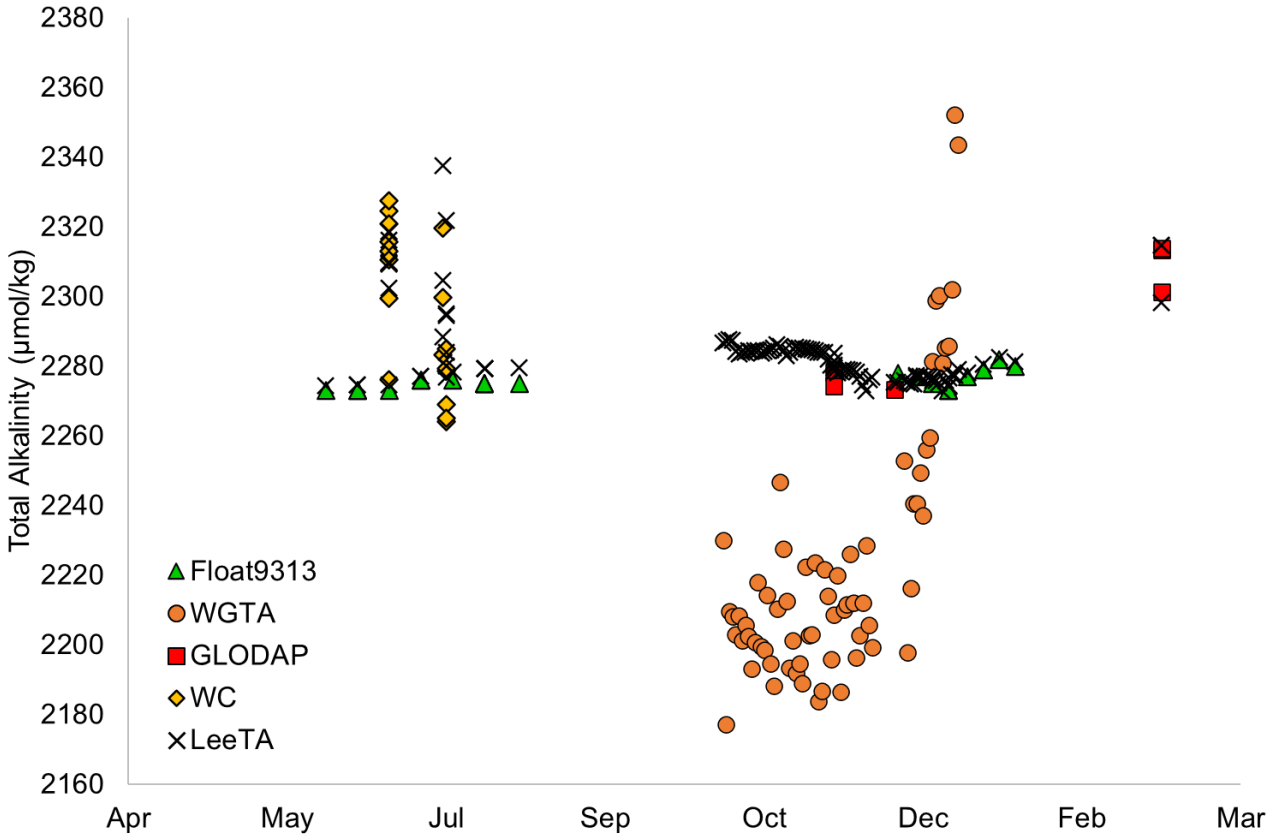

Figure D4: Comparison of TA per month compiled from WC, WG, GLODAPv2.2019 and SOCCOM datasets

D.3 Relation between LeeTA and LIAR_TA

The following graph was constructed to illustrate the deviations between LIAR and Lee TA across the SO, at temperatures below 0 °C and between 11-12 °C. Figure D5 was constructed using observational data obtained from shipboard and float-based measurements. We see the relationships differ from one another most at temperatures below 0 °C, however, show a remarkable similarity (1:1) at temperatures between 11 – 12 °C. This supports our theory that Lee TA and LIAR TA are similar in nature in the biologically productive regions of the SO i.e. accounting for nitrate and oxygen in the LIAR formulation does not show a significant difference from simpler formulations based on only salinity and temperature.

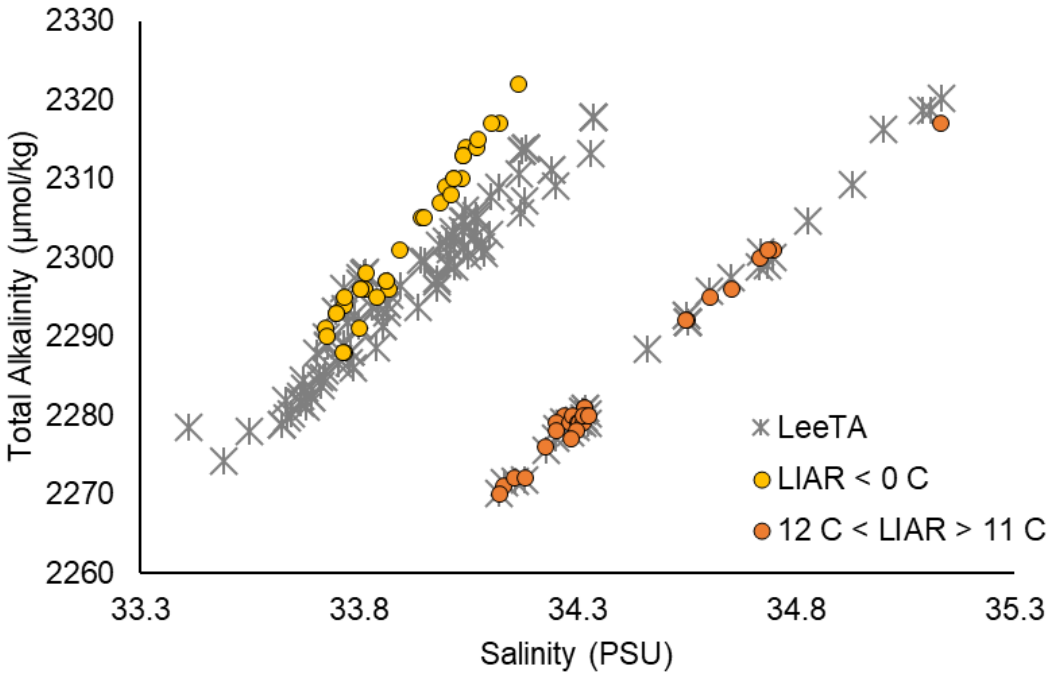

Figure D5: Comparison between LeeTA and LIAR_TA across a range of Southern Ocean conditions at temperatures below 0 °C and between 12-11 °C

D.4 Impact of changes in LeeTA on derived pCO_2

Hypothetical scenarios were carried out on LeeTA, lowering the TA concentration by 10, 30 and 60 µmol/kg respectively to mimic the expected lower TA during the pre-bloom conditions, these values were then used to compute pCO_2 and compared to $WGpCO_2$ observations.

Figure D6 shows the derived pCO_2 values from varying TA and WGpH. As observed, larger magnitude changes in LeeTA result in a significant difference of calculated pCO_2 and correlate more closely to the observed $WGpCO_2$ measurements, as seen from the scenario where LeeTA is decreased by a magnitude of 60 µmol/kg. This indicates that the discrepancy observed between $LEEpCO_2$ and $WGpCO_2$ (Figure 4.7) can be reconciled by accounting for a bias in nitrate uptake during the bloom period i.e. accounting for remineralisation (no nitrate uptake) and a subsequently lower TA (WGTA) in the pre-bloom period.

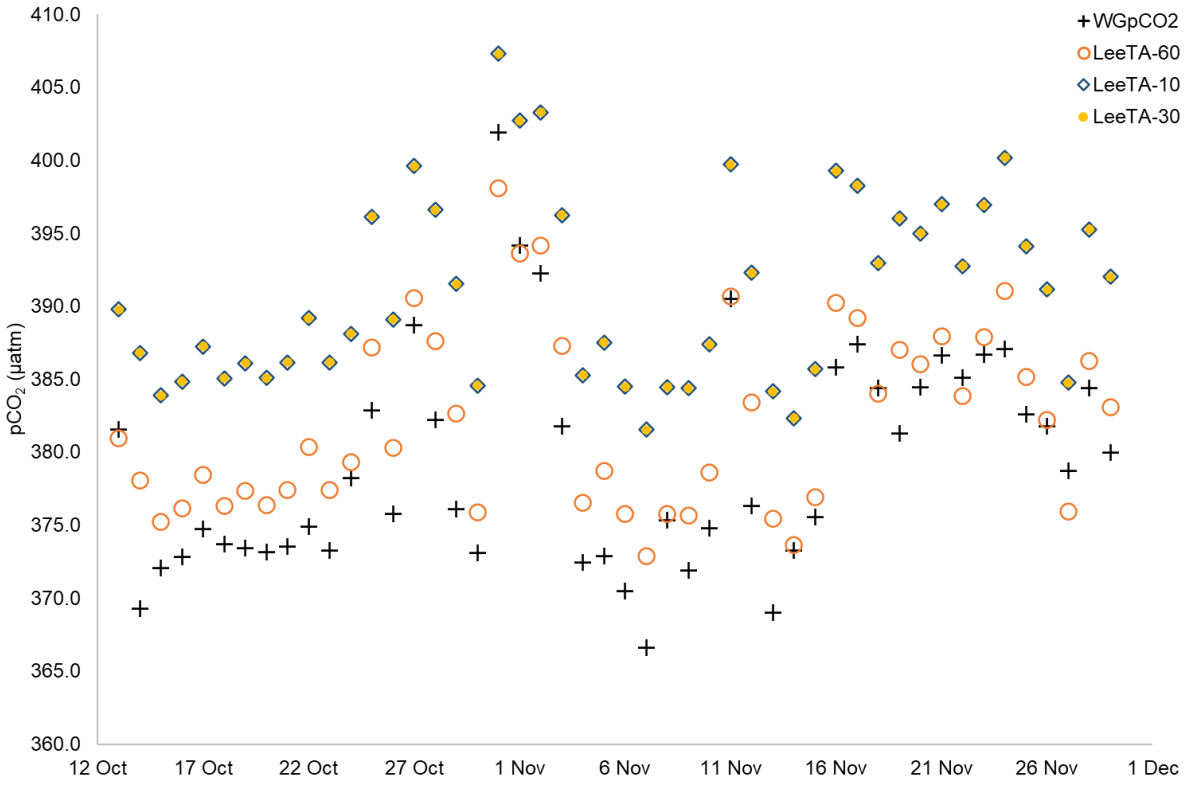

Figure D6: Resultant estimates of pCO_2 with decreasing LeeTA during the pre-bloom period as compared to $WGpCO_2$ observations

D.5 Impact of the nitrate seasonal cycle on TA

The changes in TA associated with the nitrate seasonal cycle are difficult to resolve without corresponding discrete measurements of TA throughout the seasonal cycle in the Southern Ocean. For this purpose, we show the correlation between LIAR_TA in the STZ and SAZ (regions of high biological activity) and corresponding nitrate sensor measurements, compared with discrete TA observations from cruise data in the winter season. From Figure D7 we observe seasonal cycle of nitrate as measured by the SOCCOM float sensors, we see a maximum nitrate concentration between June – August, the winter period when nitrate uptake is expected to be low, these values are supported by the WC datasets for discrete measurements of surface nitrate concentrations.

Figures D8 and D9 show the correlation between LIAR_TA, WC TA observations and the corresponding nitrate concentrations. Both datasets show a strong correlation between TA nitrate concentration, showing a linearly inverse relationship i.e. for low nitrate concentrations, TA is high in concentration (in accordance with the findings of this study), and TA is low when nitrate concentrations are at a high – this can be indicative of nitrate uptake and remineralisation. However, we acknowledge that there are several factors that could affect TA in this region that cannot be definitively resolved with the available data. It is suggested that a time series of discrete data measurements be obtained to constrain the seasonal cycle of TA, as well as validate the float sensor measurements in under-sampled regions of the SO.

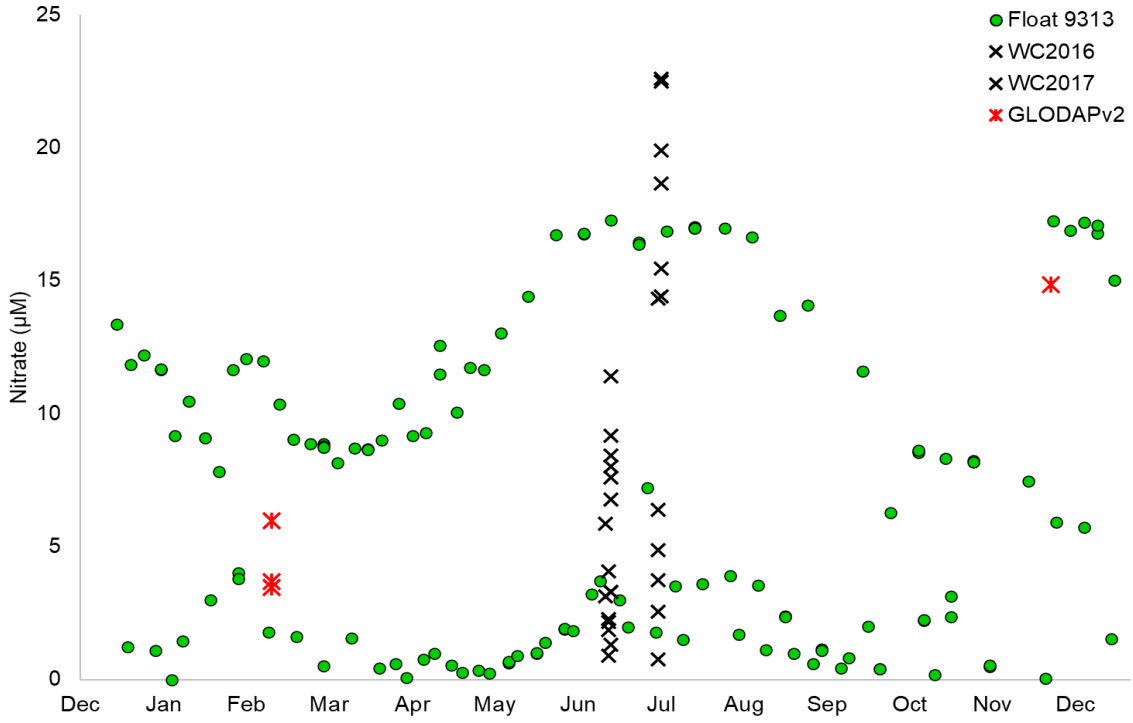

Figure D7: Float, WC and GLODAPv2 nitrate concentration data in the STZ/SAZ region per month

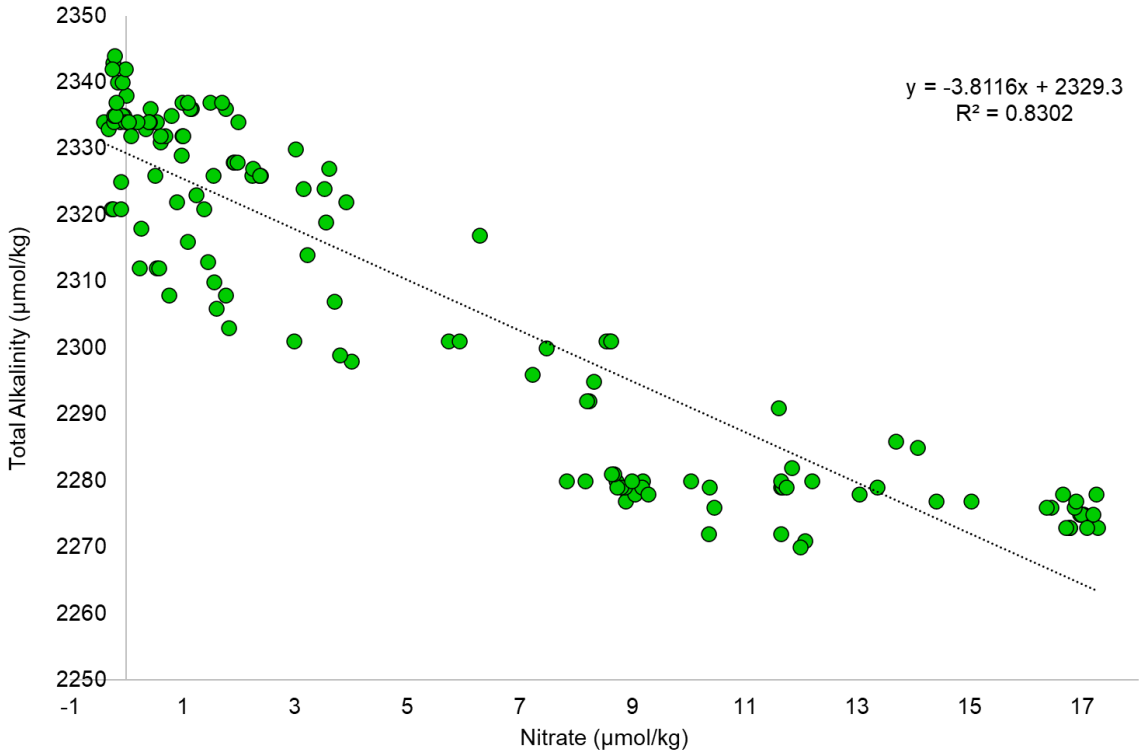

Figure D8: LIAR_TA correlated with corresponding nitrate sensor data from Float 9313

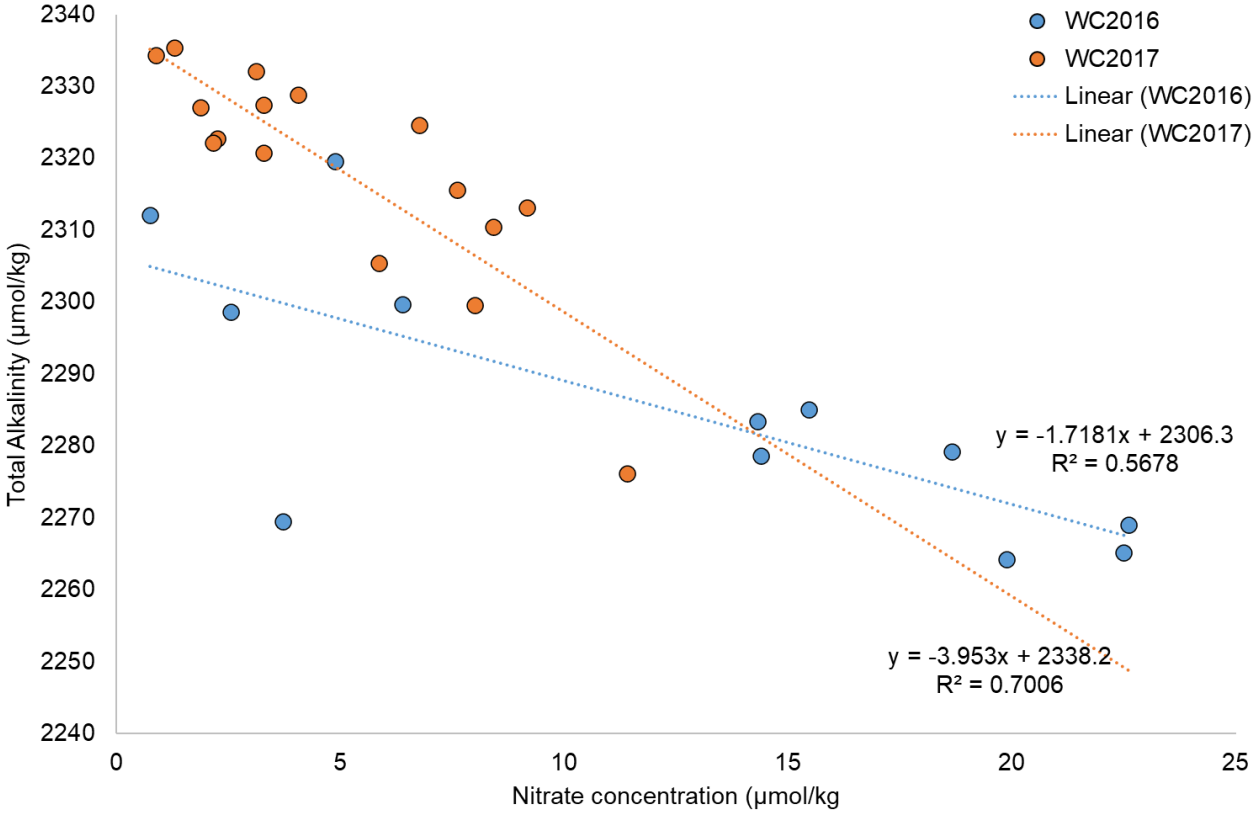

Figure D7: WC2016 and WC2017 discrete TA observations correlated with corresponding nitrate concentrations